

FOG

Freiberg Online Geosciences

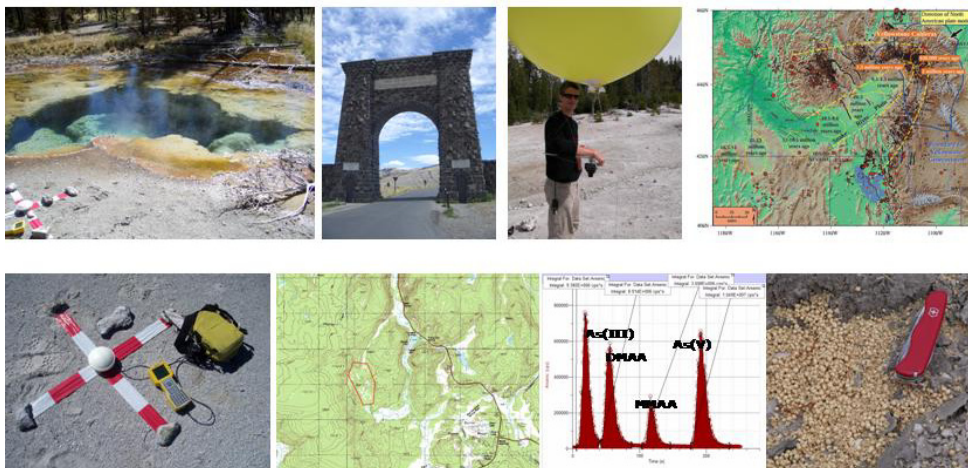
FOG is an electronic journal registered under ISSN 1434-7512



2005, VOL 13

Brimer, Baas

Hydrogeological and Hydrochemical Investigations in West Nymph Creek Thermal Area, Yellowstone National Park, USA



List of Contents

LIST OF CONTENTS	2
LIST OF ABBREVIATIONS	5
ABSTRACT	7
1 OBJECTIVES AND DELIVERABLES.....	8
1.1 OBJECTIVES.....	9
1.2 DELIVERABLES	10
2 YELLOWSTONE NATIONAL PARK.....	11
2.1 INTRODUCTION - A LAND OF SCENERY	11
2.2 GEOLOGY OF THE YELLOWSTONE NATIONAL PARK.....	12
2.2.1 <i>Pre-Quaternary Geology</i>	12
2.2.2 <i>Volcanism in the Quaternary</i>	13
2.2.3 <i>Glaciers Carve the Landscape</i>	14
2.2.4 <i>The Yellowstone Hotspot</i>	15
2.2.4.1 Track of the Hotspot	16
2.2.4.2 Resurgent Yellowstone	20
2.2.4.3 The Norris-Mammoth Corridor.....	21
2.2.5 <i>Hydrothermal Activity</i>	23
2.2.5.1 Hydrogeochemistry.....	23
2.2.6 <i>Study Area - West Nymph Creek Thermal Area (WNCTA)</i>	25
3 METHODOLOGY OF THE GEOSPATIAL ANALYSIS.....	28
3.1 INTRODUCTION TO REMOTE SENSING FROM LOW FLYING PLATFORMS.....	28
3.1.1 <i>Ground Control Points</i>	29
3.1.2 <i>Theory of GPS and DGPS</i>	29
3.2 AERIAL SURVEY	32
3.2.1 <i>Temporary Survey Grid</i>	32
3.2.2 <i>Determination of the Coordinates</i>	32
3.2.3 <i>Design of the Helium Balloon</i>	33
3.2.4 <i>Helium Balloon at Work</i>	35
3.2.4.1 Encountered Problems	36
3.3 GROUND SURVEY	37
3.3.1 <i>Feature's Name and Sample Code</i>	37
3.3.2 <i>Runoff and Discharge</i>	38
3.4 GEOGRAPHICAL INFORMATION SYSTEM (GIS).....	39
3.4.1 <i>Data Model - Raster or Vector?</i>	39
3.4.2 <i>TNTmips - Creating the Aerial Overview</i>	41
3.4.2.1 Georeferencing.....	41
3.4.2.2 Mosaicking	42

3.4.2.3	Raster Resampling	44
3.4.2.4	Digitizing the Geobjects.....	45
3.4.2.5	TNTAtlas - Displaying Geodata	46
4	CHEMISTRY	47
4.1	ARSENIC IN THE ENVIRONMENT	47
4.1.1	<i>Arsenic Toxicity</i>	48
4.1.2	<i>Arsenic in Natural Waters</i>	48
4.1.3	<i>Arsenic Species Chemistry</i>	49
4.1.3.1	Dissolved Inorganic As(V)	50
4.1.3.2	Dissolved Inorganic As(III)	51
4.1.3.3	Organic arsenic compounds	54
4.1.3.4	Dissolved Mono- and Di-methylated Arsenic Acids.....	56
4.2	SPECIES SEPARATION	58
4.2.1	<i>Hydride Generation</i>	59
4.2.2	<i>High Performance Liquid Chromatography</i>	61
4.3	APPLIED ON-SITE HYDROCHEMISTRY	62
4.3.1	<i>Parameters by Electrode</i>	62
4.3.2	<i>Photometry</i>	63
4.3.3	<i>On-site Arsenic Species Separation</i>	64
4.3.4	<i>Water Samples</i>	65
4.4	LABORATORY METHODS AND SETTINGS	66
4.4.1	<i>Species Detection Methods</i>	66
4.4.2	<i>Atomic Absorption Spectrometry</i>	66
4.4.2.1	Determination of As(III) and Total Arsenic Using Hydride Generation - Atomic Absorption Spectrometry.....	67
4.4.2.2	Determination of As(III), As(V), MMAA, and DMAA Using Field Separation and Graphite Furnace - Atomic Absorption Spectrometry	68
4.4.3	<i>Determination of Multiple Elements Using Inductively Coupled Plasma - Atomic Emission Spectrometry</i>	69
4.4.4	<i>Determination of As(III), As(V), MMAA, and DMAA Using High-Performance Liquid Chromatography - Inductively Coupled Plasma - Mass Spectrometry</i>	70
4.4.5	<i>Other Analytical Methods</i>	71
5	RESULTS AND DISCUSSION.....	72
5.1	DIGITAL ATLAS	72
5.1.1	<i>Data Check - Measuring Tape vs. Digital Determined Lengths</i>	73
	<i>Browsing the Atlas</i>	74
5.1.1.1	Navigation tools.....	75
5.1.1.2	Viewing tools.....	75
5.1.1.3	Working tools	76
5.1.1.4	Groups and Layers	76

5.1.1.5	Groups and Individual Layers of the Atlas	77
5.1.1.6	Legends of the Layers in the Group Hydrochemistry	79
5.2	ANALYTICS.....	82
5.2.1	<i>Data Quality Check with Charge Imbalance</i>	82
5.2.1.1	Charge Imbalance by PHREEQC	83
5.2.1.2	Measured vs. Calculated Specific Conductance after Rossum (1975)	83
5.2.1.3	Charge Imbalance by WATEQ4F	84
5.2.2	<i>Iron Species Check</i>	85
5.2.3	<i>Arsenic Species Check</i>	86
5.2.4	<i>Description of the Analysis Results</i>	87
5.2.4.1	Cl-As-Correlation in Geothermal Fluids	87
5.2.4.2	Comparing HG-AAS to HPLC-ICP-MS	88
5.2.4.3	Ion exchangers: Acetic acid vs. Hydrochloric acid Conditioning	91
5.2.4.4	Species determination: Ion exchangers vs. HPLC-ICP-MS	93
5.2.4.5	Modeling As Species	96
5.3	HYDROGEOLOGY	97
5.3.1	<i>Clustering the Water Samples</i>	97
5.3.2	<i>Hydrogeological Model</i>	101
5.3.3	<i>Remarkable Thermal Features</i>	102
6	SUMMARY AND RECOMMENDATIONS	104
7	ACKNOWLEDGEMENTS	107
8	REFERENCES	109
9	APPENDIX	114

List of Abbreviations

AAS	atomic absorption spectrometry
AES	atomic emission spectrometry
As	arsenic
As(III)	inorganic trivalent arsenic, can be H_3AsO_3^0 , H_2AsO_3^- , HAsO_3^{2-} , AsO_3^{3-}
As(V)	inorganic pentavalent arsenic, can be H_3AsO_4^0 , H_2AsO_4^- , HAsO_4^{2-} , AsO_4^{3-}
As(T)	total arsenic
C/A-code	coarse acquisition code
DEM	digital elevation model
dGPS	differential Global Positioning System
DL	detection limit
DMA	gaseous dimethylarsine, $(\text{CH}_3)_2\text{AsH}$
DMAA	organic dimethylated arsenic acid, without distinction between tri- or pentavalent species
DMA ^{III} A	organic trivalent dimethylated arsenic acid, can be $(\text{CH}_3)_2\text{As}(\text{OH})$ or $(\text{CH}_3)_2\text{AsO}^-$
DMA ^V A	organic pentavalent dimethylated arsenic acid, can be $(\text{CH}_3)_2\text{AsO}(\text{OH})$ or $(\text{CH}_3)_2\text{AsO}_2^-$
EDL	electrodeless discharge lamp
EDTA	ethylenediaminetetraacetic acid
EPA	Environmental Protection Agency
GB	giga byte
GCP	ground control point
GF-AAS	graphite furnace - atomic absorption spectrometry
GIS	geographical information system
GPS	Global Positioning System
HG	hydride generation
HCL	hollow cathode lamp
HPLC	high performance liquid chromatography
ICP	inductively coupled plasma
mL	milliliter
MMA	gaseous monomethylarsine, $(\text{CH}_3)\text{AsH}_2$
MMAA	organic monomethylated arsenic acid, without distinction between tri- or pentavalent species
MMA ^{III} A	organic trivalent monomethylated arsenic acid, can be $(\text{CH}_3)\text{As}(\text{OH})_2$, $(\text{CH}_3)\text{AsO}_2(\text{OH})^-$, $(\text{CH}_3)_2\text{AsO}_2^{2-}$
MMA ^V A	organic pentavalent monomethylated arsenic acid, can be $(\text{CH}_3)\text{As}(\text{OH})_2$, $(\text{CH}_3)\text{AsO}_2(\text{OH})^-$, $(\text{CH}_3)\text{AsO}_3^{2-}$
MS	mass spectrometry
mV	millivolt
m/z	mass-to-charge ratio

nm	nanometer
NPS	National Park Service
p-code	precise code
PE	Polyethylene
ROA	range of analysis, standard deviation or square root of the variance
SPE	solid phase extraction (ion exchanger)
TMA	gaseous trimethylarsine, (CH ₃) ₃ As
USGS	United States Geological Survey
UTM	Universe Transverse Mercator
w:v	weight per volume
WHO	World Health Organization
WNCTA	West Nymph Creek Thermal Area
YNP	Yellowstone National Park

Abstract

Fast changing geothermal features characterize the Yellowstone National Park, USA. High-resolution aerial images were taken to map the hydrothermal study area. The combination of a digital camera and a low flying (< 100 m) helium balloon was a cost and time effective method to get a status quo of the feature's form and size. The resulting aerial overview has a resolution of 2.5 cm and is presented in a multilayer digital atlas, providing a basis for further surveying. Ground survey included mapping and on-site hydrochemistry of 18 major hydrothermal features. Arsenic concentrations are known to be elevated in Yellowstone (1.7 ± 2 mg/L) - therefore, beside trace element analysis with ICP-AES, three techniques for As speciation were applied: HG-AAS, HPLC-ICP-MS, and on-site SPE with GF-AAS. Surprisingly low total As concentrations made an evaluation of the different methods difficult. Grouping the water samples revealed two water types: steam heated waters (type I) and waters with a deep thermal origin (type II). Thus, a known hydrogeological model (White et al. 1988) is checked for its applicability to the study area.

1 Objectives and Deliverables

Yellowstone National Park (YNP) in Wyoming, USA, is known for its geothermal activity with more than 10,000 hot springs, fumaroles, geysers and mud pots. The Yellowstone hotspot, located beneath the National Park, is the origin of the thermal activity of that area. In some regions of the Park the geothermal activity has not changed in several years, other areas undergo significant changes over short period of time. The backcountry area West Nymph Creek Thermal Area (WNCTA), north of the Norris Geyser Basin in the northwestern part of the Park, is an area of interest. Located on the Norris Mammoth corridor, increasing geothermal activity was observed in the Norris Geyser Basin since the early 1990's combined with decreasing geothermal activity in the Mammoth area. No detailed or documented investigations have ever been done in this area.

Hydro- and geothermal features with different sizes, activities and hydrochemistry arise, develop and disappear. Since its inauguration as first National Park in 1872, many mapping and research campaigns repeatedly investigated the geology, the hydrogeology, and the hydrochemistry of Yellowstone. Until now, it took too much time to map the huge number of geothermal features in a relative short period to get the status quo of form, size, activity and chemistry. Possible trends of changing structures might not be detected.

Furthermore, Yellowstone's geothermal waters show high concentrations of trace elements at a high variability. Arsenic concentrations are commonly high in thermal fluids associated with active volcanism and shallow magmatism. This study focus on the distribution of As in thermal features of the West Nymph Creek Thermal Area of the Yellowstone National Park and the different possibilities for water sample preservation and the corresponding analytical procedures for the determination of the arsenic species. Arsenic concentrations typically range from 0.1-6 mg/L with a mean (\pm s.d.) of 1.7 ± 2 mg/L for 390 water samples done by the USGS. Dissolved As concentrations vary because of several reasons: the physical processes of boiling that causes increases in concentration and the mixing of deep hydrothermal waters with shallow ground water that causes decreases in concentration.

Different arsenic species are found in natural waters of the Yellowstone National Park at concentrations up to 4 mg/L. Two adjacent hot springs may present a pH from acid to alkaline, reducing to oxidizing conditions, temperature from boiling to atmospheric and trace element concentrations from below detection limit up to mg/L range.

1.1 Objectives

As fast changing geothermal features require a detailed mapping, a hydrogeological and hydrochemical status quo of the backcountry study area West Nymph Creek Thermal Area is set. Traditional ground survey is combined with an innovative low-cost aerial mapping. On the long term, this data will help to interpret periods and trends of changes for the geothermal features in this very active area.

Furthermore, different arsenic speciation techniques are applied.

- Conduct ground mapping of the geothermal features with a parameter catalogue to collect information on location, shape, gas activity, turbidity and others. Perform on-site hydrogeochemical investigations.
- Realize high-resolution aerial mapping with a resolution in the centimeter range with a custom-made and cost effective low flying platform.
- Lay out a temporary survey grid and determine the exact position of the ground control points with a differential Global Positioning System (dGPS). Furthermore, compare the accuracy of the dGPS to on-site measurement of lengths.
- Present a multi-layer GIS (geographical information system) atlas with the processed aerial pictures, mosaicked to an aerial overview, the digitized features, thematic maps, and hydrochemical data. Attach the on-site data from the survey, as well as the analytical results, as databases to the atlas.
- Review literature and interpret the hydrogeological model of the Norris-Mammoth corridor (White et al. 1988) for its applicability to the West Nymph Creek Thermal Area.
- Check if the proposed grouping of the hydrothermal waters (White et al. 1988) of the Norris Geyser Basin is applicable to the study area and check the documented As/Cl correlation (Stauffer and Thompson 1981).
- Check the hydrothermal waters on reported high arsenic concentrations and take water samples for trace element analysis.
- Compare two methods for arsenic species separation: on-site speciation by solid phase extraction (SPE) vs. species separation from preserved sample by high performance liquid chromatography (HPLC). Furthermore, compare four methods for total arsenic determination.

1.2 Deliverables

The major deliverables of this master thesis were aimed to be:

- Proving the applicability of a helium-filled latex balloon in combination with a commercial digital camera as effective and low cost method to document spatial changes of geothermal areas.
- Presenting a multi-layer digital atlas, combining the mosaicked aerial overview, the digitized features (e.g. hot springs, fumaroles, mud pots, drainages), a DEM (digital elevation model) of the Yellowstone National Park, thematic maps (e.g. topography base map, roads, boundaries, calderas, rivers, geology), and hydrochemical data. Different databases (e.g. locations and characteristics of the analyzed sites, on-site and laboratory data on hydrochemistry, arsenic speciation) are attached to the digital atlas.
- Grouping and characterization of the hydrothermal waters of the study area, allowing statements if the hydrogeological models from the Norris Geyser Basin and the Norris-Mammoth corridor are applicable to the West Nymph Creek Thermal Area.
- Providing recommendations for As speciation methods. Comparing advantages and limitations of solid phase extraction versus liquid chromatography. Furthermore, the comparison of two conditioning methods of the ion exchangers should provide information about future As speciation.

2 Yellowstone National Park

2.1 Introduction - A Land of Scenery

The Yellowstone National Park is located in the northwestern part of the State Wyoming with small parts in Montana and Idaho, USA (Figure 1).



Figure 1: Location of the Yellowstone National Park (YNP) in the northwestern part of Wyoming, USA (modified from Microsoft AutoRoute 2004)

Majestic mountains, dazzling arrays of steaming geysers, colorful hot springs, mud pots and magnificent wildlife - bison, bears, elks, and moose - are among the world-famous features of Yellowstone National Park. The Yellowstone plateau has an average altitude of about 2,000 to 2,500 m. Since the establishment as the world's first national park in 1872 with an area of 8,987 km², its riches have largely been protected through the efforts of generation after generation. The park's status as World Heritage Site and a Biosphere Reserve affirm its international recognition as a unique place worthy of preservation. Its relatively pristine condition as a naturally functioning ecosystem makes it an ideal place to do research on many subjects. More than 10,000 hydrothermal features, including 200 geysers, numerous hot springs, mud pots and fumaroles are found here. Hydrothermal legends as Old Faithful Geyser, Steamboat Geyser as the world largest geyser and Grand Prismatic Spring as the world's third largest hot spring are located in the Yellowstone National Park. The Continental Divide is the major watershed that cuts through the

southwestern part of the Park. Runoff south of the watershed flows mainly into the Snake River and the Falls River to the Pacific Ocean. Rivers north of the Continental Divide (Gibbon River, Firehole River, Gallatin River, Yellowstone River) discharge via Madison River to the Missouri and finally to the Gulf of Mexico.

Precipitation ranges from 260 mm at the north boundary to 2050 mm in the southwest corner. Average temperatures range from -13°C in January up to 27°C in July at Mammoth Hot Springs.

2.2 Geology of the Yellowstone National Park

2.2.1 Pre-Quaternary Geology

The geologic story of the Yellowstone Country begins with 2.7 billion-year-old Precambrian basement rocks, mostly pink granites and gneisses found in the Gallatin Range and the Absaroka Range at the north-central edge of the Park and in the Beartooth Mountains in the northeast outside the Park. Potassium feldspar is responsible for the pink color of the plutonic rocks (Figure 2). During a second period of rock formation, 1.5 billion years ago, dark magma injected cracks in the older Precambrian rocks (diabase dikes).

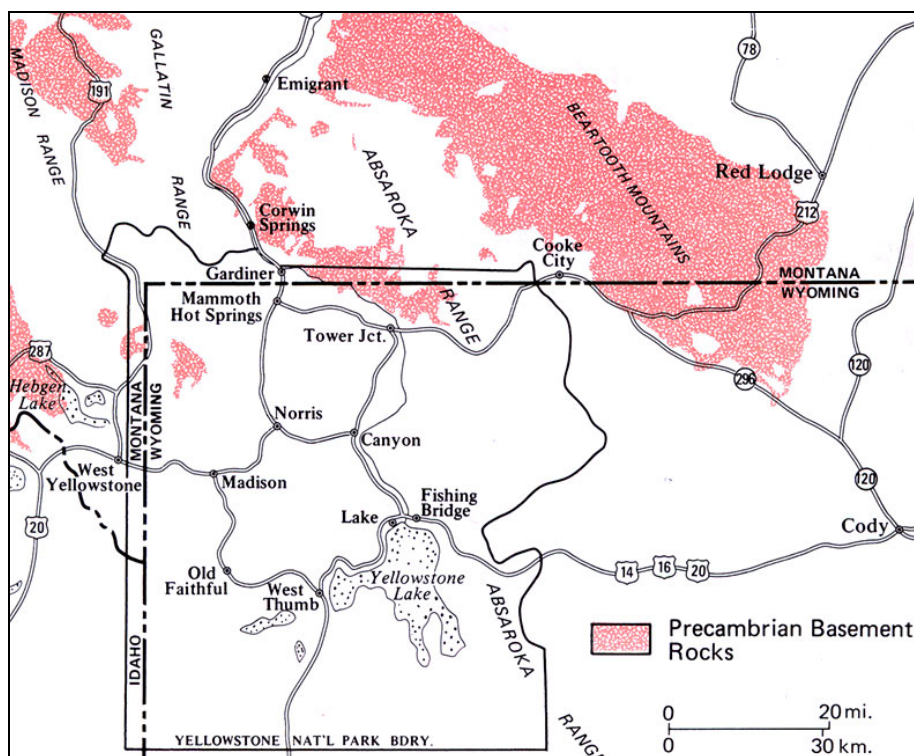


Figure 2: Exposed Precambrian Basement Rocks in the Yellowstone County (Fritz 2003)

The Precambrian formation of metamorphic and igneous rocks was apparently followed by a long period of uplift and erosion in the Yellowstone region that brought them to the

surface (Fritz 2003). During the Paleozoic era, from 570 million to 245 million years ago, marine conditions prevailed in the Yellowstone region. The shoreline probably ran south to north through what are now Colorado, Wyoming, and Montana. Limestones, sandstones and shales are the evidence for deep seafloor sedimentation during the Paleozoic. The Mesozoic era, from 245 million to 66 million years ago, was characterized by strong sea level fluctuations. At times, the Yellowstone region was covered by the ocean, at other times it was land. Many different types of sediments were deposited in shallow seas, swamps, lakes and rivers (Smith and Siegel 2000). During the late Mesozoic and early Cenozoic, 100 million to 50 million years ago, a period of uplift and mountain building called the Laramide orogeny occurred as the North American plate collided with the Pacific oceanic crust. A long linear mountain chain was shoved up - the Rocky Mountains. Soon after the uplift, from 50 million to 40 million years ago, in the early Tertiary, volcanoes started to erupt in the Yellowstone Country (Idaho, Wyoming and Montana). Deposits of this period are referred to as the Absaroka Volcanic Supergroup, a group of andesitic lava flows, basalt flows, airfall ash, mudflow conglomerate and stream gravel. Following the period of Absaroka volcanism, only uplift, stretching and erosion occurred in the park until volcanism started again about 2.5 million years ago to produce the Yellowstone Plateau volcanic field (Fritz 2003).

2.2.2 Volcanism in the Quaternary

The history of Quaternary explosive volcanism is characterized by three major volcanic cycles - each resulting in the formation of a large caldera and the deposition of pyroclastic rhyolitic lava (Figure 3).

The first and biggest eruption occurred 2 million years ago and ejected about 2,500 km³ of rhyolitic tuff. Rock layers of ash-flow tuff are called Huckleberry Ridge Tuff and reach maximum thicknesses of 150 to 750 m. The second, smaller eruptive cycle happened around 1.3 million years ago, just outside the actual Yellowstone National Park in the Island Park area of Idaho. A total of 280 km³ of pyroclastic flow form the Mesa Falls Tuff in Idaho with a thickness up to 150 m. The third eruptive cycle climaxed about 630,000 years ago and resulted in 1,000 km³ of the Lava Creek Tuff that today covers 60% of the Park's surface. The caldera of this last major volcanic cycle has a size of 45 km to 75 km. About 30 smaller post caldera flows filled much of the caldera with thick rhyolitic lava. One of these post-caldera eruptions, less than 150,000 years ago, left a secondary caldera what is now West Thumb of Yellowstone Lake. Most recent volcanic activity occurred 70,000 years ago and built the Pitchstone Plateau flow in the southwest of the Park (Smith and Siegel 2000; Fritz 2003).

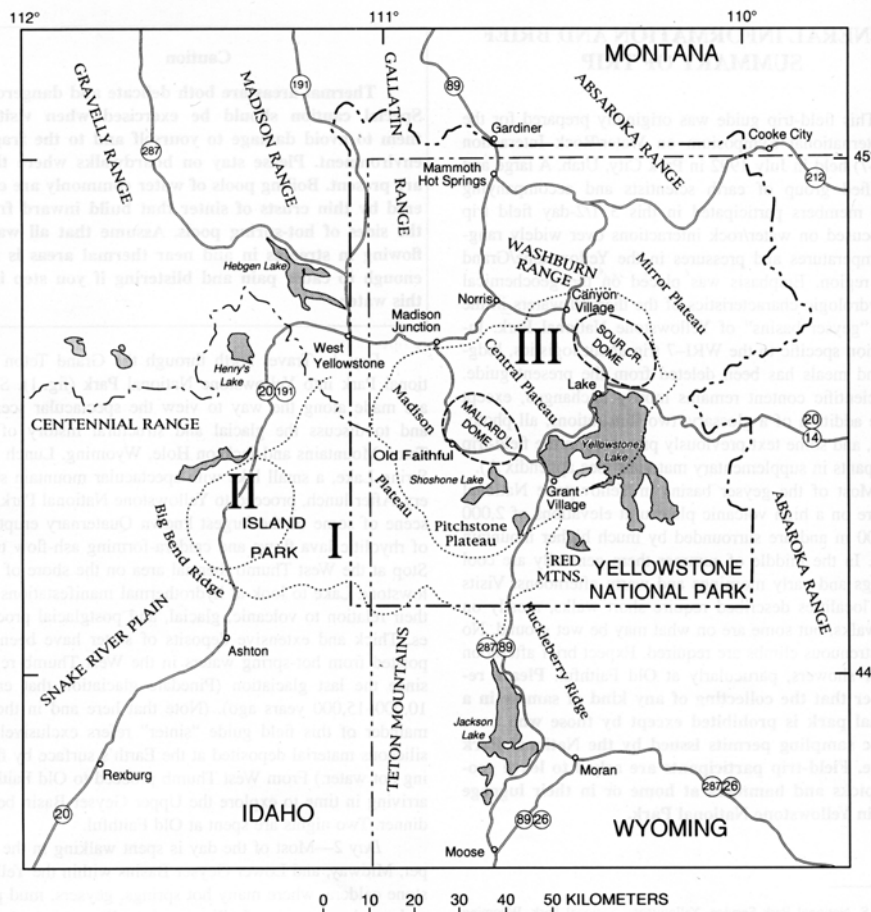


Figure 3: Extension and location of the three (I, II, III) youngest Yellowstone calderas, formed 2, 1.3, and 0.6 Ma ago (White et al. 1988).

The three Yellowstone caldera eruptions were 250, 28, and 100 times bigger in volume than the 1991 eruption of Mount Pinatubo in the Philippines (about 7 km³ of pyroclastic flow and ash). Almost the complete area of Northern America was covered by light volcanic ash particles from Yellowstone's giant eruptions 2 million years and 630,000 years ago (Smith and Siegel 2000).

2.2.3 Glaciers Carve the Landscape

Apart from volcanic eruptions and post caldera lava flows, advancing glaciers shaped the landscape of Yellowstone Country. Two major glaciation stages during the Pleistocene Ice Age are especially important for Yellowstone. The earliest, the Bull Lake glacial event, was between 160,000 and 130,000 years ago. The more recent Pinedale glaciers formed between 70,000 and 13,000 years ago and left the most obvious features. Ice thickness reached up to 1,200 m. Later, smaller glaciers and volcanic activity destroyed much of the evidences of the earlier glaciers (Fritz 2003). Today, only small glaciers are found in the Teton Range in above 3,300 m.

Interactions occurred between the glaciers and the Yellowstone hotspot beneath them. On a relatively small, local scale, meltwater from ice seeped underground and triggered hydrothermal or phreatic eruptions of steam and hot water, producing craters up to 1,300 m wide. Phreatic craters are well known around the east side of the Yellowstone Plateau. They include Indian Pond, Mary Bay, and other small lakes and bays on the north end of the Yellowstone Lake. When a glacial lake was suddenly drained, the confining pressure on underground hot water reservoirs was lowered locally resulting in violent hydrothermal explosions (Smith and Siegel 2000).

2.2.4 The Yellowstone Hotspot

Traditional hotspot theory implies that hotspots form where hotter or molten rock rises from the earth's core-mantle boundary due to variations in rock temperature and densities (Figure 4). For the Yellowstone hotspot, a newer theory suggests that the roots of the hotspot are located at only 200 km depth. The earth's crust has been stretching apart for more than 17 million years in a wide area of the western United States, creating the Basin and Range Province. The direction of this stretching process is southwest - northeastward at an annual rate of about 1.2 cm. This weakened region of the crust is characterized by alternating north-south mountain ranges and north-south valleys that extent from the Tetons/Yellowstone through southern Idaho, southeast Oregon, western Utah, Nevada, and into southern California. The hotspot's formation may result from the interaction of rising molten rock with the stretched and weakened zones in the Basin and Range Province. As the North American plate moved southwestward over the hotspot, latter bulged upward the lithosphere in a broad area before triggering caldera-forming eruptions. Smaller rhyolitic lava eruptions followed, succeeded by several basalt lava flows. The Snake River Plain, once higher than today, sank as much as 600 m after the hotspot passing. High Mountains, like the Wasatch Range in Utah and Idaho, that once crossed the Snake River Plain were eroded. (Smith and Siegel 2000; Fritz 2003).

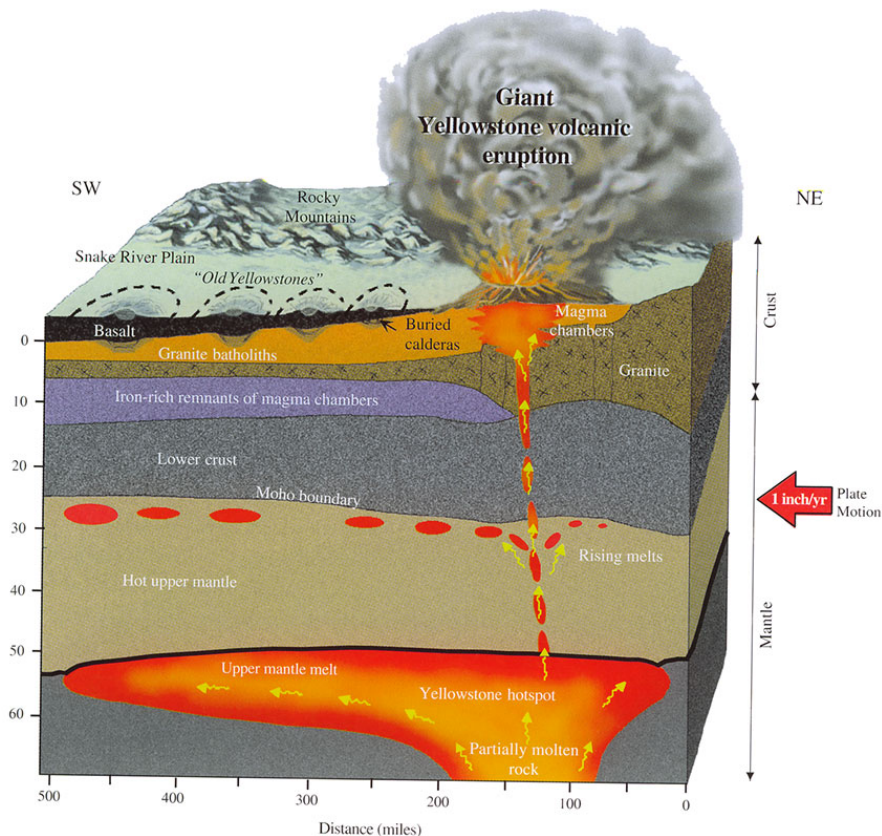


Figure 4: Cross section of the Yellowstone hotspot. Partially molten rocks rise from the hotspot and are sheared off by the overlying North American plate, which moves southwest at 2.5 cm per year. Some molten rock rises upward, through the crust-mantle boundary, melting overlying rock to create a magma chamber feeding Yellowstone's volcanic eruptions. Granite batholiths and iron-rich rocks beneath the Snake River Plain are remnants of old magma chambers left in the wake of the hotspot. Later basalt eruptions covered the Snake River Plain (Smith and Siegel 2000).

Today's hotspot below Yellowstone National Park consists of a column (mantle plume) of hot and molten rock are located at about 80 km depth. Plate tectonic forces share off gigantic basalt blobs and raise them toward the surface. Passing the lower crust, these basalt blobs melt silica-rich rock to create partially molten rhyolite. The magma chamber (granite pluton) extends from about 8 to 13 km beneath the surface. In the northeast of the Park it might be as shallow as 5 km beneath the surface (Smith and Siegel 2000).

2.2.4.1 Track of the Hotspot

About 17 million years ago, the nascent Yellowstone starting plume intercepted the lithosphere centered near the today's border of Nevada, Oregon, and Idaho. The McDermitt caldera at the border of northern Nevada and southeastern Oregon is the first remaining of the Yellowstone hotspot, the largest hotspot under a continent worldwide. Earlier appearances of the Yellowstone hotspot are still discussed controversially. As the North American plate drifted southwestward over the hotspot, a chain of about 100 calderas

formed stretching almost 800 km from the Oregon - Nevada - Idaho border, to Yellowstone National Park in northwestern Wyoming 2 million years ago (Figure 5).

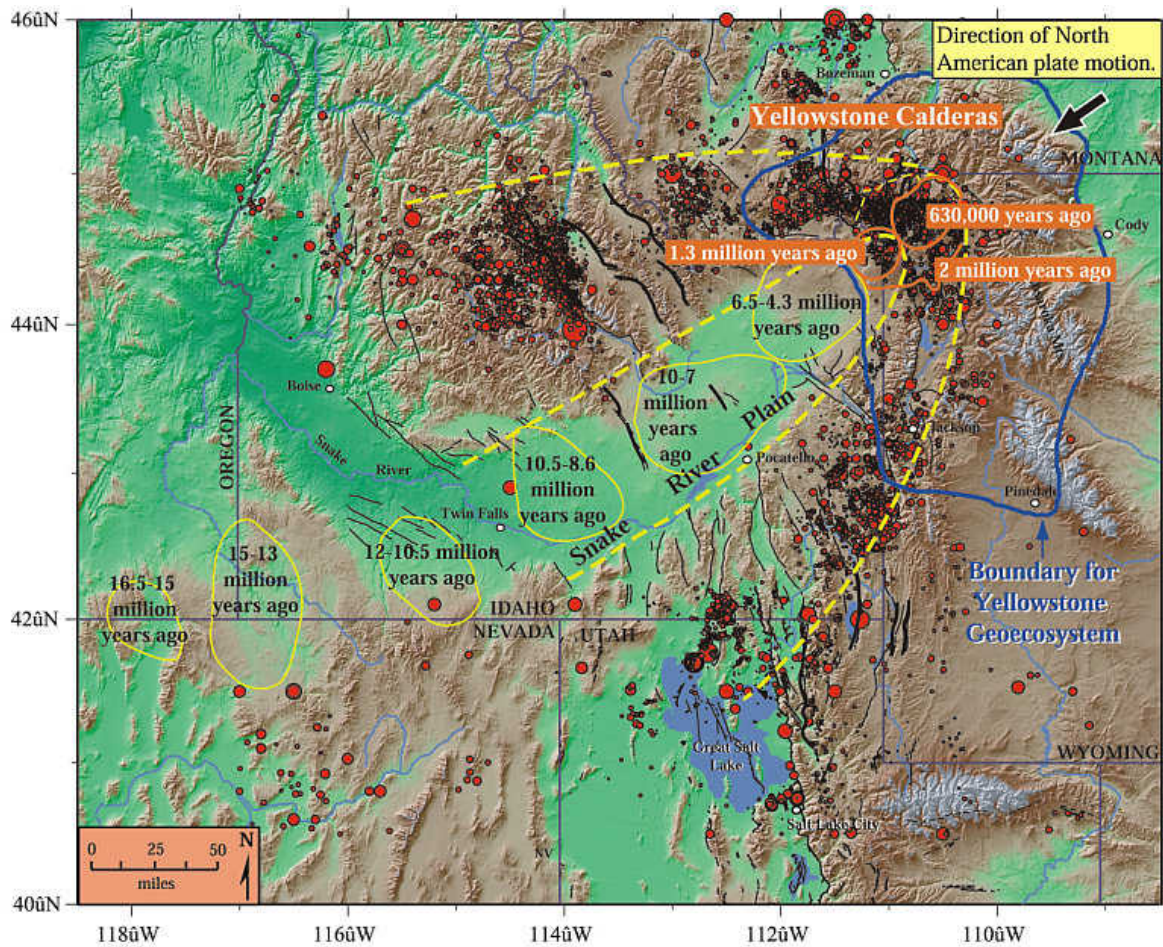


Figure 5: Track of the Yellowstone hotspot, which triggered about 100 caldera eruptions from seven major volcanic centers: McDermitt volcanic field (16.5-15 Ma), Owyhee volcanic center (15-13 Ma), Bruneau-Jarbidge volcanic center (12-10.5 Ma), Twin Falls volcanic center (10.5-8.6 Ma), Picabo volcanic center (10-7 Ma), Heise volcanic center (6.5-4.3 Ma), Yellowstone volcanic center (2.1-0.6 Ma) (Smith and Siegel 2000).

The average drifting speed of the North American plate during the last 16.5 million years above the Yellowstone hotspot was about 4.5 cm per year. From 16.5 million to 8 million years ago, the speed of drift was 6.1 cm annually, then abruptly slowed down to an average speed of about 3.3 cm per year. Tracking the Yellowstone hotspot back to the west from its present location at the Yellowstone Plateau, scientists were led into the problem of addressing the initial stages of the Yellowstone plume head. The segment containing the 10-Ma-and-younger rhyolitic volcanic progression is linear in both rate and trend and is reflected in the topographic depression of the eastern Snake River Plain, whereas the segment containing the 10-Ma-and-older rhyolitic progression includes calderas spaced 100-200 km northwestward apart. Not only the speed of drift changed, but also the direction from former southwest to south-southwest (Figure 5). Smith and Siegel (2000)

believe the origin of these changes in a slowdown and a change of direction of the plate movement.

In contradiction to the statement from Smith and Siegel (2000) about a change in plate movement direction, Pierce et al. (2000) believe the rising plume head may have interacted with and been diverted westward by the inclined Vancouver slab of oceanic Juan de Fuca plate. This interaction may explain the anomalously high apparent volcanic migration rate of about 7 cm per year from 16 to 10 Ma, which does not correspond with a known change in rate of the North American Plate. Today's hotspot migration rate is about 2.9 cm per year. About 16 millions years ago, the hotspot's actual feeding tail was located 260 km east of the McDermitt caldera in a straight, continuous line with the younger calderas. At that time, the hotspot was located underneath the northeastward tilting subduction zone of the oceanic lithosphere of the Juan de Fuca plate underneath the North American continental plate. The head of the rising mantle plume intersected with the overlaying Vancouver slab and was thus deflected west-southwestward, jutting out to the surface at the position of today's McDermitt caldera. The inclination of the Vancouver slab increased, meanwhile the continuous southwestward plate movement continued, which made the subduction zone depart southwestward from the hotspot. Since about 10 million years ago, without any deflections, the plume head rises straight from the feeding tail up to the surface. The southwestward deflection tapered off, which could explain the change in the hotspot track's direction to rather south-southwest and its apparently increased migration rate.

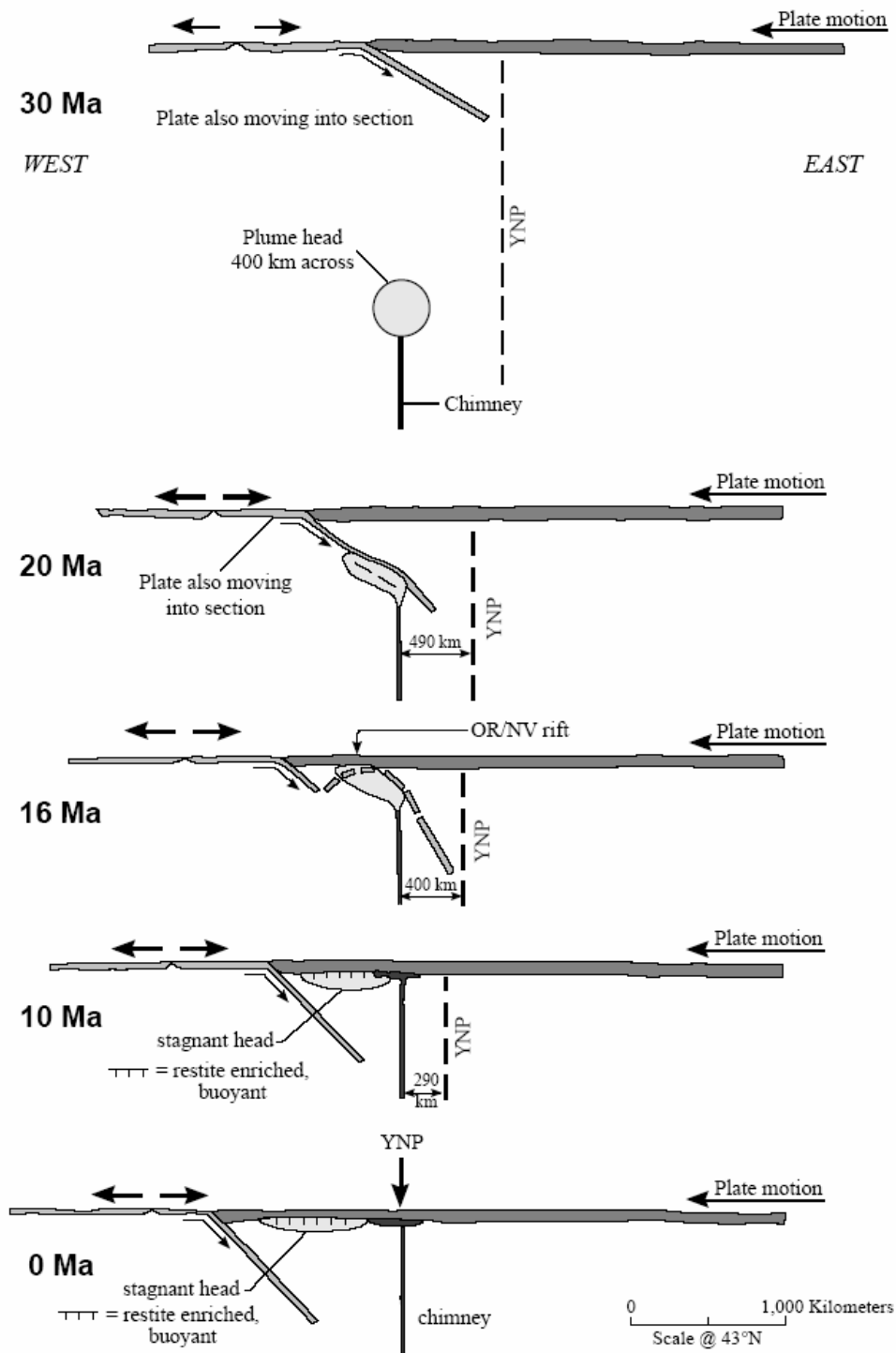


Figure 6: Postulated westward deflection of the Yellowstone plume head by buoyant rise up the inclined Vancouver slab. Time sequence from 30 Ma (top) to present (bottom) with fixed position of plume in the mantle. At 20 Ma, the plume head has intersected the inclined Vancouver slab and is being displaced westward. By 16 Ma the plume center is beneath McDermitt (along the Oregon/Nevada rift), about 260 km west of its feeding plume tail. As the plume flattens, the area of the plume in this cross section diminishes to about half because of spreading in the third dimension. The inclination of the Vancouver slab is shown to increase from 30 Ma to present (Pierce et al. 2000).

2.2.4.2 Resurgent Yellowstone

Even today, the Yellowstone Country is a geologically very active region. A large ellipsoid-shaped area in the central part of Yellowstone between Old Faithful, Fishing Bridge, and Canyon is uplifting at nearly 2.5 cm per year. An increase in number and strength of earthquakes results from this uplift which in turn alter some of the thermal and geyser activity. The Mount Borah earthquake in central Idaho in late 1983 increased the average time between the eruptions of Old Faithful geyser slightly. About 37 thermal features around Old Faithful and Geyser Hill experienced significant changes. Previously dormant springs have been reactivated and erupted again as geysers. The 1959 Hebgen Lake earthquake located northwest of Yellowstone caused similar increases in geothermal activity (Fritz 2003).

Current activity includes not only the high-temperature hydrothermal system but also various seismic activities and temporal pattern of historic fast uplift or inflation followed by deflation. Without resurgent magmatic activity, it is almost impossible to explain these processes. Further more, a variety of geophysical anomalies indicate that magma or partially molten rock may be present at depths ranging from about 5 to 10 km, and in the eastern half of the 630,000 year old Yellowstone caldera possibly as shallow as 3 km beneath the surface. These anomalies include low densities, large convective and conductive heat flows, a magnetic low and shallow calculated Curie-point isotherms and low seismic velocities. Further anomalies are a high seismic attenuation, a sharp increase in electrical conductivity at a depth of about 5 km, shown by magnetotelluric soundings, and a lack of seismic focal depths deeper than about 3 to 4 km beneath much of the caldera (Fournier et al. 1994).

After the last volcanic cycle, the resurgence of magma beneath the caldera formed two domes. The older Sour Creek dome formed after the third volcanic cycle 630,000 years ago. It is located in the northeastern part of the caldera, centered about 10 km north of Fishing Bridge and rises about 400 m above the surrounding countryside. The oval-shaped, pine covered hill has an extension of 10 to 16 km. The 150,000 year old Mallard Lake dome is located about 32 km southwest of Sour Creek dome, about 2 km north of Old Faithful. The dimensions of the oval-shaped dome are 11 to 8 km and 300 m above its surroundings. The presence of two resurgent domes suggests that two conduits feed Yellowstone's volcanism (Smith and Siegel 2000). Both domes are interconnected by the 153,000 year old Elephant Back fault zone, outcropping between the domes and reaching 2,600 m in altitude.

Many leveling surveys on different isolated spots of the Yellowstone caldera floor were done over the last 20 years. The results show that periods of uplift are followed by periods of subsidence. The average rate is about ± 20 mm/year. Since 1992, high resolution synthetic aperture radar (SAR) images from the European Space Agency satellites ERS-1 and ERS-2 made measurements of the year-to-year deformation of the whole caldera possible. With the created interferograms, the sources of deformation are localized

(Dzurisin et al. 1999). During the period from August 1992 to June 1997 Wicks et al. (1998, 1999) observed that the deformation centers changed on a time scale of 1 to 2 years between Sour Creek dome and Mallard Lake dome. The progression of uplift from the Sour Creek dome to the Mallard Lake dome may indicate that Sour Creek is closer, or at least has a preferential conduit, to the magma chamber below. Wicks et al. (1998) suggest that fluid reservoirs beneath the two domes interact via a second conduit. A third conduit to the northwest is suggested as an outlet from the caldera, feeding the shallow hydrothermal features in the Norris Geyser basin, and maybe connected to the Norris-Mammoth corridor.

Dzurisin et al. (1990) proposed two end-member models to explain the Caldera's floor uplift and subsidence. In the first model, injection of basalt near the base of the cooling rhyolite magma system is the primary cause of uplift. Rhyolite cools down and crystallizes in the uppermost part of the magma chamber, releasing gas and brine into the shallow hydrothermal systems. The subsidence of the caldera floor starts whenever the supply rate of basalt is less than the subsidence due to crystallization and loss of fluids. This model explains the Yellowstone caldera's uplift from 1923 to 1984 and the following subsidence from 1985 to 1995. The second model explains the uplift by pressurization of the deep hydrothermal system by magmatic gases released during crystallization of rhyolite and then trapped at lithostatic pressure beneath an impermeable self-sealed zone of mineral deposition. Subsidence occurs because of episodic hydrofracturing and injection of pore fluid from the deep lithostatic pressure zone into a shallow hydrostatic pressure zone. Caldera uplift and subsidence can continue for tens of thousands of years without an eruption.

2.2.4.3 The Norris-Mammoth Corridor

The Norris-Mammoth corridor is a complex subsidence structure of faults, dykes, thermal activity and vents, which extends north from Norris Geyser basin at least up to Mammoth, probably even further up to Corvin Springs Known Geothermal Resources Area. Electromagnetic (Stanley et al. 1991), seismic, and gravity data (Lehmann et al. 1982) confirm the assumption. Details are discussed in 2.2.6.

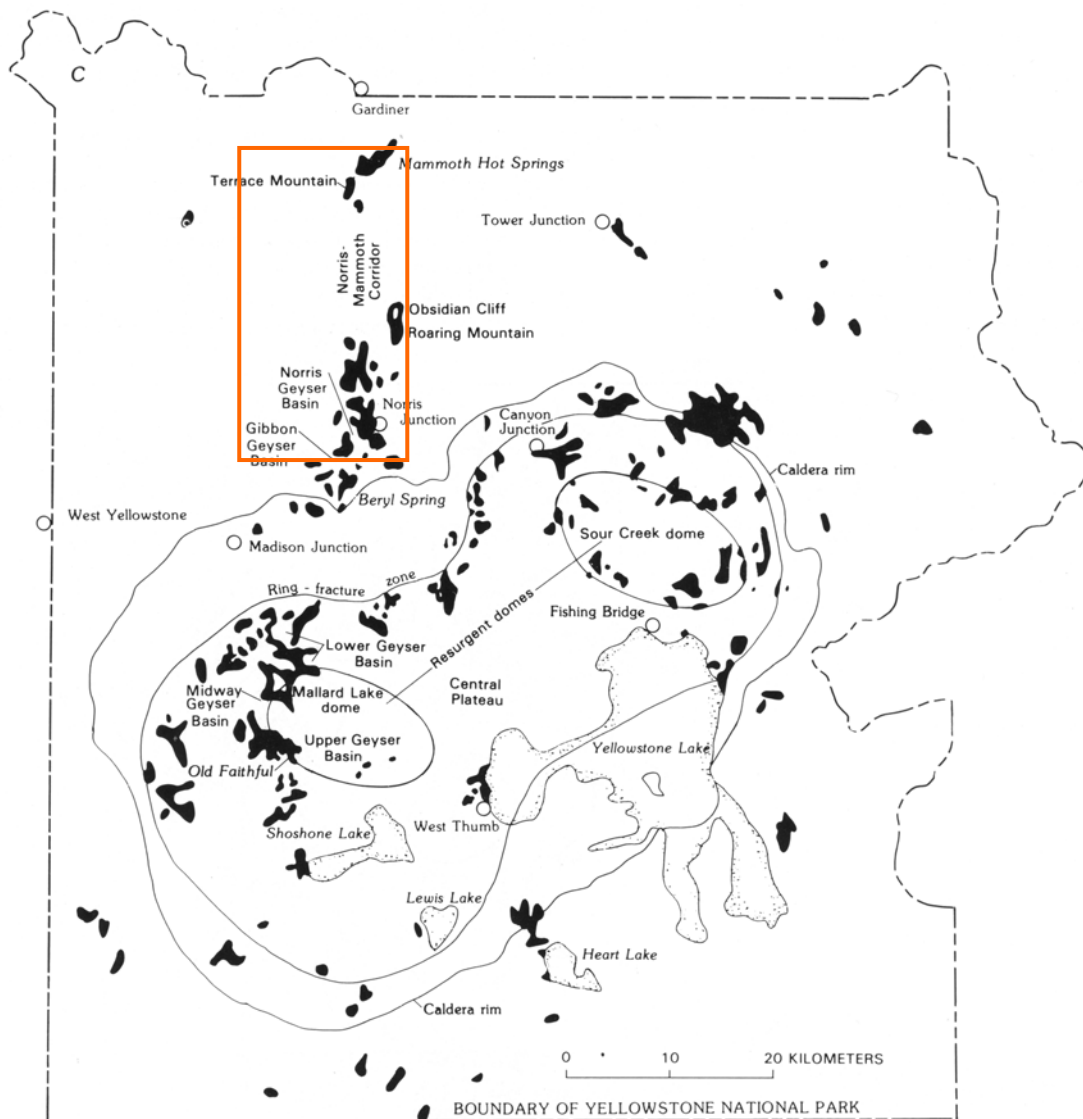


Figure 7: Yellowstone map showing the third cycle caldera rim (630,000 years old), the ring-fracture zone and the resurgent domes (Mallard Lake dome in the southwest and Sour Creek dome in the northeast). Both domes are interconnected by the Elephant Back fault zone (not shown in detail). The Norris-Mammoth corridor, the Norris Geyser Basin, and the WNCTA are marked with an orange square. The distribution of known active and fossil hydrothermal systems are displayed in black (modified after White et al. 1988).

The concept of a third conduit as outlet for hydrothermal fluids, proposed by Wicks et al. (1998), is supported by the observation that the two largest earthquake swarms ever recorded in the Park since 1972 occurred in that area. The change from uplift to subsidence in 1985 and the change from subsidence to uplift in 1995 are either initiated or accompanied by prolific earthquake swarms. The epicenters fell on a line extending from the northwest caldera rim toward the Hebgen Lake fault zone outside the Park; magnitudes up to 4.5 were recorded (Smith and Siegel 2000; Wicks et al. 1998). Most recent research reveals an inflation area of 30 to 40 km at the center of the proposed outlet (Wicks et al. 2002, 2003). A maximum uplift of 125 mm over the Norris Uplift Anomaly was detected from 1996 to 2002.

2.2.5 Hydrothermal Activity

Yellowstone is avowed for the world's largest number of geysers, hot springs, fumaroles (steam vents) and mud pots. Surface geothermal activity started after the last glaciation period, the Pinedale glaciation, about 13,000 years ago. These geothermal features are located in places where rainwater and snowmelt can infiltrate easily into the ground, become superheated by underlying magma and rise up to the surface again. Many geysers and hot springs are located in flat-bottomed valleys where lava flows did not converge, covered by permeable stream and glacier sediments that allow water to percolate into the ground. These spots are located on the northern ring-fracture zone of the youngest caldera rim, along the Norris-Mammoth corridor and on active faults in and outside the caldera. The abundant supply of recharge water comes primarily from snow that accumulates on the surrounding high mountains, based on isotopic investigations from Truesdell (1977).

Convection is the key to understand how geysers and hot springs work. Hot or molten rock at shallow depths about 4 to 5 km heats the overlying saline brine that carries heat upward by convection and heats in turn overlying fresh groundwater. Confined, deeper groundwater becomes superheated (about 350°C), exceeds the normal boiling point and when enough pressure builds up to overcome the weight and pressure of groundwater above, steam and hot water burst out of a geyser. About 200 to 250 hydrothermal features erupt as geysers each year. Hot springs occur when hot water pours out to the surface in the absence of a pressurized underground reservoir. Colorful mud pots or "paint pots" as e.g. Mud Volcano and Fountain Paint Pots form when there is a shortage of water and clayey minerals are dissolved from surrounding rocks. When only steam is released through vents without much hot water, the feature is a fumarole (Smith and Siegel 2000).

2.2.5.1 Hydrogeochemistry

Over the last 40 years, many investigations focused on the hydrogeochemistry of geothermal features in Yellowstone. Stable isotope studies revealed that more than 95%, maybe up to 99.9% of the circulating geothermal water in the caldera has a meteoric origin and only little magmatic fluids are mixed in (Craig et al. 1956; Fournier 1989). A general model of Yellowstone hydrothermal system assumes that in depths of about 4 to 5 km, infiltrating water is heated to about 350°C (inferred from enthalpy-chloride relations and Si-geothermometer). This saline brine contains about 400 mg/L Cl and high Na concentrations; the concentrations of SO_4^{2-} and HCO_3^- are low. The vapor phase, which coexists with this "parent water", is rich in CO_2 and H_2S (Fournier 1989).

The eastern part of the Park is dominated by geothermal features with little or no discharge (mud pots and fumaroles) as impermeable ash flow tuffs predominant in this area prevent infiltration of surface water. Large geothermal areas concentrate in the north and northwest of the Park. Meteoric water from the Gallatin Range recharges easily through permeable rhyolite flows. The water of these features has high Cl and SiO_2 concentrations at a near neutral pH (Truesdell et al. 1977; White et al. 1971). Waters at Yellowstone have a wide

range of compositions. The pH values range from 1 to 10, temperatures range from ambient to boiling, and high concentrations of H_2S , SO_4^{2-} , HCO_3^- , Cl^- and trace elements such as As and Hg are found here.

For this thesis, arsenic concentrations in geothermal waters are of special interest. First, Gooch and Whitfield (1888) detected arsenic concentrations in Yellowstone waters. Many survey campaigns detected As concentration in a range from 0.1 to 6 mg/L (Ball et al. 1998a, 1998b; Nordstrom et al. 2001). Arsenic is a typical element in geothermal fluids. At depths, most reservoir fluids are under saturated with regard to As minerals. High As concentrations are believed to result from leaching processes of the surrounding rocks by ascending hot fluids. Investigations on the vapor-liquid distribution for As in different hot springs of modern geothermal fields revealed distribution factors in the range of 0.001 to 0.01 at temperatures of 150 to 300°C (Ballantyne and Moore 1988). Only a small fraction of As, mainly $\text{As}(\text{OH})_3(\text{g})$, is separated into the vapor phase (= Type I waters at Yellowstone). At temperatures < 200°C and in the presence of $\text{HCl}(\text{g})$, $\text{AsCl}_3(\text{g})$ might predominate (Pokrovski et al. 2002). Stauffer and Thompson (1984) observed that the majority of As remains in the liquid phase during phase separation - this is the reason for the elevated As concentrations in Type II waters of Yellowstone, compared to Type I waters. The behavior of As in the liquid phase during phase separation is similar to the behavior of Cl. This fact was the reason why Ritchie (1961) was the first who observed a positive correlation of As and Cl in geothermal fluids. This observation is reinforced by many analyses of waters from Yellowstone's hot spring, showing an enrichment in As relative to Cl. One reason for the high As concentrations could be that high CO_2 concentrations increase arsenite hydrolysis and solubility from host rock (Stauffer and Thompson 1984). Another concept is that As accumulates in precipitates near the surface (Nordstrom et al. 2001).

The arsenic species distribution $\text{As}(\text{III})/\text{As}(\text{V})$ is extremely variable, ranging from predominance of reduced As(III) in hot springs to predominance of oxidized As(V) in drainages. The distribution of $\text{As}(\text{III})/\text{As}(\text{V})$ indicates that most, but not all, thermal features are dominated by arsenic (III) at the point of discharge. After discharge the arsenic redox state either remains reduced if H_2S and/or S_2O_3 are present or, in the absence of reducing agents, it rapidly oxidizes to As(V) by microbial catalysis. An exception are high Fe(III) concentrations, which can rapidly oxidize As(III) at low pH. Changes in pH, temperature, or the ratio of oxidized to reduced species concentrations might change the dominant oxidation mechanism between biotic and abiotic. Both biotic and abiotic processes are operative in controlling the redox state of As in thermal features and their overflows (Webster and Nordstrom 2002).

2.2.6 Study Area - West Nymph Creek Thermal Area (WNCTA)

The study area is called West Nymph Creek Thermal Area (WNCTA) and is located 4 km northwest of Norris on the Norris-Mammoth corridor. The extents of the study site range from 44°44'23" N to 44°44'45" N (Latitude) and from 110°44'34" W to 110°44'45" W (Longitude). Many geologists, geochemists and microbiologists have investigated the geology, the hydrochemistry, and the remarkable thermal activity of Norris Geyser Basin (see review White et al. 1988). No detailed and documented investigations have ever been done in the backcountry area of WNCTA.

After an evaluation of the existing aerial photographs and a first reconnaissance of the study area (September 2004), one could subdivide the site into three major areas of geothermal activity: a north group, a central group and a south group. The discharge of the geothermal features for the north group flows through the central and south group. The drainage of all the areas joins the Gibbon River, which finally joins the Madison River. The north group is characterized by many geothermal features, varying in size, color and activity. A large fumarole area located on the slope of a hill characterizes the central group. With geothermal features varying in size, color and activity, the south group is similar to the north group. In addition, a large wetland area is located in the south group. A young pine forest (about 15 years) from the Yellowstone's afterglow period surrounds all geothermal areas. Dense brushwood and dead-fall characterize the drainage.

White et al. (1988) present a hydrogeological model to explain the hydrothermal activity in the Norris-Mammoth corridor (Figure 8). A magma chamber is assumed to be centered near the vent of the 180,000 years old Obsidian Cliff flow, from where geothermal fluids at about 370°C, neutral in pH, rich in Cl⁻ and SiO₂, emerge to the north and to the south. To the north, extensive cooling and dilution by meteoric water takes place. These waters dissolve carbonate from pre-Tertiary sedimentary rocks, which precipitates upon the discharge at Mammoth hot springs and contributes to the formation of the travertine terraces. To the south, the 370°C hot waters undergo subsurface boiling with a steam-water separation. The gases CO₂ and H₂S, initially abundant, escape through channels and fissures. Near the surface, H₂S reacts with atmospheric O₂ and dissolves in condensing steam and local meteoric water, thereby causing the acid bleaching of an almost continuous zone southward to Norris Basin. Most residual chloride water remains and cools in the subsurface to about 270°C. For the study area, located south of the Obsidian Cliff on the Norris-Mammoth corridor, elevated sulfate and chloride concentrations at low pH values are expected.

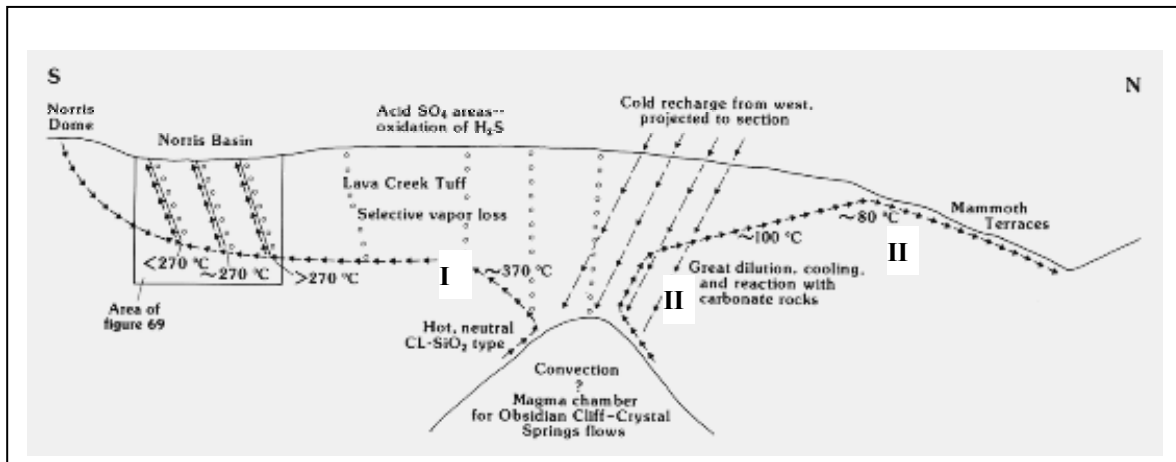


Figure 8: Hydrogeological model to explain the hydrogeochemistry in the Norris-Mammoth corridor (White et al. 1988). This north-south section identifies the magma chamber below Obsidian Cliff as heat source for convection of the hydrothermal fluids. Toward the south (I) steam-water separation, H_2S oxidation and surface alteration takes place. Toward the north (II) the hydrothermal fluids are diluted and cooled by infiltrating meteoric waters and dissolve carbonatic Pre-Tertiary sediments. The orange flash indicates the location of the West Nymph Creek Thermal Area on the Norris-Mammoth corridor.

Kharaka et al. (1991) propose a slightly different model with a disconnected magmatic body for the northern Mammoth hot springs area. Isotopic fractioning supports this model. High $^3\text{He}/^4\text{He}$ ratios in geothermal waters as in Norris and Mammoth indicate a direct release from deep reservoir. Low $^3\text{He}/^4\text{He}$ ratios are detected in all geothermal waters along the corridor. Stanley et al. (1991) give evidence of a magmatic body beneath Mammoth. Magnetotelluric and other geophysical surveys identified a partially molten area south of Bunsen Peak at a depth of 6 km.

White et al. (1988) differentiate among four different types of water in the Norris Geyser Basin. For the West Nymph Creek Thermal Area, 4 km northwest of Norris, this classification has to be checked for applicability.

- The fundamental water type in Norris Basin is a nearly neutral in pH and high in Cl and SiO_2 (contents of > 700 mg/L for each). Its SiO_2 content depends on its temperature and on the amount of precipitation. Temperatures below Norris are around 270°C . High initial SiO_2 and Cl concentrations correlate with the high temperature. Contents of SO_4 and of all inorganic C species are generally low.
- A second type of water is high in SO_4 and moderately high in Cl, with strong varying Cl/ SO_4 ratios. Low Cl concentrations (contents < 5 mg/L) indicate dilution by meteoric water. H_2S from a lower, reducing milieu oxidizes near the surface with atmospheric oxygen to form SO_4 (or H_2S oxidation with ferric iron from oxidized ash-flow tuffs).

- Acid Cl- SO₄ water is the most abundant water type in the southwestern part of Norris Basin. These meteoric waters contain sulfuric acid, probably obtained from the recharge area by oxidizing H₂S and native S. Near the crest of Norris Dome, another source of acid warm meteoric water seems to be located.
- Acid SO₄ with high temperature and rich in soluble constituents, leached from the local rock, is a minor water type. This water is generally close to boiling and is surrounded and underlain by saline waters of other types from which it is supposed to derive. Beside water vapor, the dominant gases are CO₂ and H₂S. H₂S oxidizes to SO₂ or SO₃.

In general, as geothermal fluids ascend adiabatically from the magma chamber water and steam separate. As pressure decreases at shallower depths, and at fractures or fissures, two major water types form in the Yellowstone National Park:

Type I water: steam, containing high concentrations of dissolved acidic gases like CO₂ and H₂S, rises and condenses or mixes with shallow groundwater. Chemical or microbial oxidation of H₂S forms H₂SO₄ or elemental sulfur, which precipitates or sublimates. Low thiosulfate (S₂O₃²⁻) concentrations were detected in most acid sulfate and acid sulfate-chloride springs due to the instability of thiosulfate at low pH values (Xu et al. 1998). The major characteristics of the type I water are low pH values, high concentrations of S(VI), high CO₂ partial pressure, and rare earth elements (REE) from reactions with surrounding rhyolite at concentrations of about 20-1130 nmol/kg Σ REE (Lewis et al. 1997). Ball et al. (2002) detected elevated Al concentrations from several mg/L to a maximum of about 100 mg/L.

Type II water: depleted of the gaseous compounds, this water is made up of the residual liquid phase. Characteristics of the type II water are a near neutral pH, lower concentrations of S(VI) and CO₂ partial pressure than detected in the type I waters. Type II waters present elevated concentrations of Si, Na and Cl. Often > 400 mg Cl/L is detected in deep (4-5 km) waters over the magmatic heat source, whereas concentrations of rare earth elements are low or even below detection limit (Lewis et al. 1997).

3 Methodology of the Geospatial Analysis

3.1 Introduction to Remote Sensing from Low Flying Platforms

Conventional aerial photography works with large format cameras and the pictures are normally taken from airplanes at 3000 to 6000 m altitude. With a photo scale ranging from 1:10,000 to 1:40,000 the vertically taken photo sequences have a standard resolution of 1 to 2 m. Usually they are updated only every few years for mapping or monitoring purposes of a region. Remote sensing from low flying platforms makes it possible to combine the advantages of terrestrial photography and conventional airborne aerial photography. Details become visible that will not be recognized on the ground or in conventional air photos and satellite images. Altitudes for low flying platforms range from a few meters up to several hundred meters above the ground. Photos are taken from manned or unmanned platforms by means of color, black-white or infrared films. High or low oblique aerial photos serve for a general overview of the survey site, whereas vertical photos are used for detailed survey and mapmaking purposes (Figure 9).

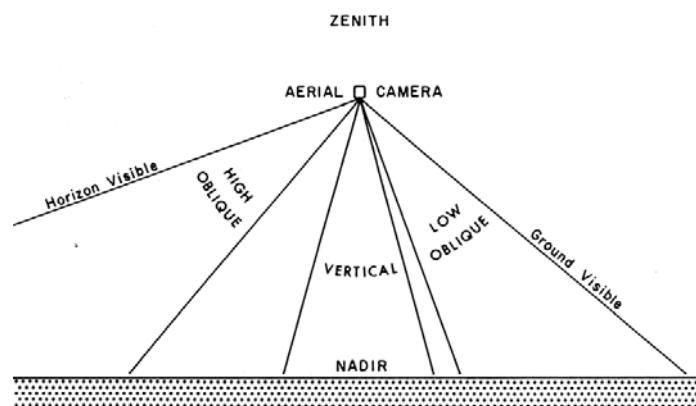


Figure 9: Different camera views for aerial photography (Aber et al. 1999)

Initially uncorrected images may be transformed into orthogonal photos when: (1) the camera's interior orientation (camera characteristics, information on lenses) is known, (2) the camera is orientated perpendicularly (90°) (or flight direction and tilt are known), and (3) a digital elevation model of the terrain is available, comprising x and y-coordinates of the images' center. If these data are not available, only the method with the x-, y- and z-coordinates of ground control points is possible. Becker (2004) gives a complete overview on low flying platforms like e.g. balloon, kite, airship and model airplane aerial photography.

3.1.1 Ground Control Points

For further editing and processing of the aerial photographs in a GIS-program (Geographical Information System), the pictures taken from the helium balloon (3.2.3) have to be georeferenced and rectified. To do so, sufficient ground control points with known coordinates were needed. The necessary density of control points depends mainly on the balloon's altitude above ground, the small format camera and the camera's focus. For georeferencing a picture, it needs to have at least three check points approximating an equilateral triangle. Every additional check point helps for further rectifying the aerial pictures.

3.1.2 Theory of GPS and DGPS

Based on preliminary tests in the late 1960's, the United States Department of Defense developed since the mid 1970's a satellite-based positioning system called NAVSTAR-GPS (Navigation Satellite Timing And Ranging - Global Positioning System). In mid 1980's, the Soviet Union developed a comparable military system: the GLONASS (Global Orbiting Navigation Satellite System). The advantage of the orbiting satellites is that they are difficult to locate from the antagonist and that they can be concentrated over a region of interest. A disadvantage of orbiting satellites is the less accurate positioning compared to satellites with a geostationary orbit.

In principle, the positioning with satellites is based on the measurement of distances by the determination of the delays of the travel time of the sent information. This requires perfectly synchronized satellites in order that all the satellites send the information at the same time. Therefore, satellites require accurate atomic clocks (rubidium/cesium) for GPS measurements. An additional satellite is required for synchronizing only: for position determination of a "2d fix" point (easting and northing) three satellites are required and four satellites are required for the position determination of a "3d fix" point (X, Y, and Z) (Merkel 2005 online).

The Global Positioning System (GPS), as it is called today, is a worldwide radio-navigation system based on a constellation of 21 operational satellites, additional three satellites in orbit as redundant backup, and their ground stations. The GPS achieved its full operational capability in June 1995, after the launch of the 24th satellite. Today more than 30 operational satellites orbit the earth. These satellites orbit the earth every 12 hours at an altitude of 20,200 km from where they send their signals (position) to the ground stations.

The American GPS system is equipped with two digital systems: the C/A-code (coarse acquisition code) and the p-code (protected code). The C/A-code sends information once a second and enables the possibility of an intentional haziness of the signal (Selective Availability). The p-code is sent every 0.1 seconds and contains more information for a

higher accuracy of the position determination. The p-code is encrypted and can only be decrypted with the corresponding code.

Specified in the Federal Radionavigation Plan (1999), GPS provides two levels of service: Standard Positioning Service (SPS) using the C/A-code and the Precise Positioning Service (PPS) using the p-code. The Standard Positioning Service is a positioning and timing service, which is available to all GPS users on a continuous, worldwide basis with no direct charge. The Precise Positioning Service is a primarily military positioning, velocity, and timing service, which is available on a continuous, worldwide basis to authorized users with cryptographic equipment, keys, and specially equipped receivers.

Limitations and typical sources of Global Positioning System errors are (Dana 1997):

- Ionosphere and Troposphere: as the satellite signal passes through the atmosphere it slows down.
- Signal Multi-Path: the satellite signal can be reflected off of objects such as tall buildings, mountains and other large rock surfaces. This causes the signal to increase its travel time.
- Receiver Clock Errors: the clock in a receiver is not an atomic clock as it is in the satellite and the built-in clock can generate small errors in timing.
- Ephemeris Errors: these are inaccuracies of the reported position of a satellite.
- Low Number of Visible Satellites: the fewer satellites signals the receiver receives will result in a less accurate location reading. Buildings, high terrain and trees are just some things that can block satellite signals.
- Bad Satellite Geometry: bad satellite geometry exists when the satellites either are located in a line or are closely grouped together.

Apart from these “natural” error sources, the Selective Availability (SA) is the intentional degradation of the Standard Positioning Service signals by a time varying bias. SA was activated in 1991 by the U.S. Department of Defense to limit and control SPS accuracy for civil users (USNO online 2005). Since May 1st 2000, the Selective Availability is definitively deactivated what increased GPS accuracy for all civil users.

The GPS was primarily conceived for positioning and velocity determination of moving objects (e.g. boats, trucks, and airplanes), and thus shows discrepancies for singular position determination. With activated Selective Availability and using the C/A-code, 95% of all position determinations (X and Y) were within a 100 m radius. If satellite positioning is used to determine the position of a stationary object, multiple position determinations are possible, resulting in a mean of the position and thus in a significant lower error. With a

determined mean of the position and without SA, 95% of all position determinations (X and Y) are within a 5 m radius. The error for the vertical positioning (elevation Z) is about 30 - 100% higher than the errors for the horizontal positioning (X and Y).

A way to correct the various natural inaccuracies in the GPS system is Differential GPS or "DGPS" that was developed in the late 1980's and early 1990's. Differential GPS involves the cooperation of two or more receivers, at least one that is stationary and another that is roving around making position measurements (Figure 10).

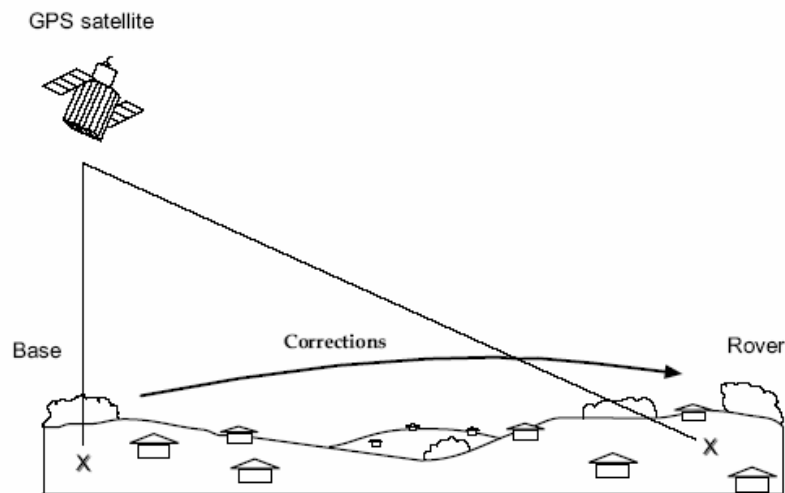


Figure 10: Differential GPS needs two receivers: a stationary base and a moving rover (Hofmann-Wellenhof and Lichtenegger 2001)

The stationary receiver, which might be a terrestrial base station or a satellite as well, is the key. It ties all the satellite measurements into a solid local reference. Depending on the distance from the base station, the real-time accuracy for DGPS measurements in horizontal and vertical orientation is in the sub-meter range under outdoor conditions. The horizontal accuracy after 45 minutes tracking satellites (mean of position) and carrier postprocessing is about one cm (Trimble 2005). The accuracy of the different systems using either the C/A-code or the p-code or using either the mean position or the singular determined position is presented in Table 1.

Table 1: Accuracy for GPS and differential GPS measurements varying with these parameters: C/A-code, p-code, singular measurement, and multiple measurements (mean of position).

System	GPS	Differential GPS
Principle	24 - 32 orbiting satellites	GPS and stationary terrestrial receivers
Discrepancy for singular measurement	± 25 m (with C/A-code) ± 10 m (with p-code)	Depends on distance to stationary receiver
Discrepancy with mean of position	± 5 m (horizontal X and Y) ± 8 m (vertical Z)	± 0.5 m (with C/A-code) < 1 mm (with p-code)
availability	worldwide	worldwide

3.2 Aerial Survey

3.2.1 Temporary Survey Grid

Using a small format camera with a 35 mm focus distance and a 24 by 36 mm film, one gets a picture section with an angle of 40° in x-direction and 60° in y-direction. Thus, a picture taken from e.g. 100 m altitude with a focus distance of 35 mm shows a section of 74 m in x-direction x 116 m in y-direction. Considering an average flight altitude of the balloon of 80 m above the ground, the picture section covers an area of 60 m by 92 m (Figure 11). A grid distance of 28 m to 28 m seems to be a reasonable convenience for the placements of the control points. In the field, due to natural restrictions (occurrence of hot springs, geysers, algal mats fumarole areas etc.), it was not always possible to establish the exact distance grid.

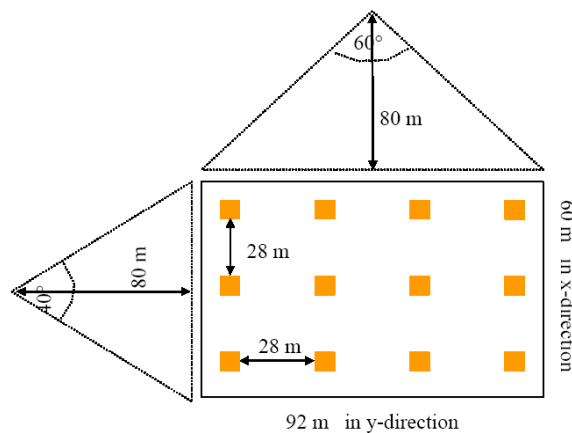


Figure 11: Picture section and calculated grid distance for 35 mm focus distance at 80 m altitude (Becker 2004)

The 171 temporary control points of the survey grid were marked with 1 m red-white-plastic stripes and laid out in a “X” form on the ground. The distance of 25 meter between each control point was estimated by footsteps.

3.2.2 Determination of the Coordinates

The position of the 165 control points was determined with a Trimble Pathfinder Pro XR differential GPS receiver combined with a Trimble TSC 1 data-logging unit, equipped with the corresponding Asset Surveyor v5.22 software. The device consists of a field computer, a backpack with the batteries, the receiver and an antenna. The instrument integrates a 12-channel GPS and offers real-time differential GPS and postprocessing options. The correction factors for the postprocessing calculation were taken from the reference station in Bozeman. The horizontal accuracy for the Trimble Pathfinder Pro XR differential GPS receiver with two minutes tracking satellites (120 time samples) and data postprocessing is about 0.5 m. To avoid any kind of distortions the mobile differential GPS antenna from the backpack was placed on the ground, in the center of the control point.



Figure 12: Differential GPS measurement of ground control point's coordinates

The position of another six ground control points was determined with a handheld Garmin-12 GPS device. This was because of good flight conditions an unscheduled area could be mapped and therefore six additional ground control points had to be fixed. The horizontal accuracy (95%) of the Garmin-12 after 2 minutes of satellite tracking is 5 meters.

3.2.3 Design of the Helium Balloon

An innovative and cost effective combination of ground survey and aerial photography for high resolution mapping of geothermal features was first tested in 2003 (Becker 2004). The construction to mount the camera at the balloon (Figure 13) was designed and built in Freiberg at the mechanical workshops of the faculty of geosciences and mining.

1. The latex balloon was able to carry about 1.5 kg. The camera weighted 0.46 kg and the construction including two 80 m lines approximately 0.7 kg, the difference of 0.34 kg between the maximum possible and the actual load provided sufficient lift. Filled with helium the balloon had a diameter of about 1.50 meter.
2. A plastic clip sealed the balloon tight to prevent helium leak.
3. Two small metal angles with holes for fixing the tether lines and the framework were fixed by two screws at the lower end of the balloon below the plastic clip (2). They served to connect the framework and the tether lines to the balloon and as an additional gas tight seal.
4. Two hollow aluminium sticks of 0.75 meter length attached in a 90 degree angle to the middle axis (8) formed the main part of the framework.

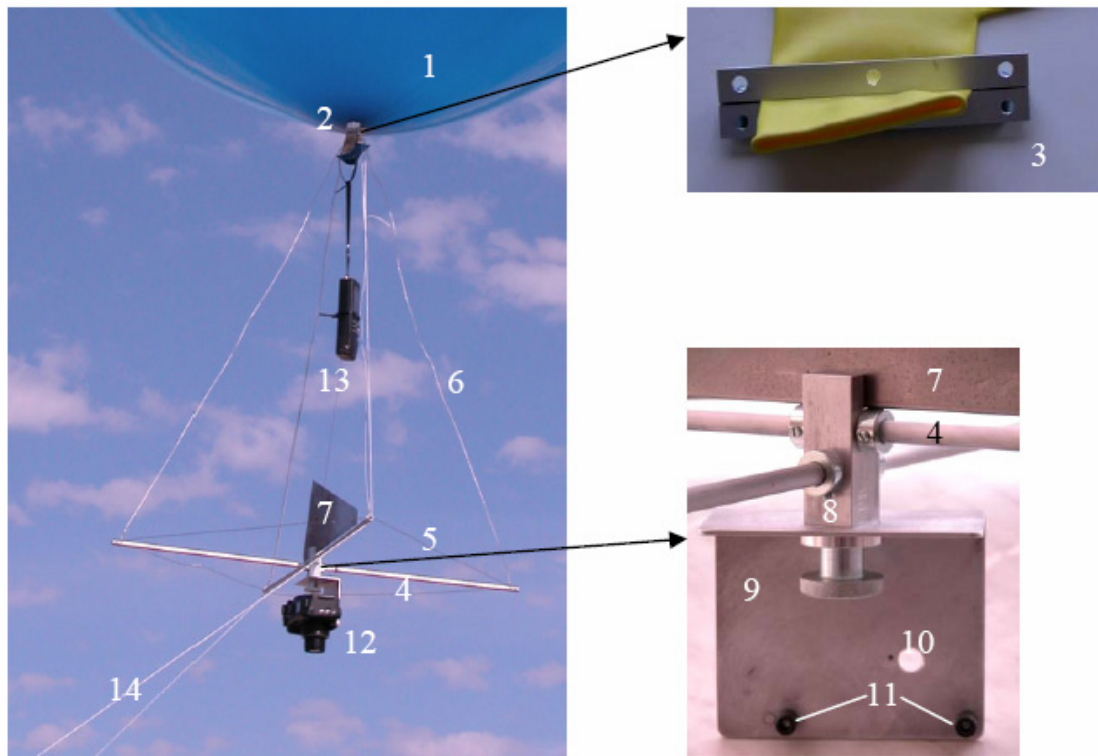


Figure 13: Setup of the custom made, light weight camera carrying construction

5. Two 1 mm thick, intertwined wires spun around the four ends of the aluminium sticks (4) and helped to stabilize the main carrying construction.
6. Four 1 mm thick, intertwined wires attached the camera carrying framework to the balloon (3).
7. The metal plate, designed to orientate the construction in the wind, was not used during the survey campaign because of low efficiency.
8. The middle axis connected the metal plate supporting the camera to the aluminium sticks framework (4).
9. One screw fixed the metal plate carrying the camera to the aluminium sticks framework (4).
10. A hole in the metal plate (9) served to fix the camera with a tripod screw.
11. Two small rubber stoppers supported the tripod screw to fix the camera.
12. The digital camera “Canon Power Shot G5” (5.0 M pixel, 4x optical zoom, focal length 7.2 – 28.8 mm, 35 – 140 mm equivalent to 35 mm film) equipped with an interval shot function took the aerial pictures.

13. In order to have more lift capacity, the handheld, GPS “GARMIN-12” was not attached to the framework. The 12-channel GPS receiver would be able to retrieve the balloon’s track on a map.
14. Two people controlled the balloon from the ground with the help of two 1.3 mm thick special nylon kite lines. To know the balloon’s approximate altitude, the lines were marked every 10 m.

3.2.4 Helium Balloon at Work

To raise the balloon with the camera construction, it had to be filled with a gas that is lighter than air. Therefore, the noble gas helium was used. Some advantages in the use of helium are that there are no dangers during working with the gas because it is non-toxic, environmentally friendly, not inflammable, stable and inert towards all other chemicals. By international norms, it belongs to the group of the non-hazardous material. Two 10-liter helium bottles were bought in Bozeman; one bottle contained 2 m³ He, enough to fill one balloon. Each bottle weighted about 20 kg and was transported in a backpack to the sampling site. Filling the balloon in the field was tricky because its 6-cm diameter opening was slipped over the special balloon-valve of only 1 cm diameter. During inflating, increasing pressure made it difficult to manually maintain the connection. When first inflating the balloon fast outpouring helium burned a small hole into the thin latex skin of the balloon. Duck tape was used to close the hole. The plastic clip (2 in Figure 13) completely sealed the inflated balloon. The next step was to fix the camera-carrying framework and then the camera itself to the balloon. Because of the diffuse loss of helium, the operation time was limited to approximately two to three days depending on weather and storage conditions.

The balloon was first launched on September 10th 2004, from 11:00 am to 11:30 pm in the southern part of the study area. The southern part showed the widest open spaces to learn to handle the balloon. Weather conditions on the first flight day were a covered sky, moderate temperatures and low to moderate winds from variable directions. The following camera settings were adjusted before lifting the balloon: the “Intervalometer” was set to one minute, auto focus, no zoom and an exposure time of 1/1000. The “Intervalometer” is a timer-program for the trigger of the camera that allows taking pictures automatically in a pre-set time interval. The short interval of taking the pictures should ensure the necessary overlap to enable the mosaicking of the images later. Two people controlled the balloon from the ground by two tether lines. Problems that occurred during the first track were uneven uplifting due to wind and turbulences of hot air masses above the geothermal features. The maximum altitude was about 60 meters. Winds picking up in velocity made the balloon bounce around so violently, that the framework tore the latex balloon. The camera and the frame crashed on the ground; the camera was so badly damaged that it had to be replaced. The 20 pictures from the recovered memory card showed a good quality and resolution, so the camera settings did not have to be changed for the next run. Before the

second balloon run on September 22nd an identical camera, a new balloon with thicker latex skin and one more bottle of helium were bought in Bozeman. To protect the camera in case of a second crash a Styrofoam protection was custom-fit around the camera.

Aerial photographs were taken on September 22nd, 24th, 25th, 26th and 27th 2004 (Table 2). Weather conditions were always allowing the use of the balloon: sunny, moderate temperatures and low to moderate winds. The camera settings from the first run (interval one minute, auto focus, no zoom) were maintained; except the exposure time was changed in dependence on the light conditions from 1/1000 to 1/1600 to 1/1800 and 1/2000. In order not to risk damaging the balloon while transporting it from one group of geothermal features to another through dense brushwood along the drainage, a second balloon was inflated in the northern group. While using two balloons, only the camera, the lines and the framework had to be transported from one area to the next.

Table 2: Overview aerial photographs

Date	Group location	Pictures	Comments
10.09.2004	South	15	Balloon crash
22.09.2004	South	70	
24.09.2004	Central	48	Inflate second balloon
25.09.2004	North	40	Memory card failure
26.09.2004	North, Central	89	
27.09.2004	North, Central, Drainage	53	Two balloons tied up, additional ground control points for mapping of the drainage

On September 25th, after getting the balloon back to the ground it was realized that the memory card of the camera quit working in flight and no pictures were obtained. After changing the memory card, the camera was operated with two small memory cards alternately. Every evening the resulting aerials from an area were checked for completeness.

September 27th was the last day in the field and the last opportunity to take photographs of those areas not covered. After having been inflated for more than five days, the lifting capacities of both balloons diminished dramatically. To lift the camera to 100 m, both balloons were tied together for additional lift. The unexpected strong uplift and the absence of wind made it possible, to tether the balloon along the drainage. Because there were no ground control points along the drainage, additional ones had to be set spontaneously. The coordinates were determined by a Garmin12 standard hand GPS.

3.2.4.1 Encountered Problems

After six days of taking aerial pictures, several problems were encountered. While filling the balloon with helium, there is the risk of burning a hole in the balloon's membrane, due

to fast outpouring gas. Because of loss of helium due to diffusion through the latex membrane, the balloon could only be used for five days. The balloon is very sensitive toward wind and turbulences. Turbulences occur most likely above geothermal features when hot air masses rise and mix with cold air masses. Wind made the balloon bounce around with the risk of contact of the frame and the vulnerable latex membrane. In the vicinity of trees and especially along the drainage there was the risk of getting entangled. Pictures taken on six different days under different light conditions and during different daytimes showed strong variances in contrast, brightness and shade effects. Wind was negligible in the mornings but the air was rich in steam and mist and the shadows were long. At noon the light conditions were good with no steam or mist was in the air, however the wind velocities increased.

3.3 Ground Survey

In addition to the aerial survey, a ground survey was done in September 2004. Major hydrothermal structures were mapped with the help of a special, self-designed parameter catalogue. It included the following parameters:

- Sample code, feature's name, date, time, weather
- GPS coordinates (Garmin 12) of the sample spot , sketch, photo documentation
- Feature's characteristic (hot spring, mud pot, wetland, drainage, fumarole, etc.)
- Runoff shape, direction and discharge
- Water color, turbidity, degassing activity
- Hydrochemistry with on-site parameters (pH, specific conductance, temperature, redox potential, Fe(II), Fe_{tot}, S²⁻)
- Remarks and special observations

A similar catalogue for the classification of hydrothermal features in Yellowstone was used by Becker (2004).

3.3.1 Feature's Name and Sample Code

The United States Board on Geographic Names limits the number and kind of names approved for National area in an effort to maintain their natural and wilderness character. In general, no new names will be adopted for features in a National Park or Wilderness Area unless a need is identified for purpose of safety, education, or area administration (Haines 1996).

The names given to the hydrothermal features during the mapping campaign primarily serve for easier identification and are not officially recognized by the Park Service. Most of the names chosen are descriptive, derived from color (e.g. White Eye), form (e.g. Puddle), and activity (e.g. Boiler) (Table 3). The sample code is a continuous nomenclature starting with the first letters of the study area WNCTAxx (West Nymph Creek Thermal Area), followed by the number of the sample spot.

Table 3: Site code and site name of features in the WNCTA.

Site Code	Arbitrary Site Name	Feature Type
WNCTA01	"Spouter"	Hot Spring (surging)
WNCTA02	"Brasil"	Hot Spring (surging)
WNCTA03	"Military pool"	Hot Spring (dormant)
WNCTA04	"Anoxia"	Hot Spring (dormant)
WNCTA05	"Channel 5"	Discharge (with gas activity)
WNCTA06	"Cinderella"	Hot Spring (Cinder)
WNCTA07	"Moonrise"	Hot Spring (dormant)
WNCTA08	"Puddle"	Hot Spring (surging)
WNCTA09	"Fizz"	Hot Spring (surging)
WNCTA10	"Chartreuse"	Hot Spring (dormant)
WNCTA11	"Popo"	Hot Spring (surging)
WNCTA12	"White Eye"	Hot Spring (surging)
WNCTA13	"Dillian Spring"	Hot Spring (surging)
WNCTA14	"Rotondo"	Hot Spring (surging)
WNCTA15	"Boiler"	Hot Spring (surging)
WNCTA16	"Fountain of Youth"	Hot Spring (dormant)
WNCTA17	"Little Prismatic"	Hot Spring (dormant)
WNCTA18	"The Swamp"	Hot Spring (dormant)

3.3.2 Runoff and Discharge

Six hydrothermal features had a more or less constant discharge. For the determination of small discharges ≤ 1 L/s, a graduated plastic cup was held in the discharge and the time to fill it was measured. For discharges ≥ 1 L/s the profile of the drainage was measured and a floating object (fir-cone) was used as tracer. An average flow velocity was determined out of five measurements. The discharge of the drainage of the West Nymph Creek Thermal Area during the month of September 2004 was about 17 L/s (0.017 m³/s).

3.4 Geographical Information System (GIS)

Geospatial information, maps, drawings, photos play a growing part in our everyday life. To provide the National Park Service with a powerful tool for further observation of the geothermal features in the West Nymph Creek Thermal Area, modern mapping devices had to be used. Different environmental, geological, and spatial data, in combination with their continuous update and fast distribution, require an organized management and permanent processing. Depending on the objectives, different subjects in one map are of primary interest. Therefore, the digital map created by a geographical information system (GIS) is replacing the conventional paper map more and more.

A geographical information system (GIS) is a computer system capable of capturing, storing, analyzing, and displaying geographically referenced information. This means that a GIS links geographic information (coordinates, location) to descriptive information (attributes) and produces geobjects. Practitioners also define a GIS as including the procedures, operating personnel, and spatial data that go into the system. Geobjects consist of their individual georeferenced geometry and the corresponding attribute information.

Most of the information about the world contains a location reference, placing that information at some point on the globe. Georeferencing is done by using a location reference system (e.g. longitude and latitude), and perhaps elevation. Coordinates from Global Positioning System (GPS) receivers can be uploaded into a GIS and be allocated to reference points.

Before the digital data can be processed and analyzed with a GIS, they may have to undergo manipulations (e.g. projection conversions). A projection is a mathematical means of transferring information from the Earth's three-dimensional, curved surface to a two-dimensional medium - paper or a computer screen. Different projections exist, each is particularly appropriate for certain uses.

Compared to a conventional map, a GIS can present many layers of different information. Each layer represents a particular theme or feature of the map. Themes can be made up of all the roads, all the lakes and rivers, or the geology of an area. These themes can be laid on top of one another, creating a stack of information about the same geographic area. Each layer can be turned on and off depending on the required information. The data structures (layers) can be of two types: vector or raster data.

3.4.1 Data Model - Raster or Vector?

How can a land use map be related to a satellite image? Digital data are collected and stored in different ways, whereas the two data sources may not be entirely compatible. Therefore, a GIS must be able to convert data from one structure to another.

The GIS can display satellite image data in raster format. Raster data files consist of rows of uniform cells coded according to data values. An example is land cover classification (Figure 14 left). Advantages of raster files are that they can be manipulated quickly and uncomplicated by image processing programs and GIS operations. Disadvantages of raster files are the obvious loss of information about position, size, and form of geobjects due to limitation of the resolution and the resulting pixel size. Raster files require high processing time and much hard disc space. They are often less detailed and may be less visually appealing than vector data files, which can approximate the appearance of traditional maps.

Vector digital data have been captured as points, lines (a series of point coordinates), or areas (polygons) (Figure 14 right). Thus, their position is given within a coordinate system. The topology of geo-features is the mutual relation between various spatial elements. An example of data typically held in a topology vector file would be the property boundaries and neighborhood relationship for a particular housing subdivision.

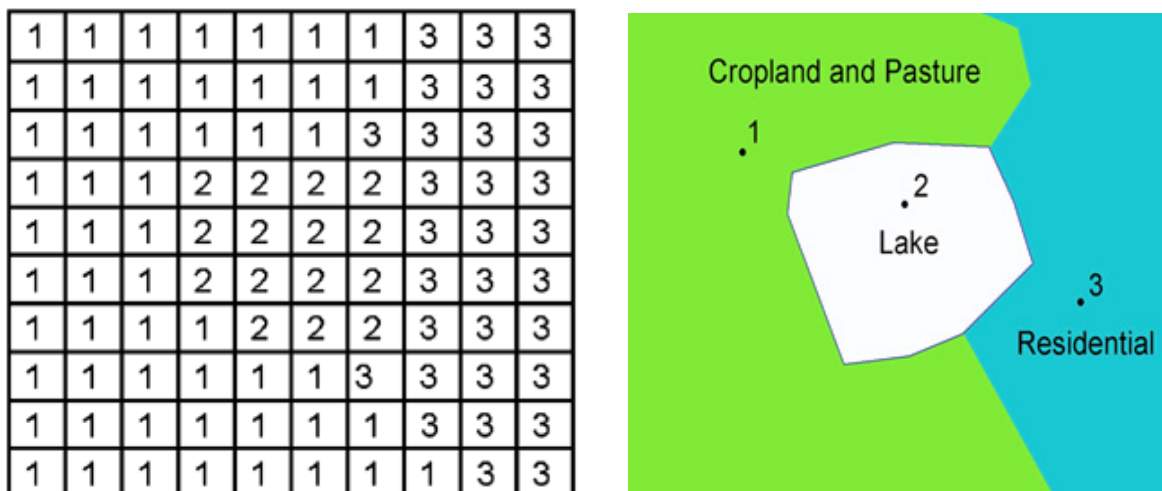


Figure 14: Example of the structure of both a raster file (left) and a vector file (right) (USGS online 2005)

Additional information on geobjects (attribute information) can be stored in attribute tables or whole databases, linked or integrated to the GIS. All the different powerful tools of a GIS permit data acquisition, storage, processing, management, manipulation, update, analysis and data output of georeferenced objects and spatial information.

3.4.2 TNTmips - Creating the Aerial Overview

In this work the GIS software TNTmips version 6.8 (Copyright © 1988-2005 MicroImages, Inc.; www.microimages.com) was used. “Mips” stands for map and image processing system. The difficulties in creating a mosaicked overview resulted from the unknown distortions of the remotely sensed images, the missing information on lens and camera, thus no calibration was possible. Furthermore, the shots were not perpendicular and the altitude was varying. All objects in a particular image were viewed from a single vantage point and that viewpoint varied from image to image. The perspective view of a single image can cause the apparent positions of ground features to be displaced from their correct horizontal positions. Relief displacements and tilt displacement are the main causes of spatial distortion, which contributes to errors in georeferencing component images. An object pictured in adjacent photos may be displaced from its true position by different amounts and in different directions in each image. When the photos are mosaicked, the two images of the same ground object are not placed at the same location in the mosaic. These effects are most obvious in low-altitude images.

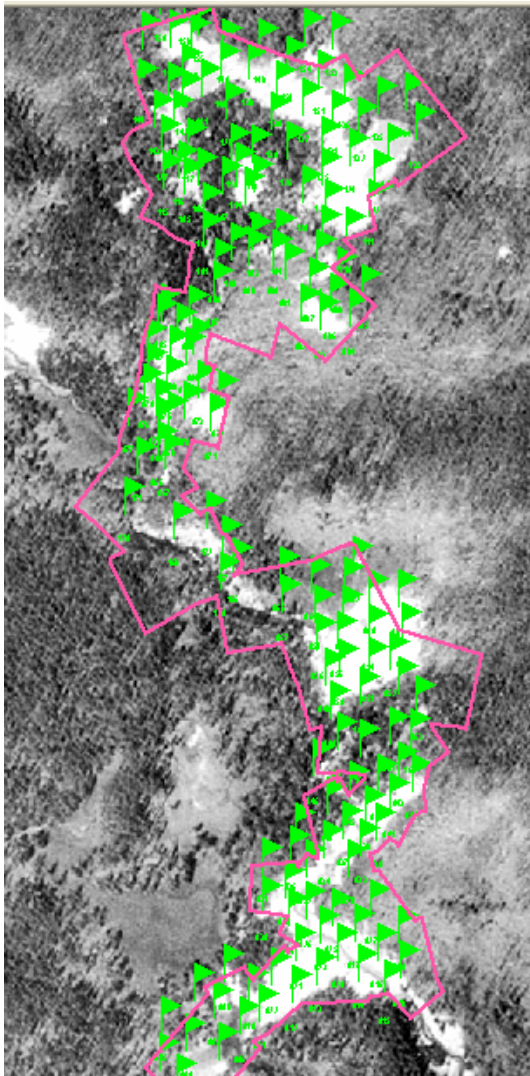


Figure 15: Distribution of the 171 ground control points

3.4.2.1 Georeferencing

The first step to create the digital atlas was to check the aerial photos taken with the balloon for their suitability. About 100 aerials among the 315 photos taken, showed at least three ground control points, low distortions at the borders and had a sufficient resolution. These 100 photos (jpg-files) were pre-processed (brightness, whiteness and contrasts) with the software ACDSee for Pentax version 5.1.0 (Copyright © 2003 ACD Systems, Ltd.) and were imported as raster objects into the program TNTmips. Most pictures showed four to six ground control points. The coordinates were allocated to the 171 reference points during the georeference process. Figure 15 shows the distribution of the ground control points over the investigation area. The following settings were used to define the map projection and coordinate system:

- System: Universal Transverse Mercator
- Projection: Transverse Mercator
- Zone: 12 (W 114 to W 108)
- Date: North American 1983
- Model: Piecewise Affine

A special change in the default georeferencing settings was done for the geometric transformation model, which was set to “Piecewise Affine”. The process analyzes the coordinates of the assigned ground control points and compares it to the locations predicted by the selected geometric transformation models. The results are used to determine numerical coefficients for coordinate transformation equations that convert the original distorted image to the desired geographic coordinate system. The Piecewise Affine model assumes that each control point is in the correct position, and the points are used to segment the image into a network of triangles. The Delaunay triangulation procedure is used to compute the optimum triangular network; benefit: all GCPs are positioned in the exact georeferenced location.

3.4.2.2 Mosaicking

The combination of the 50 georeferenced raster images into a single mosaic image was done with the Mosaic process in “TNTmips”. A number of options allow to fine-tune the appearance of the mosaic. Because all the input images were already georeferenced in the same map projection, the Automatic positioning option was chosen. The pre-set Piecewise Affine option from the georeferencing process made the aerial photographs fit together. However, not more than three of the best fitting adjacent and overlapping images were processed at the same time. Doing so, a constant control of the mosaic was possible, as well as reducing processing time. In some pictures with few ground control points in the center of the image, the distortion at the borders was reduced by adding additional tie points to the images. Tie points identify the corresponding locations in a pair of overlapping images and help to increase the adaptation between the images. For pictures where e.g., the shadows of the objects in the overlapping part were orientated in different directions or the offset at the borders was too big, a custom Processing Area was applied manually to the pictures. With this tool, parts of the input image could be excluded from the mosaic.

The Mosaic process requires many settings in different menu-panels; their corresponding functions are listed in Table 4.

Table 4: Different menu-panels and their functions for the Mosaic process

Menu-panel	Function
Input	Order of the imported images and geographic settings (projection, cell size, processing area)
Output	Geographic extents and projection of the mosaicked file
Parameters	Settings for the mosaicking process and display options
Contrast	Contrast enhancement options. Default values were preserved
Trend	Edit brightness effects. Default values were preserved

The settings in the menus “Contrast” and “Trend” were not changed because the adaptations of the pictures were done before importing them. In the “Output” menu, the projection for the mosaic is identical to the projection of the input file. Only the “Null Value” is set from none to 255 (white). Raster cells, which have the value 255, will appear transparent. White (255) was chosen instead of the default black (0) because of its low frequency of occurrence compared to black. In this menu, it was impossible to determine any color as transparent. Major changes in the settings were done in the menu “Parameters”.

Setting the Parameters

The Positioning of the pictures was done automatically. All the control points were accurately located, sufficient in number for the transformation model, and distributed uniformly across the image. In the following, the used parameter settings are marked with a dot. The Mosaicking process incorporates all the geometric transformation models (also called “Warping models”) that are available in the Georeferencing process. The Warping model is a process, which changes or rectifies the geometry of a raster image using the locations of ground control points that provide georeference control for the image.

- Warping Model: Piecewise Affine (refer to 3.4.2.1 Georeferencing)

The Resample process uses several steps to create the transformed output raster. First, the geometric transformation procedure creates a “blank” rectified raster with the proper extents and scale (cell size). Then a cell value is determined for each cell in the rectified raster. To do so, the geometric transformation is reversed for each output cell in order to determine its position in terms of the original raster line and column coordinates. The target output cell may be larger, smaller, or it may even overlap several input cells. The output cell value must therefore be calculated (interpolated) from some combination of the surrounding input cells. The Resample menu offers three options for interpolating output cell values: Nearest Neighbor, Bilinear Interpolation, and Cubic Convolution.

- Resampling Method: Cubic Convolution

Cubic Convolution calculates an output cell value from a 4x4 block of surrounding input cells. The output value is a distance-weighted average, but the weight values vary as a non-linear function of distance. This method produces sharper, less blurry images than bilinear interpolation, but it is the most computationally intensive resampling method.

The Overlap Method option menu on the Parameters panel allows choosing different techniques to process the overlapping portions of input rasters. Most methods attempt to create a gradual transition by assigning overlap cell values based on a comparison or mathematical combination of corresponding cell values from the input images. Only the Last Raster method uses the uppermost raster in each overlap area for the output image.

- Overlap Method: Last Raster

After the Mosaic process was completed, the aerial overview was checked for remaining distortions. This was done by activating the vector layer of the ground control points above the mosaic and comparing their positions. The use of non-georeferenced tie points between some images led to minor deviations (~ 0.3 m) between the actual position (gcp) and the displayed position (mosaic).

3.4.2.3 Raster Resampling

The mosaic of 50 aerial photographs was georeferenced and rectified a second time with a total of 171 ground control points because the original coordinates were slightly changed by the manual positioning of tie points. The Automatic Resampling process uses georeference control point information to perform simple rectification of distorted images, and to transform a raster image into a desired geographic coordinate system. The Resampling process compares known coordinates from ground control points to the locations predicted by the selected geometric transformation model. The results were used to determine numerical coefficients for coordinate transformation equations. For the Automatic Resampling process, a large number of exactly located and uniformly distributed ground control points is required (see Figure 15). Alike the mosaic process, the Automatic Resampling process as well requires adjustments in different menu-panels. Their names and the corresponding functions are described in Table 5.

Table 5: Different menu-panels and their functions for the Raster Resampling process

Menu-panel	Function
Model	Choice of different geometric transformation models
Resample	Methods for interpolating cell values for the output raster
Scale	Settings of the used method to scale the output raster
Orient	Options for orienting the output raster relative to the output
Extents	Settings for the geographic extents of the output raster

Settings for the Raster Resampling

The following settings were taken:

- Model: Piecewise Affine (refer to 3.4.2.1)
- Resample: Cubic Convolution (refer to 3.4.2.2)
- Scale: By Cell Size

This parameter allows specifying the size of the output cells (meter) by making entries in the text fields on size (meters). After the first resampling process with the default settings (no change of scale), the resulting mosaic from the West Nymph Creek Thermal Area had a raster cell size of 0.019 m and a file size of 4.3 Giga Bytes. This file size made any development (layers of the digital atlas) designed for further sharing on DVD impossible. The cell size was set to 0.025 m and the raster was resampled - the resulting mosaic had an acceptable file size of 1.8 GB. A difference between the 0.019 m and the 0.025 m cell size is hardly noticeable; even small geothermal features are still identifiable.

- Orient: To Projection

This setting orients the output raster to the map projection specified by the Georeferencing process (refer to 3.4.2.1)

- Extents: Entire Input

Specifies the extents of the output raster; here corresponding to the whole extents of the input raster.

3.4.2.4 Digitizing the Geoobjects

After the overview raster has been computed, the relevant geoobjects (hot springs, mud pots, drainages, wet zones, and fumarole areas) were digitized in the next step using the on-screen technique. The different thematic vector layers were created in the Spatial Data Editor in TNTmips. For all the new vector objects, the implied georeference from the computed mosaic was chosen. For the mapped features, the Topology Level was set to “polygonal” in a 2D coordinate system. To smooth the borderlines of the digitized objects, the TNTmips filter “Line Densification” with the “Cubic BSpline-Type” was applied to all the polygonal vector objects.

Various data tables were imported to the vector layer of the sample spots from a Microsoft Access database. To link the Access database immediately to TNTmips was impossible in the version 6.8. All the created layers, as well as additional maps and aerial photographs are explained in detail in the section of the Digital Atlas.

3.4.2.5 TNTAtlas - Displaying Geodata

The software package TNTAtlas provides the opportunity to publish and manage spatial information for wide-scale, multi-platform distribution. Complex stacks of relational imagery, maps, drawings, and databases can be merged together. Two different types of atlases exist: the hierarchical atlas and the single layout atlas. The hierarchical atlas has a logical arrangement with branching paths like an inverted tree. In this study, an atlas from the second type was created. The single layout atlas uses the TNTmips' map scale controlled visibility feature, which turns layers on and off as one zooms in and out depending on the current map scale of the displayed layout. A digital atlas is the electronic publication tool for today's geospatial information.

Several thematic groups were defined as "New Display Layout" by adding the respective layers and saving it as layout. One characteristic of the digital atlas is the "Hyperlink" function for photos, maps, and texts. With this tool, the photos were linked to their layer as external files and the text files were linked to their titles in the start page. By the "Hyper Index Navigator", it is possible to activate the different levels, switch between the layouts, and return to the home level (refer to 5.1).

4 Chemistry

The toxic and carcinogenic properties of some inorganic and organic trace elements species make their determination in natural waters vitally important. Several methods for speciation of arsenic and other elements in thermal waters using field and laboratory techniques are presented. A crucial requirement for chemical speciation is to maintain the integrity of the original chemical species in the sample before analysis.

4.1 Arsenic in the Environment

Arsenic is a naturally occurring metalloid that ranks 20th in abundance in the earth's crust. It forms more than 245 minerals; arsenopyrite is the most common (Mandal and Suzuki 2002). It is associated with igneous and sedimentary rocks, where average concentrations range from 0.5 to 2.5 mg/kg (Smedley and Kinniburgh 2002). Sulfidic ores, along with copper, nickel, lead, cobalt, or other metals show high concentrations in arsenic. Weathering of rocks converts arsenic sulfides to arsenic trioxides, which enter the arsenic cycle as dust or by dissolution in rain, rivers, or groundwater. Furthermore biological activity, volcanic activity, and anthropogenic inputs like smelting operations and fossil fuel combustion are responsible for the emission of As into the atmosphere, from where it is redistributed on the earth's surface by rain and dry fallout. Other man-made sources for the As-contamination of soils and ground waters are mining activities and processing wastes, electronic industries, tanning industries, ammunition factories, poultry and swine feed activities, pesticides and wood preservatives, cosmetic and pharmaceutical industry, and high soluble arsenic trioxides stockpiles (Nordstrom 2002).

Arsenic can be easily solubilized in ground waters depending on pH, redox conditions, temperature, and solution composition. Natural arsenic in ground water at concentrations above the drinking water standard of 10 µg/L (EPA and WHO) is not unusual. A small number of source materials are now recognized as significant contributors to arsenic in water supplies: organic-rich or black shales, Holocene alluvial sediments with slow flushing rates, mineralized and mined areas (most often gold deposits), volcanogenic sources, and thermal springs. High concentrations of arsenic are common in geothermal waters in Kamchatka, New Zealand, Japan, Alaska, California, and Wyoming, where high geologic As background concentrations are found (e.g. black shales, rhyolite). In geothermal waters in Hawaii and Iceland, where young basalts make up most of the rocks, arsenic concentrations are rather low (Nordstrom 2002). The high As concentrations in Yellowstone are believed to originate from rock-leaching processes rather than direct magmatic origin. Silicic volcanic rocks and especially volcanic glasses have elevated As

concentrations. A thick layer of ash-flow tuff overlies the important thermal regions of the Park (Stauffer 1984).

4.1.1 Arsenic Toxicity

Humans are exposed to many different forms of inorganic and organic arsenic species (arsenicals) in food, water, and other environmental media. Arsenic is still the most common source of acute metal and metalloid poisoning and is second only to lead in chronic ingestion. The chemical forms and oxidation states of arsenic are important, as toxicity depends on factors like physical state, gaseous, dissolved or particulate, the rate of absorption into cells, the rate of elimination and chemical substitution. Each of the forms of arsenic has different physicochemical properties and bioavailability, therefore the study of the kinetics and metabolism of arsenicals in individuals is important. Arsenic intake may take place via respiration of dust and fumes or orally by the uptake of arsenic in water, beverages, soil and food. The toxicity of arsenicals is reported to decrease in the following order: arsines (gaseous form of arsenic) > inorganic As(III) > organic As(III) e.g. MMA(III) and DMA(III) > organic As(V) e.g. DMA(V) and MMA(V) > inorganic As(V) and arsenosugars. Symptoms of acute arsenic poisoning are restlessness, throat discomfort, nausea, chest pain, convulsion, diarrhea, vomiting, collapse, and cardiac failure, sometimes followed by coma or death. Symptoms of chronic As poisoning include bronchitis, myocardial infarction, arterial thickening, hyperpigmentation, hyperkeratosis, peripheral neuropathy, skin, lung, bladder, liver cancer, mutagenic and teratogenic effects, and the widespread “black foot” disease (necrosis on soles and palms). A detailed review on As toxicology is given by Mandal and Suzuki (2002).

4.1.2 Arsenic in Natural Waters

The range of arsenic concentrations found in natural waters is large, ranging from less than 0.5 µg/L to more than 5000 µg/L. Typical concentrations in freshwater are less than 10 µg/L and mostly less than 1 µg/L. Rarely, much higher concentrations are found in ground water. Nevertheless, natural arsenic in ground water at concentrations above the drinking water standard of 10 µg/L (EPA and WHO) is not unusual. Well-known high As ground water areas have been found in Mexico, Argentina, Chile, China and Hungary, and more recently in West Bengal (India), Bangladesh and Vietnam. In the Bengal Basin, more than 40 million people are exposed to drinking water containing “excessive” (> 50 µg/L) As. These large-scale “natural” As ground water problem areas tend to be found in two types of aquifers: firstly, inland or closed basins in arid or semi-arid areas (especially in volcanogenic provinces), and secondly, strongly reducing aquifers often composed of alluvial sediments. Both environments tend to contain geologically young sediments in flat, low-lying areas where ground water flow is sluggish. Historically, these are poorly flushed aquifers and any As released from the sediments has been able to accumulate in the ground water. Arsenic-rich ground waters are also found in geothermal areas and, on a more

localized scale, in areas of mining activity and where oxidation of sulfide minerals (e.g. pyrite) has occurred. The As concentration of these affected aquifers does not appear to be exceptionally high, being normally in the range 1–20 mg/kg (Smedly and Kinniburgh 2002).

Three distinct “triggers” have been determined that can lead to the release of As on a large scale. The first is the development of high pH (> 8.5) conditions in semi-arid or arid environments usually as a result of the combined effects of mineral weathering and high evaporation rates. This pH change leads either to the desorption of adsorbed As (especially As(V) species) and a range of other trace elements from mineral oxides (especially Fe oxides), or it prevents them from being adsorbed. The second trigger is the development of strongly reducing conditions at near-neutral pH values, leading to the desorption of As from mineral oxides and to the reductive dissolution of Fe and Mn oxides, also leading to As release. Iron(II) and As(III) are relatively abundant in these ground waters and sulfate concentrations are low (1 mg/L or less). The third trigger for As release is high dissolved O₂ concentration, which initiates pyrite oxidation. As arsenic concentrations are elevated in pyrites (e.g. arsenopyrite), mainly reduced As is released and oxidized to As(V) in the ground water. High concentrations of phosphate, bicarbonate, silicate and possibly organic matter can decrease or prevent the adsorption of arsenate and arsenite ions onto fine-grained clays because of competition for adsorption sites. Arsenite tends to adsorb less strongly than arsenate often causing arsenite to be present at higher concentrations. Unfortunately, these generalities do not allow prediction of high or low dissolved arsenic concentrations in any particular well. This is due to the large degree of spatial variability in dissolved arsenic concentrations within arsenic-affected aquifers. Arsenic-affected aquifers are restricted to certain environments and appear to be the exception rather than the rule (Smedly and Kinniburgh 2002).

4.1.3 Arsenic Species Chemistry

The most common valence states of arsenic are 3 and 5, as in AsF₃ and AsF₅. Coordination numbers for arsenic cover the range 3 (AsF₃), 4 (As(CH₃)₄⁺), 5 (AsF₅), and 6 (AsF₆⁻). The oxidation number of arsenic in arsenic compounds, as for any element, depends on a model of the charge distribution in the bonds. The use of the relative electronegativities of the respective atoms is the usual way for the determination of the charge distribution. Arsenic has an electronegativity of 2.18 in the Pauling scale of electronegativities (Mortimer 1996). In aqueous solution, arsenic does not form complexes with simple anions like Cl⁻ and SO₄²⁻ as do cationic metals. Arsenic forms anions and reacts with C, O, S, halogens or H. Chemical bonds like As-X are polarized As^{δ+}—X^{δ-} when X = C, O, S or a halogen. The situation regarding As-H is less clear because both elements have a similar electronegativity. Cullen and Reimer (1989) assume that arsenic is the more electropositive element (oxidation state +3). Figure 16 shows the predominant speciation of arsenic under standard conditions of 25°C, 1 atm, at varying pH and redox conditions.

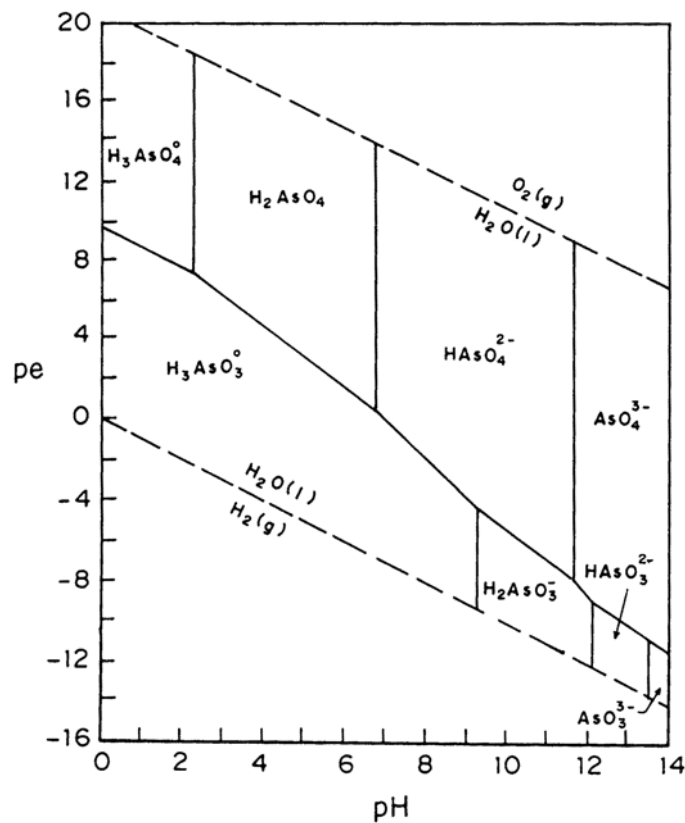


Figure 16: Pe–pH diagram of arsenic predominance in water at 25°C (Kumaresan and Riyazuddin 2001)

In aqueous systems, arsenic exhibits anionic behaviour. In aerobic waters, arsenic acid predominates only at extremely low pH (< 2); within a pH range of 2 to 11, it dissociates to $H_2AsO_4^-$ and $HAsO_4^{2-}$. Arsenious acid appears at low pH and under mildly reduced conditions. It only dissociates to $H_2AsO_3^-$ at a pH > 9. Only when the pH exceeds 12 does $HAsO_3^{2-}$ appear. At low pH in the presence of sulphide, $HAsS_2$ can form; arsine, arsine derivatives and arsenic metal can occur under extreme reducing conditions (Kumaresan and Riyazuddin 2001).

4.1.3.1 Dissolved Inorganic As(V)

The oxidized form of dissolved As is the pentavalent arsenate, As(V). Redox potential (E_H) and pH are the most important factors controlling As speciation. The pH-dependent dissociation of As(V) species is shown in Figure 17. In waters with a pH about 7, the negatively charged species $H_2AsO_4^-$ and $HAsO_4^{2-}$ predominate. In acid solutions with a pH < 2 (e.g. mine drainages, hydrothermal waters) significant amounts of the zero-valent species $H_3AsO_4^0$ occur, with solution properties comparable to those of phosphoric acid. Alkaline waters with a pH > 12 show high concentrations of AsO_4^{3-} .

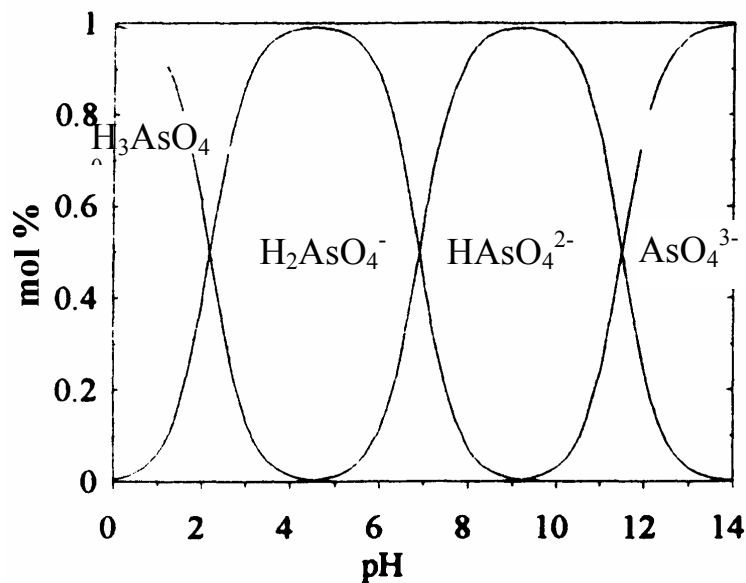


Figure 17: Arsenate speciation as a function of pH (after Rude 1996)

Sohrin et al. (1997) and others state that there is a significant negative correlation between arsenic concentration in surface waters and biological activity. Arsenic uptake by phytoplankton during spring bloom leads to a depletion in dissolved arsenate was measured. During winter, in the absence of biological activity, an increase in dissolved arsenate is registered. Different limiting factors for As(V) concentrations in the aqueous phase are known, such as precipitation as, or coprecipitation with, an oxide, hydroxide, carbonate or phosphate mineral, or more likely by their strong adsorption to hydrous metal oxides (e.g. Fe-, Mn-, and Al-oxides), clay or organic matter. Limiting mineral phases are alkaline earth metal-arsenate complexes, or rather their hydrates. Most toxic trace-metal cations (e.g. Pb^{2+} , Cu^{2+} , Ni^{2+} , Cd^{2+} , Co^{2+} , Zn^{2+}) generally become increasingly insoluble as the pH increases. In contrast, most oxyanions including arsenate tend to become less strongly sorbed, or even desorb as the pH increases ($\text{pH} > 8.5$). This information was stated earlier (Reducing aquifer conditions at near-neutral pH values lead to the desorption of As from mineral oxides and to the reductive dissolution of Fe- and Mn-oxides, also leading to As release). Large concentrations of phosphate, bicarbonate, silicate and possibly organic matter can enhance the desorption of As because of competition for the same binding sites (Smedley and Kinniburgh 2002).

4.1.3.2 Dissolved Inorganic As(III)

Concentrations and relative proportions of As(V) and As(III) vary according to changes in input sources, redox conditions and biological activity. Reduction of As(V) to As(III) and vice versa oxidation of As(III) to As(V) can occur both enzymatically catalyzed or in a purely chemical reaction.

Stratified lakes show strong varying redox gradients, which leads to stratification of As concentration. Observations by Sohrin et al. (1997) at Lake Biwa in Japan showed that As

speciation changed seasonally in the photic zone. The As(III) concentrations in the epilimnion increased in spring and fall in all probability due to the productivity of phytoplankton. In the hypolimnion, As(III) may have been released from the sediments or formed by reduction of As(V) in the water column. Biological productivity in the bottom lake waters during the summer months deplete oxygen concentrations and are a likely cause of the higher As(III) concentrations in the hypolimnion (Sohrin et al. 1997). The presence of As(III) may be maintained in oxic waters by biological reduction of As(V), particularly during summer months. Higher relative proportions of As(III) have been detected in river stretches close to inputs of As(III)-dominated industrial effluent and in waters with a component of geothermal water (Andreae and Andreae 1989). Many bacteria and cyanobacteria strains are known which catalyze the reduction of As(V) to As(III), e.g. *Pseudomonas fluorescens* (Myers et al. 1973), *Anabaena oscillaroides* (Freeman 1985), and the freshwater phytoplankton *Chlorella* (Blasco et al. 1972). The reverse process of spontaneous As(III) oxidation to As(V) was first observed in cattle dipping fluids by Brünnich in 1909. Turner (1949) characterized new species of arsenite-oxidizing bacteria from the genus of *Pseudomonas*, *Xanthomonas*, and *Archomobacter*. The rapid oxidation of arsenite to arsenate by *Thermus aquaticus* and *Thermus thermophilus*, common inhabitants of hot springs and thermally polluted domestic and industrial waters has been documented by Gihring et al. (2001). Field investigations at a hot spring site in Yellowstone revealed conserved total arsenic transport and rapid arsenite oxidation occurring in the drainage channel, heavily colonized by *Thermus aquaticus*. In laboratory experiments, arsenite oxidation by cultures of *Thermus aquaticus* Y71 (previously isolated from YNP) and *Thermus thermophilus* HB8 was accelerated by a factor of over 100 relative to abiotic controls. Purely chemical conversion rates are low, compared to the biologically catalyzed ones.

In ground waters, the ratio of As(III) to As(V) can vary greatly as a result of variations in the abundance of redox-active solids, especially organic C, the activity of microorganisms and the extent of convection and diffusion of O₂ from the atmosphere. In strongly reducing aquifers (Fe(III)- and SO₄-reducing aquifers, e.g. Bangladesh and inner Mongolia), As(III) typically dominates with ratios of As(V)/As(III) in the range of 0.1 to 0.9. In the presence of sulfides under reducing conditions the formation of arsenic sulfides may limit the aqueous As(III) fraction. In oxic seawater, the As is typically dominated by As(V), though some As(III) is invariably present and becomes of increasing importance in anoxic bottom waters. Ratios of As(V)/As(III) are typically in the range 10-100 in open seawater (Smedley and Kinniburgh 2002). At the near-neutral pH of many ground waters, As(III) is expected to be less strongly sorbed than As(V) and so some desorption of As may occur as a result of the start of strongly reducing conditions following sediment burial. Recent experiments with synthetic Fe- and Al-oxides have demonstrated the desorption of As following reduction of As(V) to As(III). Dissolution of the oxides was not necessary for As release (Zobrist et al. 2000).

Both oxidation of As(III) and reduction of As(V) may occur during storage and inadequate sampling techniques. Laboratory studies show that the kinetics of oxygenation of As(III) are slowest in the slightly acid range around pH 5, which is why water samples are often filtered and acidified to about this pH to preserve their in situ speciation. Acidification prevents complexation, filtration excludes from microbial activity. Photocatalyzed Fe(III) reduction causes As(III) oxidation; however, storing the sample in the dark prevents photochemical reactions. Furthermore, the presence of Fe(II) or SO_4 inhibits the oxidation of As(III) by Fe(III) because of complexation reactions and competing reactions with free radicals. Fast abiotic As(III) oxidation reactions as observed in the laboratory are not observed in natural water samples. Reasons are, that (1) the As redox species have already stabilized, (2) most natural waters contain very low dissolved Fe(III) concentrations, and (3) the As(III) oxidation caused by Fe(III) photoreduction is inhibited by Fe(II) or SO_4 (McCleskey et al. 2004).

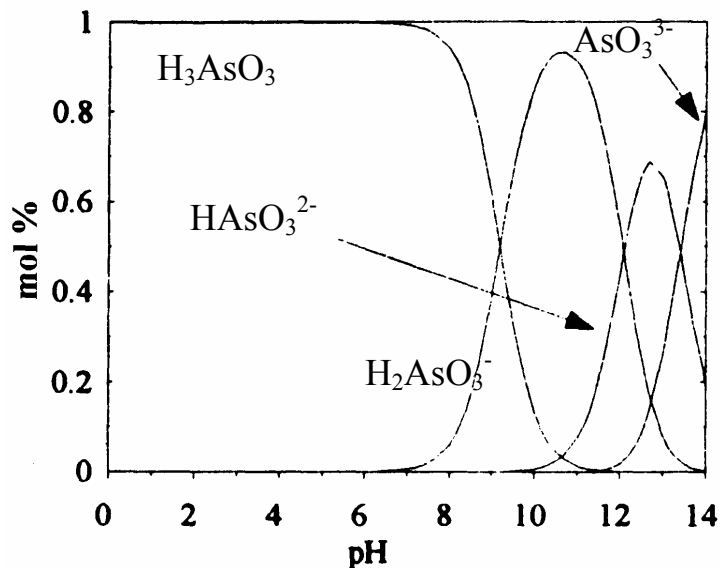


Figure 18: Arsenite speciation as a function of pH (after Rude 1996)

The pH dependent As(III) species distribution is shown in Figure 18. In aqueous solutions with a pH < 9, the zero-valent H_3AsO_3^0 species is dominant. Its solubility and mobility is 4 to 10 times higher than those of As(V) (Cullen and Reimer 1989). While the solution properties of the pentavalent H_3AsO_4^0 resemble those of H_3PO_4^0 (phosphoric acid), the properties of trivalent H_3AsO_3^0 rather resemble those of H_3BO_3 (boric acid). In aqueous solutions within a pH range of 9 to 12, H_2AsO_3^- is predominant. In alkaline solutions within a small pH range from 12 to 13, HAsO_3^{2-} is the predominant species. AsO_3^{3-} is present in solutions with pH > 13.

The toxicity of As(III) compared to As(V) is stated to be 18-50 times higher (Petrick et al. 2000), respectively 25-60 times higher (Morrison et al. 1989). Because arsenite is more toxic than most other forms of arsenic, oxidation of arsenite to arsenate is generally considered as protective mechanism used by many microorganisms.

4.1.3.3 Organic arsenic compounds

The transfer of alkyl, mostly methyl groups, can transform inorganic arsenic compounds to organic ones. The process is not a purely chemical one, but it is promoted by microbial activity (fungi, bacteria, yeasts, algae) and, presumably, requires the intervention of As within the metabolic pathways of the cells (Cullen and Reimer, 1989).

Challenger (1945) first proposed the principle of the methylation process using a sequence of alternating reduction and oxidizing steps. The oxidation steps include the replacement of OH⁻-groups by CH₃⁻-groups. Inorganic As(V) is first reduced either enzymatically or non-enzymatically to inorganic As(III), then transferred to monomethylarsonic acid (MMAA; CH₃As^VO(OH)₂). Challenger favored the hypothesis that the methylation of arsenic involved the transfer of a preexisting methyl group from compounds such as betaine, methionine, or a choline derivate (formaldehyde).

Recent studies revealed detailed information on the chemicals and enzymes involved and identified S-adenosylmethionine (SAM; a methionine derivate) as major methyl-donor. To proceed from arsenate to trimethylarsine, four two-electron reductions are required. SAM then methylates each reduction product. A complete and modern version of the individual reaction steps from arsenate to trimethylarsine is shown in Figure 19.

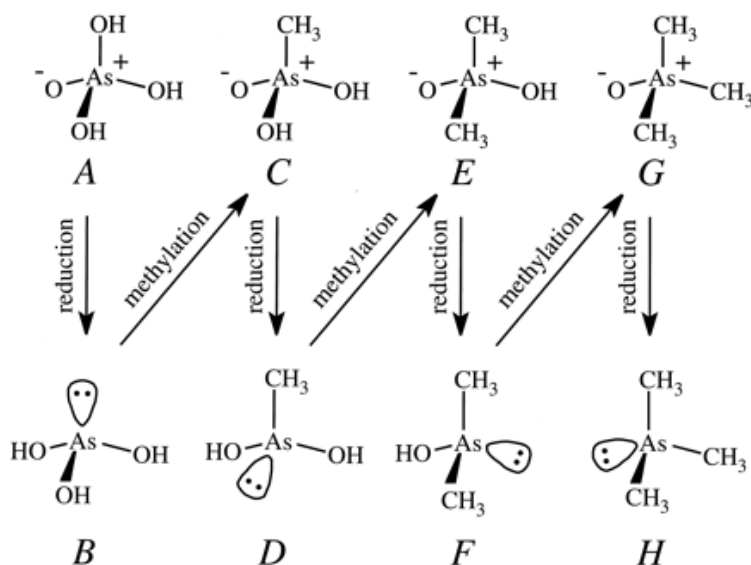


Figure 19: Challenger mechanism for the conversion of arsenate to trimethylarsine. (A) Arsenate; (B) arsenite; (C) methylarsonate; (D) methylarsonite; (E) dimethylarsonate; (F) dimethylarsinite; (G) trimethylarsine oxide; (H) trimethylarsine. The top line of structures shows the As(V) intermediates. The vertical arrows indicate the reduction reactions to the As(III) intermediates (bottom line), and the diagonal arrows indicate the methylation steps by S-adenosylmethionine (SAM) (Bentley and Chasteen 2002).

Two of the proposed intermediates are poorly defined As(III) compounds - (D) methylarsonous acid, CH₃As^{III}(OH)₂, and (F) dimethylarsinous acid, (CH₃)₂As^{III}OH. The reductive steps are straightforward in concept but not in practice. To convert arsenate to

trimethylarsine, the reductions are likely to be enzyme catalyzed with reductants providing the necessary 2e⁻. The reductants are almost certainly thiols, and particular attention has been given to glutathione (GSH) and lipoic acid (6,8-dithiooctanoic acid). There is little experimental evidence from microbial systems, but it is assumed that the reactions resemble those for formation of methylarsonate and dimethylarsinate in mammals. There is evidence that both in vitro and in vivo GSH does function as a reductant and reduces arsenate to arsenite. Further reaction eventually forms arsenotriglutathione. Again, the mechanism is complicated by the ability of arsenic compounds to react with thiols. Dithiol derivatives such as lipoic acid could be involved as a membrane-bound or enzyme-bound component. The final step of the Challenger mechanism, the reduction of trimethylarsine oxide to trimethylarsine, is possible with a variety of thiol reagents (cysteine, dimercaptopropanol, lipoic acid, mercaptoacetic acid, and mercaptoethanol).

The methylation steps may appear at first sight confusing, since in all cases an oxidation from As(III) to As(V) occurred. To keep the process in balance there must be a concomitant reduction. Since no redox cofactor is involved, the process appears at first glance to be a simple methyl transfer process. However, a detailed analysis of the reaction indicates that the necessary reduction is found in the corresponding decrease in oxidation number from -II to -IV for the transferred carbon. A formal method for assigning oxidation states to redox-labile elements in organic compounds helps in following the reduction and methylation steps with arsenic (Bentley and Chasteen 2002).

Since the methyl group of ¹⁴CH₃ methionine was transferred to arsenic in the formation of trimethylarsine by *S. brevicaulis*, the postulated role for SAM was substantiated (Challenger 1954). When C²H₃ methionine was used as a methyl donor, the ²H-labeled nonvolatile metabolites produced ²H-labeled arsines. These observations were consistent with the operation of the Challenger mechanism, with methyl groups being derived from methionine by way of SAM (Cullen et al. 1995). Moreover, trimethylarsine formation from (CH₃)₂AsO(OH) by these organisms was inhibited by ethionine. Ethionine is an antagonist for methionine; hence, these observations support the role of a methionine-based synthetic path (Cullen et al. 1977).

The ability of wood-rotting fungi to metabolize arsenic compounds is of considerable interest since arsenicals are commonly used as wood preservatives. Merrill and French (1964) examined 65 species of wood-rotting fungi for growth in the presence of As₂O₃. Only *L. trabea* and *Lenzites saepiaria* produced an unidentified, garlic-odored gas. Recent work from Pearce et al. (1998) confirmed the volatilization of arsenic by another wood decaying fungus. *Phaeolus schweinitzii* produced volatile methylated products of arsenic when grown in presence of As₂O₅, but again the product was not specifically identified.

It is not clear why phosphate strongly inhibits formation of trimethylarsine in cultures growing with arsenate, arsenite, and monomethylarsonate but has no effect when

dimethylarsinate was used. It might be of interest that phosphorus and arsenic are both members of group 15 of the periodic table (Cox and Alexander 1973).

Huysmans and Frankenberger (1991) isolated a *Penicillium* species from an agricultural evaporation pond in an area with high arsenic concentrations in the soil. The organism formed trimethylarsine from methylarsonate; addition of carbohydrate and sugar acids to the minimal medium suppressed volatilization, whereas glutamine, isoleucine, and phenylalanine had a stimulatory effect. Various elements known to be toxic to living systems generally inhibited the conversion of methylarsonate to trimethylarsine by this *Penicillium* species. The element showing the most significant inhibition was V, followed by Ni, Sn, B, Te, Mn, Mo, Cr, and Ag; at low concentrations, the following elements were stimulatory: Hg, Fe, Cu, Al, Zn, and Se (Frankenberger 1998).

Challenger (1945) and Bach (1945) doubted that bacteria could methylate arsenicals. The metabolism of arsenic compounds widely used in agriculture has been studied in mixed microbial populations from soil. While evidence was obtained for arsenic volatilization, it was usually not clear whether bacteria or fungi were involved. The first report documenting bacteria producing arsine was presented by McBride and Wolfe (1971). Anaerobically growing bacteria (*Methanobacterium MoH*) might have produced the gas dimethylarsine, $(\text{CH}_3)_2\text{AsH}$. Several bacterial species (e.g. *Corynebacterium* sp., *Escherichia coli*, *Flavobacterium* sp., *Proteus* sp., and *Pseudomonas* sp.) were isolated from the environment, incubated with sodium arsenate and showed methylation capacities in producing dimethylarsine. Further studies focused on anaerobic ecosystems such as sewage sludge, waste water treatment plants, and landfill and identified anaerobic volatilization of arsenic. Michalke et al. (2000) identified *Methanobacterium formicicum* as the most efficient organism for As volatilization; arsine and all three methylarsines, as well as an unidentified volatile arsenic compound, were produced over the As concentration range of 0.05 to 0.3 mM.

Temperature plays a decisive role in the methylation process. Howard et al. (1982) observed no methylation occurring below 9-12°C. Organic As compounds, like all organometallics, are thermodynamically unstable. Due to their slow decomposition kinetics, they may have a transient existence under a variety of environmental conditions. Chemical demethylation is slow. However, reduction, oxidation, hydrolysis, and reaction with sulphur compounds can significantly alter distribution, mobility, and volatility of the biologically generated compounds. A detailed review on As methylation is given in Cullen and Reimer (1989), and Bentley and Chasteen (2002).

4.1.3.4 Dissolved Mono- and Di-methylated Arsenic Acids

The most common dissolved methylated arsenic species are dimethylarsinic acid ($\text{DMA}^{\text{V}}\text{A}$) and monomethylarsonic acid ($\text{MMA}^{\text{V}}\text{A}$). In both cases As is present in the pentavalent oxidation state. Less frequent are the trivalent $\text{DMA}^{\text{III}}\text{A}$ and $\text{MMA}^{\text{III}}\text{A}$. The rare occurrence

of tri-methylated arsenic acid ($\text{TMA}^{\text{V}}\text{O}$) might be due to facile reduction to the volatile $(\text{CH}_3)_3\text{As}$ by microorganisms.

Methylated pentavalent arsenic compounds ($\text{MMA}^{\text{V}}\text{A}$ and $\text{DMA}^{\text{V}}\text{A}$) are much easier excreted from most organisms compared to inorganic As, since they are less reactive with tissue constituents (Buchet et al. 1981).

The species distribution of both, $\text{MMA}^{\text{V}}\text{A}$ and $\text{DMA}^{\text{V}}\text{A}$, is strongly pH-dependent. For $\text{MMA}^{\text{V}}\text{A}$ (Figure 20), the negatively charged species $\text{CH}_3\text{AsO}_2(\text{OH})^-$ dominates under near neutral conditions (pH 4 to 9). The zero valent species $\text{CH}_3\text{As}(\text{OH})_2$ only predominates under acid conditions (pH < 3.6). In alkaline solutions (pH > 9), the double negatively charged species $\text{CH}_3\text{AsO}_3^{2-}$ dominates.

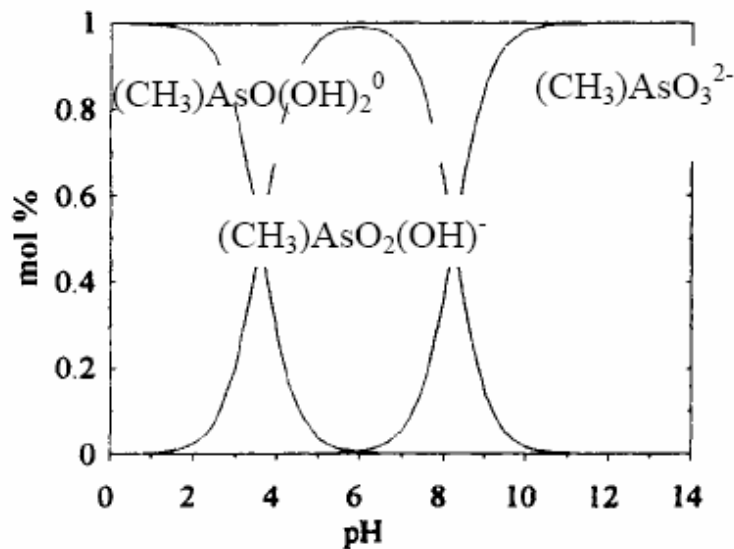


Figure 20: $\text{MMA}^{\text{V}}\text{A}$ species distribution is pH dependent (after Rude 1996).

Only two species are known for $\text{DMA}^{\text{V}}\text{A}$ (Doak and Freedman 1970). The predominant one is the zero valent $(\text{CH}_3)_2\text{AsO}(\text{OH})$ for pH < 6.1 (Figure 21).

The average share of methylated compounds (tri- and pentavalent MMAA and DMAA) in some fresh and seawater samples amounted up to 10-20% of the total As (Braman and Foreback 1973). Depending on bioactivity and temperature, the share can also become up to 70%. Sohrin et al. (1997) report an increased $\text{DMA}^{\text{V}}\text{A}$ fraction (up to 64% of total As) during summer in water samples from Lake Biwa, Japan. In contrast to the highly mobile inorganic zero valent As(III) species, some unspecific sorption on cation and anion exchangers is known for the $\text{DMA}^{\text{V}}\text{A}$ species.

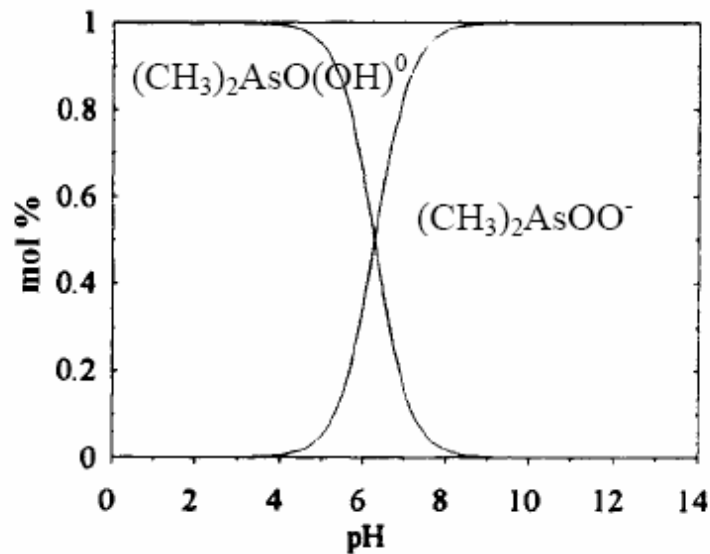


Figure 21: DMA^{VA} species distribution is pH dependent (after Rude 1996).

The existence of the trivalent organic acids MMA^{III}A and DMA^{III}A is proved by recent studies (e.g. Le et al. 2000, Sohrin et al. 1997). Inadequate sampling techniques, preparation, and storing temperature makes the trivalent methylated As fraction (MMA^{III}A and DMA^{III}A) oxidize within a few days, respectively within a few hours.

4.2 Species Separation

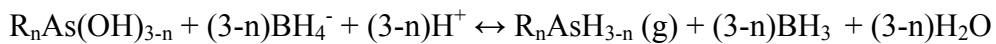
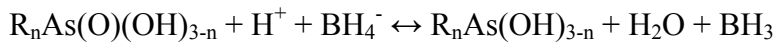
Speciation of arsenic is investigated because of its importance for toxicological studies and remediation efforts. The biophysicochemical properties of arsenic species in particular require quantitation of individual species in addition to total arsenic concentration. Standard inductively coupled plasma - atomic-emission spectrometry (ICP-AES) is an appropriated method for the determination of elevated total arsenic concentration, as it is unable to measure down to 10 µg/L. Existing methods using graphite furnace - atomic absorption spectrometry (GF-AAS), hydride generation atomic absorption spectrometry (HG-AAS), or inductively coupled plasma - mass spectrometry (ICP-MS) are sufficient to quantitate total arsenic well below the US Environmental Protection Agency (EPA) and the World Health Organization (WHO) Maximum Contaminant Level (MCL) of 10 µg/L.

Recent advances in instrumentation, such as high-performance liquid chromatography - inductively coupled plasma - mass spectrometry (HPLC-ICP-MS), have provided more straightforward methods for the determination of As species. Anion-exchange chromatography has been used successfully in speciation procedures because of the anionic nature of many arsenic species. Arsine generation techniques can be used for inorganic As species based on the different susceptibilities of the trivalent arsenite and pentavalent arsenate reduction to arsine. The hydride generation technique is unable to detect or resolve organic As species if no anion-exchange chromatograph is switched in, followed by ICP-

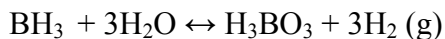
MS detection (Bednar et al. 2004). The individual advantages and disadvantages of the hydride generation technique and the liquid chromatography are presented and discussed in detail in 4.2.1 and 4.2.2. The on-site arsenic speciation technique (ion-exchange cartridges) is explained under 4.3.3.

4.2.1 Hydride Generation

Hydride generation (HG) occurs when dissolved species in an acidic solution react with NaBH_4 to form volatile species. The technique of hydride generation enables As(III)/total As species separation due to the different pH sensitivities of the species in solution (Figure 22). Dissolved pentavalent As species are first reduced to trivalent As species, before arsines are produced according to the following reaction:



In a first reduction step, generated Borane hydrolyses, giving the intermediate BH_3OH^- . In a second reduction step, boric acid and gaseous hydrogen are formed. The general reaction is:



The advantage of HG for analysis is the isolation of the analyte from the matrix and the pH dependent species separation. It thus eliminates interferences and enhances sensitivity 10 - 100 fold compared with direct liquid sample nebulization to (Howard 1997). Typical concentrations for the reductant NaBH_4 are 0.01 - 2%. Higher concentrations lead to the formation of excess hydrogen and increase backpressure in reaction vials. In acid solutions, the oxidation rates of NaBH_4 are $6 \cdot 10^5$ mol/L for the first reaction step, and $1 \cdot 10^7$ mol/L for the second. Much lower reaction rates are realized in alkaline solutions with $2.9 \cdot 10^{-4}$ mol/L, respectively $4.7 \cdot 10^{-2}$ mol/L (Gardiner and Collat 1965). Thus, for longer stability, NaBH_4 is prepared in NaOH , for rapid hydride generation acid, mainly HCl , is added.

Despite its many advantages, a number of problems are associated with the HG approach. Variations in the hydride-generation efficiency for different As species are caused by the strong pH-dependency of the arsine generation (Figure 22). Arsenic (III) predominates as H_3AsO_3^0 up to a pH of 9 and reacts with the reducing agent already at slightly acid conditions (pH 5 - 7). At a pH range between 0.5 - 2, $\text{DMA}^{\text{V}}\text{A}$ shows a clear peak. Arsine generation from $\text{MMA}^{\text{V}}\text{A}$ takes place at $\text{pH} < 4$ and arsine generation from As(V) must be carried out at $\text{pH} < 1$. The response for sample solutions with a $\text{pH} < 3$ and elevated methylated arsenic concentrations will be inaccurate because not only the As(III) fraction is detected, but the methylated species as well. The calculated As(V) concentration will be lower than its actual concentration, the As(III) concentrations will be overestimated.

An excess of HCl, used as carrier solution in the AAS or as sample preservative, leads to a decrease of sensitivity on all four As species, since the surplus H^+ rapidly consumes the reductant, which does no longer volatilize the As species (Luna et al. 2000).

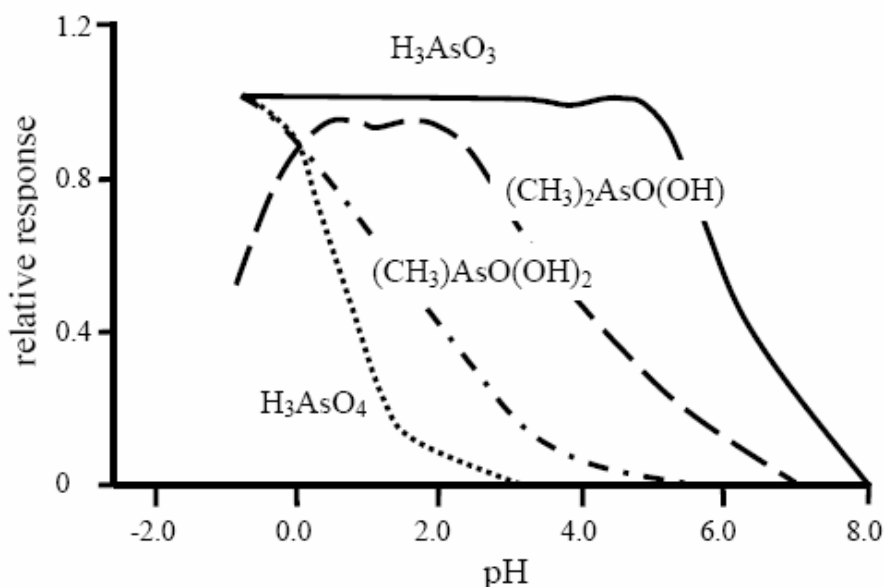


Figure 22: pH dependence of arsine hydride generation from solutions containing As(V), MMAA, DMAA, and As(III) (Howard 1997).

When using hydride generation, it is assumed that AsH_3 only forms from inorganic As, MMA only from monomethylated species, DMA only from dimethylated species, and TMA only from $TMA^V O$. The process of transmethylation during volatilization and later in the gas phase is neglected in this assumption. Talmi and Bostick (1975) state that the reduction of MMAA resulted, apart from the expected MMA, in the partial production of AsH_3 , DMA, and TMA. Further, the HG of DMAA produced small amounts of MMA. Pantsar-Kallio and Korpela (2000) found in experiments for $DMA^V A$, that at pH 1 - 2, about 90% of DMAA are volatilized as DMA, the remaining fraction as MMA and TMA. With decreasing pH, the remaining fraction increases to that extent, that at pH less than -0.3 all $DMA^V A$ is converted to TMA.

Feldmann et al. (2004) are skeptic to conclude simply from the volatile species detected by HG to the dissolved species. These analytical uncertainties can be eliminated by separating the species prior to forming hydrides. Using a high performance liquid chromatography (HPLC), easy species separation from solutions is possible as species have different retention times on a chromatography column. The boiling points do not affect the separation when using HPLC. Detection limits are improved by the subsequent use of HG.

Pergantis et al. (1997) observed the variations in efficiency of arsine-generation with the help of deuterium-labeled reagents ($NaBD_4$ instead of $NaBH_4$, and DCl instead of HCl). They concluded that arsines once generated may further react with acids present in the reaction mixture, thus allowing for deuterium-hydrogen exchange.

Interference of the arsenic species can take place with dissolved metal cations. Poor As(III) recoveries occurred in a 10 µg/L As solution when Cu exceeded 0.5 mg/L, Fe(III) exceeded 0.5 mg/L, Cr(VI) exceeded 0.01 mg/L, or Cd exceeded 10 mg/L. Furthermore, high Fe(II) concentrations ($\text{Fe(II):Fe(III)} > 2$) inhibited As(III) oxidation only when Fe(III) exceeded 10 mg/L, what was not the case for the West Nymph Creek Thermal Area (WNCTA) samples. The poor recoveries are the result of hindered arsine production when interfering metal cations compete for the available NaBH_4 and/or when oxidation of As(III) by the interfering metal takes place. Separation of interfering metal cations using cation-exchange prior to hydride-generation permits accurate As(III) determination in waters containing high metal concentrations (McCleskey et al. 2001). When combining hydride generation with an atomic fluorescence, interferences are reduced and detection limit is improved.

Further restrictions of HG is the fact that borohydride does not reduce several organo-arsenicals (e.g. arsenosugars, arsenobetaine, or arsenocholine). A pretreatment of these non-volatile arsenicals is required. Investigated methods for the transformation to arsines are alkaline digestion (de Bettencourt and Andreae 1991), UV-photo-oxidation with $\text{K}_2\text{S}_2\text{O}_8$ (Sur 1999), microwave-assisted oxidation (Le et al. 1993, Sur 1999), or a combination of all three (Yano et al. 2000).

Contaminations in the reducing agent NaBH_4 , interactions and redissolution of the formed hydrides in the headspace increase uncertainties and losses during the analytical process of hydride generation.

4.2.2 High Performance Liquid Chromatography

High performance liquid chromatography (HPLC) was developed in the mid-1970's and quickly improved with the development of column packing materials. New methods including reverse phase liquid chromatography allow improved separation between very similar compounds. The efficiency of HPLC depends on type of column used for the separation of compounds, as well as the choice of the detector to interface with the HPLC in order to get optimal analysis results. The sample solution is injected into the mobile phase, which acts as a carrier for the sample solution. Chemicals of the mobile phase and sample solution interact among each other and with the column, determining the degree of migration and separation of components contained in the sample. The dimensions of the typical HPLC column are 1-3 m in length with an internal diameter between 3-5 mm. "Short columns" have a length of about 3 mm and they are packed with smaller particles. The usual diameter of micro-columns, or capillary columns, ranges from 3 µm to 200 µm (online ASRG 2005).

The separation of arsenic species performed by high pressure liquid chromatography uses ion exchange, or size exclusion chromatography. In a pH between 5 and 7, the elution order is $\text{As(III)} > \text{DMA}^{\text{VA}} > \text{MMA}^{\text{VA}} > \text{As(V)}$. Ion pairing is used with reverse-phase columns, where Tetrabutylammonium is the most commonly used pairing cation. Le et al. (2000)

furthermore determined MMA^{III}A and DMA^{III}A when using a reversed-phase column and a mobile phase of 5 mM tetrabutylammonium hydroxide (TEAH), 3 mM malonic acid, and 5% methanol at pH 5.8.

Garbarino et al. (2002) recommend immediately adding Ethylenediaminetetraacetic acid (EDTA) to filtered water samples, designated for HPLC analysis. EDTA was shown to be appropriate to preserve the distribution of arsenic species by chelating metal cations, to buffer the sample pH, and to reduce microbial activity. Opaque polyethylene bottles should be used to preserve the sample from light. The concentration of the EDTA can be varied, depending on the expected concentration of metal cations (e.g. Fe, Mn, and Al). Only an estimate of the iron concentration is needed because iron is chelated preferentially over other major cations (e.g. Ca and Mg).

4.3 Applied on-site Hydrochemistry

Changes in the water chemistry are often caused by modifications in the environment. Therefore, it was important not only to register and to map the morphology of hydrothermal features but also to consider the water chemistry. In the West Nymph Creek Thermal Area, 18 hot springs have been analyzed. Besides the determination of temperature, redox potential, specific conductance, and dissolved oxygen, some element species (Fe_{tot}, Fe²⁺ and S²⁻) were determined on-site with a field photometer. Arsenic species As(III), As(V), mono- and dimethylated arsenic were separated in the field by solid phase extraction. Furthermore, water samples were filtered and prepared for later analysis in the laboratory. All the bottles used in the field have been cleaned twice with HNO₃ (1M) and washed with deionized water.

4.3.1 Parameters by Electrode

The on-site parameters such as pH, water temperature, specific conductance, redox potential and dissolved oxygen were determined by submerging the specific electrodes from the WTW (Wissenschaftlich-Technische Werkstätten GmbH Weilheim) MultiLine P4 directly into the thermal feature. Values were read from the display of the device (WTW MultiLine P4).

The **pH** was determined with a SenTix 41 pH combined electrode with integrated temperature probe. After about five minutes, equilibrium (pH ±0.01) between the probe and the water was observed. The pH values of the study area varied between 2.3 and 7.1.

The pH is a very sensitive parameter for modeling processes e.g. modeled charge imbalance (5.2.1.3). As the modeled charge imbalance showed a bad correspondence, the pH was redetermined for all the samples about one week after sampling. A BECKMAN 256 pH-Meter equipped with an ORION Thermo ROSS (Model 9107) pH combined electrode with

integrated temperature probe was used to determine the pH in the untreated water samples designated for the ion chromatography.

The **redox potential** was determined with an Ag/AgCl electrode on the WTW MultiLine P4. It was corrected for standard hydrogen potential and temperature according to the following equation based on information provided by the manufacturer (WTW): $E_H(\text{corrected}) = E_H(\text{measured}) + (-0.7443 * \text{temperature } [^{\circ}\text{C}] + 224.98)$. The E_H values were drifting strongly at the beginning of the measurement - redox potential measurement was aborted after an average of 30 minutes even if no steady conditions were obtained. Such samples are marked as “not in equilibrium” in the database. The waters in the study area showed both oxidizing (+610 mV) and reducing (-70 mV) conditions.

The **dissolved oxygen** was determined with a Cellox 325 electrode with integrated temperature probe on the WTW MultiLine P4. The determination of the dissolved oxygen was not possible directly when the water of the sampling site had a temperature greater than 50°C.

The **specific conductance** was determined with a TetraCon 325 Standard Conductivity Cell on the WTW MultiLine P4. The equilibrium for the measurement was reached after about five minutes. Values ranged from 360 to 4320 $\mu\text{S}/\text{cm}$.

The water **temperature** was determined with three different probes: the SenTix 41 pH electrode, the TetraCon 325 conductivity cell, and with the Cellox 325 electrode for dissolved oxygen if temperature was lower than 50°C. The mean temperature was calculated from the two/three determinations. Temperatures varied from 13 to 86°C.

4.3.2 Photometry

Some species like e.g. Fe_{tot} , Fe^{2+} and S^{2-} had to be analyzed on site. Increasing storage time might favor oxidation of these sensitive species by atmospheric oxygen or microorganisms. Prior to analysis, the photometry vials were rinsed 3 times with filtered water from the corresponding sample site. For photometry 10 to 25 mL water were taken from the sampling site with a 10 mL PE syringe and filtered through a 200 nm cellulose acetate filter (Membrex). The photometer used in the field was a HACH DR/890 Colorimeter (Figure 23).

Method 8146 was used for **Fe(II)** determination with a detection limit of 0.01 mg/L. The 1,10-Phenanthroline indicator in the Fe(II) reagent interacts with the Fe(II) in the sample forming an orange colored complex. The color intensity correlates directly with the Fe concentration. In the study area concentrations for Fe(II) varied from below detection limit to about 2 mg/L.

Total iron Fe_{tot} was determined by method 8008 with a detection limit of 0.01 mg/L. FerroVer Iron reagent reacts with all dissolved and most of undissolved Fe species in the

sample to form soluble Fe(II). The Fe(II) reacts with the 1,10-Phenanthroline-Indicator in the reagent to an orange colored complex. Its color intensity is proportional to the total Fe concentration. Total iron concentrations varied from below detection limit to about 2.04 mg/L.



Figure 23: Photometry in the field

The Fe(III) concentration was determined by subtracting the Fe(II) concentration from the total iron (Fe_{tot}) concentration. Values from below the detection limit to 1.84 mg/L were determined.

Method 8131 or Methyl-blue method was applied for the determination of sulfide S^{2-} . The detection range for this method was 0.01 to 0.7 mg/L S^{2-} . Metallic sulfides and H_2S , both soluble in acid, react with the N,N-dimethyl-p-phenylenediaminesulfate to form Methyl-blue. The intensity of the blue color is proportional to the sulfide (S^{2-}) concentration.

4.3.3 On-site Arsenic Species Separation

The ion exchange on solid phases (SPE = solid phase extraction) is a simple, inexpensive and sensitive method for arsenic speciation in the aquatic phase. According to the speciation technique of Le et al. (2000), and Yalcin and Le (2001), a combined set of commercial cation and anion exchangers was used to separate on site As(III), As(V), monomethyl As (MMAA), and dimethyl As (DMAA). The sequence of the exchangers is important: cation exchanger on the top above the anion exchanger (Figure 24). At $pH > 1.6$ the zero valent DMAA species predominates and shows unspecific sorption on both the cation and anion exchange cartridge, while MMAA and As(V) as negatively charged species pass through the cation exchanger and sorb on the anion exchange cartridge only. Concomitant anions, like carbonate, chloride or sulfate can compete with arsenic species for exchange sites on the columns if they occur in increased concentrations, for example high sulfate concentrations in the g/L range in acid mine drainage (Bednar et al. 2004). The

As(III) fraction as zero-valent H_3AsO_3^0 species passes through both exchangers and is collected in solution.

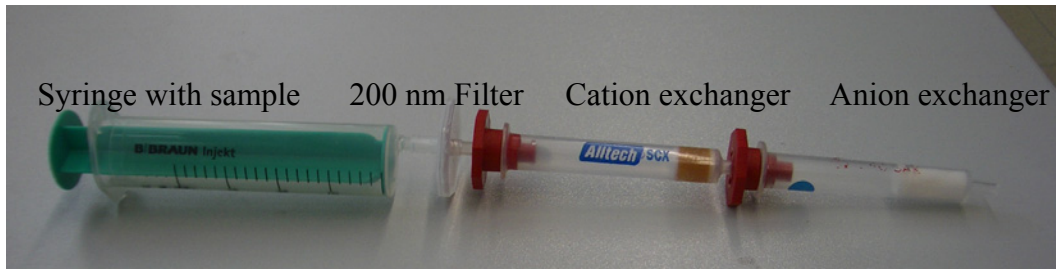


Figure 24: Setup of syringe, cation and anion exchanger for As speciation

The strong cation exchanger (SCX, particle size of 45-150 μm , exchange capacity of 1.9 meq/mL) was acquired from Alltech, the silica based anion exchanger (SAX, particle size of 50 μm , total capacity of 0.14 meq/g) from Supelco. The exchanger material (500 mg) is packed between one mm thick, porous disks in 4 mL cartridges.

The process of conditioning will clean the exchangers by desorption of sorbed ions and regeneration of the functional groups. The ion exchangers got prepared in two different ways. For every sampling spot, one pair of exchangers was conditioned with 10 mL of HCl (1 M), followed by 6 mL methanol (50%) and finally rinsed with 6 mL of distilled water. With syringes, the conditioning solution was first pushed through the cation exchanger followed by the anion exchanger. To achieve a higher buffering capacity and a better long-term stability, Bednar et al. (2004) suggest conditioning the exchangers with 10 mL of acetic acid (1.7 M), followed by 6 mL of methanol (50%) and finally rinse them with 6 mL of distilled water. In their studies acetic acid conditioning showed a recovery of 99% after 47 days of storage, whereas a recovery of 85% for the chloride conditioned form. After conditioning the exchangers were kept in the refrigerator until use.

At the sampling sites 10 mL of sample were taken with a pre-rinsed PE syringe. The water sample was then filtered through a 200 nm cellulose acetate filter (Membrex) and passed through the ion exchangers with a flow rate of 1-2 mL/min. The As(III) fraction was collected in a 20 mL polyethylene (PE) bottle. The exchanger cartridges were disconnected, wrapped in aluminum foil and stored in the refrigerator at about 6°C together with the PE bottles until analysis in the laboratory six weeks later. Elution of the resins and laboratory analysis are explained under 4.4.2.2. Experiments from Le et al. (2000) confirm the stability of the As species on the exchangers for that period of time.

4.3.4 Water Samples

To preserve the species distribution in water samples and to protect species from conversion by oxidation, reduction, complexation, and biotically catalyzed reactions the following sample preparation and conservation measures were taken. In brackets the analyzed species and the location of the analyzing laboratory.

- 100 mL PE bottle, no treatment → IC (anions, Boulder)
- 100 mL glass bottle, no treatment → TOC / TIC (Freiberg)
- 50 mL PE bottle, filtered, 500 μ L 6 N HCl¹ → HG-AAS (As, Boulder)
- 50 mL PE bottle, filtered, 500 μ L conc. HNO₃ → ICP-AES (Boulder)
- 50 mL PE bottle, filtered, 0.25 M EDTA² → HPLC-ICP-MS (As, Denver)

Filtration was done with 200 nm cellulose acetate filter (Membrex). The adequate bottles have been cleaned twice with HNO₃ (1 M) and rinsed with distilled water. Bottles for IC and TOC / TIC were rinsed on site twice with non-filtered sample water; bottles for the AAS, ICP-AES, and HPLC-ICP-MS were rinsed twice with filtered sample water.

4.4 Laboratory Methods and Settings

The As species were determined in three different laboratories (Freiberg, Boulder, and Denver), using different species separation methods, and different detection methods. The following paragraphs explain in detail the methods, and the setups of the devices.

4.4.1 Species Detection Methods

The species detection after HG can be done by AAS (atomic absorption spectrometry), ICP-AES (inductively coupled plasma - atomic emission spectrometry), AFS (atomic fluorescence spectrometry), GC (gas chromatography), or ICP-MS (inductively coupled plasma - mass spectrometry). The ICP techniques are especially interesting for multi-element analysis. ICP-AES is used mostly for samples with higher As concentrations. About 100 to 1000 higher sensitivities are reached by incorporating a hydride generation (HG) step between HPLC and ICP-AES or ICP-MS, thus providing corrections for the Cl-Ar interferences.

4.4.2 Atomic Absorption Spectrometry

Atomic absorption is the process that occurs when a ground state atom absorbs energy in the form of light of a specific wavelength and is elevated to an excited state. The amount of light energy absorbed at this wavelength increases with the number of atoms of the selected element in the light path. By measuring the amount of light absorbed, a quantitative determination of the amount of analyte can be made. Unknown concentrations are

¹ Method proposed by McCleskey & Nordstrom (2002)

² Method proposed by Bednar et al. (2004)

determined in relation to known concentrations in standard solutions. The use of special light sources and careful selection of wavelengths allow the specific determination of individual elements. Interferences of dissolved metal ions associated with atomic absorption analysis are negligible because the gaseous arsine (AsH_3) is separated from the sample matrix. The major limitation of atomic absorption using flame sampling is that only a small fraction of the sample reaches burner-nebulizer system, and the atomized sample passes quickly through the light path.

4.4.2.1 Determination of As(III) and Total Arsenic Using Hydride Generation - Atomic Absorption Spectrometry

Water samples were collected in the field, filtered through a 200 nm pore size filter, 50 mL of sample were acidified with 500 μL 6N HCl to a $\text{pH} < 2$, and stored in acid-washed opaque PE bottles in the refrigerator. All water samples and standards were prepared in 25 mL volumetric flasks.

Total dissolved arsenic species As and As(III) in the samples were determined by hydride generation - atomic absorption spectrometry (HG-AAS) at the USGS National Research Laboratory in Boulder, Colorado, USA. The total As is made up of the As(III) plus As(V) concentration. An atomic absorption spectrometer (AAS) (Perkin-Elmer Analyst 300) was equipped with an As electrodeless discharge lamp (EDL) as primary light source, electrically heated quartz cell with a 15 cm path length to atomize the sample, a monochromator to isolate the specific wavelength of light to be used, and a flow injection analysis system (FIAS) (Perkin-Elmer FIAS 100). The following spectrometer parameters were used: EDL current of 380 mV, wavelength of 193.7 nm, and 0.7 nm slit width. Peak height was used for data processing. The following FIAS settings were used: argon as carrier gas, cell temperature of 900°C, sample loop of 500 μL , HCl (10 percent) carrier solution with a flow rate of 10mL/min, reducing agent: 0.25 percent (total As) or 0.03 percent (As(III)) sodium borohydride (NaBH_4) in 0.05 percent sodium hydroxide (NaOH) with a flow rate of 5 mL/min. The efficiency of arsine generation depends on the valence state of arsenic. Since As(III) is reduced to arsine much easier than As(V), As(V) is pre-reduce to As(III) using potassium iodide (KI) and L-ascorbic acid, 10 percent (w:v) each. In 10% conc. HCl at a $\text{pH} \ll 1$ the hydride generation for total As was performed. The hydride generation for As(III) was performed in 2% HCl at a pH of 1 - 2 (statement McCleskey 2005). The detection limits of the HG-AAS analytical procedure used at the USGS laboratory in Boulder are 0.5 $\mu\text{g/L}$ for total As and 1.0 $\mu\text{g/L}$ for As(III).

At a constant carrier concentration (HCl 10%, pH about -0.5) and FIAS flow rate, increasing the NaBH_4 concentration increases the sensitivity of the As(III) determination. However, when the NaBH_4 concentration exceeds 0.0625 percent, As(V) is reduced, causing an overestimation of As(III) (McCleskey et al. 2003). To ensure selective reduction of As(III), the NaBH_4 concentration was maintained at 0.03 percent for the As(III) determination.

The best choice of preservative for As redox species determination by HG-AAS is hydrochloric acid (HCl) because of the approximation of the sample matrix to the HCl carrier solution. However, samples preserved with hydrochloric acid interfere in the As-determination if an ICP-MS is used due to the $^{40}\text{Ar}^{35}\text{Cl}^+$ molecular interference on monoisotopic $^{75}\text{As}^+$ (Garbarino et al. 2002).

4.4.2.2 Determination of As(III), As(V), MMAA, and DMAA Using Field Separation and Graphite Furnace - Atomic Absorption Spectrometry

Details on the commercial cation and anion exchangers, used to separate on site As(III), As(V), monomethylated As acid (MMAA), and dimethylated As acid (DMAA) are explained under 4.3.3. While DMAA shows unspecific sorption on the cation exchanger (SCX) and As(V) and MMAA are sorbed on the anion exchanger (SAX), As(III) as zero-valent H_3AsO_3^0 species passes through both exchangers.

The ion exchangers were eluted in the laboratory at the TU Bergakademie Freiberg. Both pairs of ion exchangers, the acetic acid conditioned anion and cation exchangers (SAX-AA and SCX-AA), and the hydrochloric acid conditioned anion and cation exchangers (SAX-HCl and SCX-HCl) were eluted in the same way. First, the MMAA fraction was desorbed from the anion exchangers; the elution was done with 10 mL of 60 mM acetic acid. This elution was done once, in order to not remove the As(V) fraction, sorbed on the same exchanger. To recover the complete As(V) fraction from the SAX, the exchanger was eluted twice with 10 mL of 1N HCl. The DMAA fraction was desorbed from the cation exchangers (SCX), using twice 10 mL of 1N HCl.

The acetic acid eluents, the hydrochloric acid eluents, and the water samples with the As(III) fraction were analyzed by a GF-AAS (Zeiss EA4 spectrometer) using graphite furnace with platform technique at the TU Bergakademie Freiberg. With graphite furnace atomic absorption, an electrical heated graphite tube replaces the conventional flame. The sample is introduced directly into the tube, which is then heated in a programmed series of steps to remove the solvent and major matrix components and then to atomize the remaining sample. The entire sample is atomized, and the atoms are retained within the tube (and in the light path that passes through the tube). As a result, sensitivity and detection limits are significantly improved for a GF-AAS compared to flame AAS. The calibration was done with matrix-matched standards.

The AAS-EA4 from Zeiss was equipped with an As hollow cathode lamp (HCL) with a wavelength of 193.7 nm and a gap width of 60 nm. A deuterium lamp is used for the background correction. 15 μL sample solution are introduced with 8 μL $\text{Pb}(\text{NO}_3)_2$ as modifier to fix arsenic.

Table 6 shows the temperature-time-program used for the analysis with GF-AAS. The detection limit for all four species was 3 µg/L.

Table 6: Temperature-Time-Program for the As eluent determination with the GF-AAS (Zeiss EA4).

Step	Temp (°C)	Ramp (°C/s)	Hold (s)	Time (s)
Drying	120	10	0	10.1
Drying	150	3	30	40.0
Dry ashing	1350	135	30	38.9
Atomization	2400	Full power	4	4.7
Cleaning	2600	1000	3	3.2

4.4.3 Determination of Multiple Elements Using Inductively Coupled Plasma - Atomic Emission Spectrometry

The inductively coupled plasma - atomic emission spectrometry (ICP-AES) used for these investigations was a Leeman Labs Direct Reading Echelle (Model DRE-D) at the U.S. Geological Survey, National Research Laboratory in Boulder, Colorado, USA. The atomic emission spectrometry (AES) is a technique to analyze liquid samples for dissolved metals. There are two fundamental principles on the basis of the AES: first, every element, when excited, will emit light at a unique, characteristic wavelength, and, second, the intensity of the emitted light is directly proportional to the number of atoms present. The temperature at which an atom will be excited enough to emit light is characteristic of that element. Operating temperatures are about 7.000 to 9.000°C.

To perform this analysis, the system requires an inductively coupled plasma (ICP) source to provide excitation energy, coupled to a direct reading echelle (DRE) spectrometer to separate and measure the emitted light. The plasma itself is a conducting gaseous mixture containing a significant concentration of cations and electrons. The plasma of the Leeman Labs DRE-D is formed with argon (Ar) gas, using energy supplied by a radio frequency generator. Power ranges are typically 1.0-1.2 kW at 40.68 MHz, enough energy to ionize or remove an electron from the normally inert Ar atom.

The function of the spectrometer is to detect the light from a particular element in the plasma, and convert the light to an electrical signal that can be used by data acquisition electronics and later converted to a meaningful analytical measurement. ICP-AES is a multi-element technique, which can determine 10-40 elements per minute in individual samples. The following elements were determined: As, Al, B, Ba, Be, Ca, Cd, Co, Cr, Cu, Fe, K, Li, Mg, Mn, Mo, Na, Ni, Pb, Si, Se, Sr, V, and Zn. Information about detection limits and scan mode (axial or radial) is given in the digital database.

4.4.4 Determination of As(III), As(V), MMAA, and DMAA Using High-Performance Liquid Chromatography - Inductively Coupled Plasma - Mass Spectrometry

For the chromatographic separation of arsenite, arsenate, monomethylarsonate, and dimethylarsinate a HPLC (Agilent 1100 Series) at the National Water Quality Laboratory, Denver Federal Center, U.S. Geological Survey was applied using ICP-MS as an element-specific detector. The following chromatographic parameters were set: a Hamilton PRP-X100 (250 mm by 4.1 mm) analytical column was operated at 30°C. Instead of using isocratic elution, a step-gradient elution was used to shorten the elution time of MMA and As(V) by more than 1 min. A 38-75 mM phosphate buffer at a pH of 5.7 was used as the mobile phase. During the gradient program, the molarity of the phosphate mobile phase was adjusted with reagent water using the proportioning valves of the HPLC. The elution time was about 7 minutes and the detection limit is 0.1 µg/L. Further, the arsenic species were converted to arsines as they eluted from the column to improve the method detection limit (MDL), prevent salt build-up on the ICP-MS cones, and eliminate chloride interferences (Bednar et al. 2004).

Arsine generation was realized with a Perkin-Elmer FIAS mercury/hydride module, combined with a flow injection ICP-MS vapor adapter kit. The efficiency of arsine generation depends on the original valence state of the arsenicals. Since As(III) is reduced to arsine much easier than As(V), As(V) is pre-reduce on-line after being eluted from the column. Routinely, potassium iodide (KI) has been used for pre-reduction, but arsine generation in a continuous-flow system requires a faster reaction. Chen et al. (1992) reported that L-cysteine could be used to quickly pre-reduce As(V) to As(III). A 2.5% (weight-to-volume, w:v) solution of L-cysteine was used under mild acid conditions to convert As(V) to As(III). A solution of 0.5% (w:v) sodium borohydride (NaBH₄) was used to reduce As(III) and methylated As species to arsine. Analytical column effluent, L-cysteine, and 0.3 M nitric acid (HNO₃) were mixed in a coil that was heated to 95°C to aid the conversion of As(V) to As(III). The NaBH₄ reagent was introduced into a three-way mixing block just prior to the three dimensional reactor. The heating caused water vapor to condense on cooler surfaces of the gas/liquid membrane separator. Consequently, a manifold cooled to 5°C with a recirculating chiller was added to eliminate the condensation. Bednar et al. (2004) state, that the cooling enhanced the efficiency of the gas/liquid membrane separator and did not affect arsine generation efficiency. The addition of the cooling manifold improved the detection limit and increased data quality.

HPLC column effluent was introduced into an ICP-MS (PE Sciex Elan 6100), used as an arsenic-specific detector. The ICP-MS uses the ability of the argon ICP to generate efficiently single charged ions from the elemental species. Ions from the ICP are introduced into the mass spectrometer and are separated according to their mass-to-charge ratio (m/z). Ions of the selected mass-to-charge ratio (e.g. 75 for arsenic) are directed to a detector, which quantifies the number of ions present. The retention time and the chromatographic

peak width determine the dwell time and readings per replicate. The sampling frequency should be at least 10 times the narrowest chromatographic peak width. For example, for a peak 10 s wide, the sampling frequency should be 1 Hz or a dwell time of about 1 s. The typical dwell times were 0.5 to 0.75 s. The number of readings per replicate was used to establish the total elution time.

The detection limit of the HPLC-ICP-MS was 0.3 µg/L for As(III) and DMAA, 0.4 µg/L for As(V), and 0.6 µg/L for MMAA.

4.4.5 Other Analytical Methods

The dissolved organic carbon (DOC) and the total inorganic carbon (TIC) were determined with a LiquiTOC (Elementar Analysesystem GmbH) at the TU Bergakademie in Freiberg. For TIC and DOC determination, untreated water samples were preserved in 100 mL glass bottles and stored in the refrigerator until analysis.

The concentrations of the major anions Cl^- , SO_4^{2-} , F^- , Br^- and NO_3^{2-} were determined by ion chromatograph (IC) at the U.S. Geological Survey, National Research Laboratory in Boulder, Colorado. The ion chromatography in use was a Dionex DX 500 system, model 2010i, equipped with AG4A guard and AS4A separator columns and an anion micromembrane suppressor-II column. The eluent was 0.018 M NaHCO_3 + 0.017 M Na_2CO_3 . The detection limits for the selected anions were Cl^- : 0.2 mg/L, SO_4^{2-} : 2.0 mg/L, F^- : 0.1 mg/L, Br^- : 0.1 mg/L, and NO_3^{2-} : 0.5 mg/L. For the IC, 100 mL water sample were preserved untreated in PE bottles in the refrigerator. In case of high anion concentrations, samples were analyzed at three different dilutions (1:50, 1:10, and 1:2).

5 Results and Discussion

5.1 Digital Atlas¹

The atlas shows the results of hydrogeological and hydrochemical investigations in the West Nymph Creek Thermal Area of the Yellowstone National Park, Wyoming, USA from different points of view. The subdivision into three sections helps to find any information required:

- 1) Study Area (TNT Digital Atlas)
- 2) Help (pdf-file)
- 3) MS Access Database

The “Study Area” Layout gives a general idea about the location of the West Nymph Creek Thermal Area (WNCTA) in the Yellowstone National Park. Further, detailed information including geological and hydrological settings, a digital elevation model (DEM), the major roads, an extract of the topography map of the park, as well as different vector and raster objects on hydrochemistry, the geothermal situation, characteristics and distribution of the geothermal features are presented. Additional data, such as mapping notes about the hydrothermal features and hydrochemistry data, is included in tables linked to the vector objects.

The digital atlas should be considered as a snapshot of the thermal features and presents a basis for future observations. The high-resolution aerial pictures allow tracing the fast changes in morphology and hydrochemistry of the hydrothermal features. TNTmips version 6.8 was the GIS-software used to create the digital atlas of the WNCTA. For displaying, browsing and sharing the atlas without the full licensed version of TNTmips, the public domain software “TNT atlas for x” from MicroImages is provided.

¹ The digital atlas was delivered separately as Scientific Report.

5.1.1 Data Check - Measuring Tape vs. Digital Determined Lengths

To scrutinize the confidence of distance measurements in the resampled mosaic, distances between ground control points were determined in the field with a measuring tape (Figure 25). At four sites, the distances between four crosses (4 side lengths and 2 diagonals) were determined to compare them to the mosaicked values. With the “GeoToolbox” from the TNTAtlas the distances were calculated in the 0.019 m cell size mosaic.

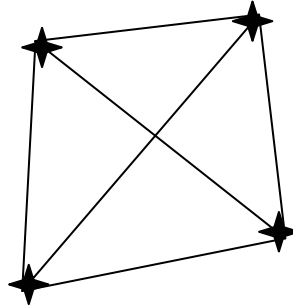


Figure 25: Measurements taken between the Ground Control Points

For the 24 measurements and the calculations, the absolute difference was determined. The comparison was done by calculating the mean of the absolute values. An absolute average deviation of 0.41 m (s.d. 0.3 m) between measured and calculated distances was determined. The best fit for the two values was 0.05 m and the most significant deviation was 1.14 m (Appendix 1). The mean range of analysis is 0.9%. Independent of the distance between two points, the determination of distances with the “GeoToolbox” has an accuracy of ± 0.2 meters. Despite the Piecewise Affine resampling models, distortions in the mosaicked aeriels were inevitable. On the other hand, the accuracy of the differential GPS measurements depends on various parameters (3.1.2). Increasing distance from the rover to the base station influences the accuracy negatively.

The horizontal accuracy for post-processed coordinates determined with the Trimble differential GPS receiver Pathfinder Pro XR is about 0.50 m. A higher accuracy requires a carrier postprocessing, a longer satellite tracking and a closeness of < 500 km to the base station.

Browsing the Atlas

From the Homepage of the digital atlas, users choose their section of interest: Study Area, Help File, Microsoft Access Database or the Master Thesis (Figure 26).



Figure 26: Homepage of the Digital Atlas

The navigation through the section “Study Area” and the available information in this section is explained below. Clicking on the link “Study Area” opens the actual Digital Atlas and shows the following toolbar and the opening screen (Figure 27).

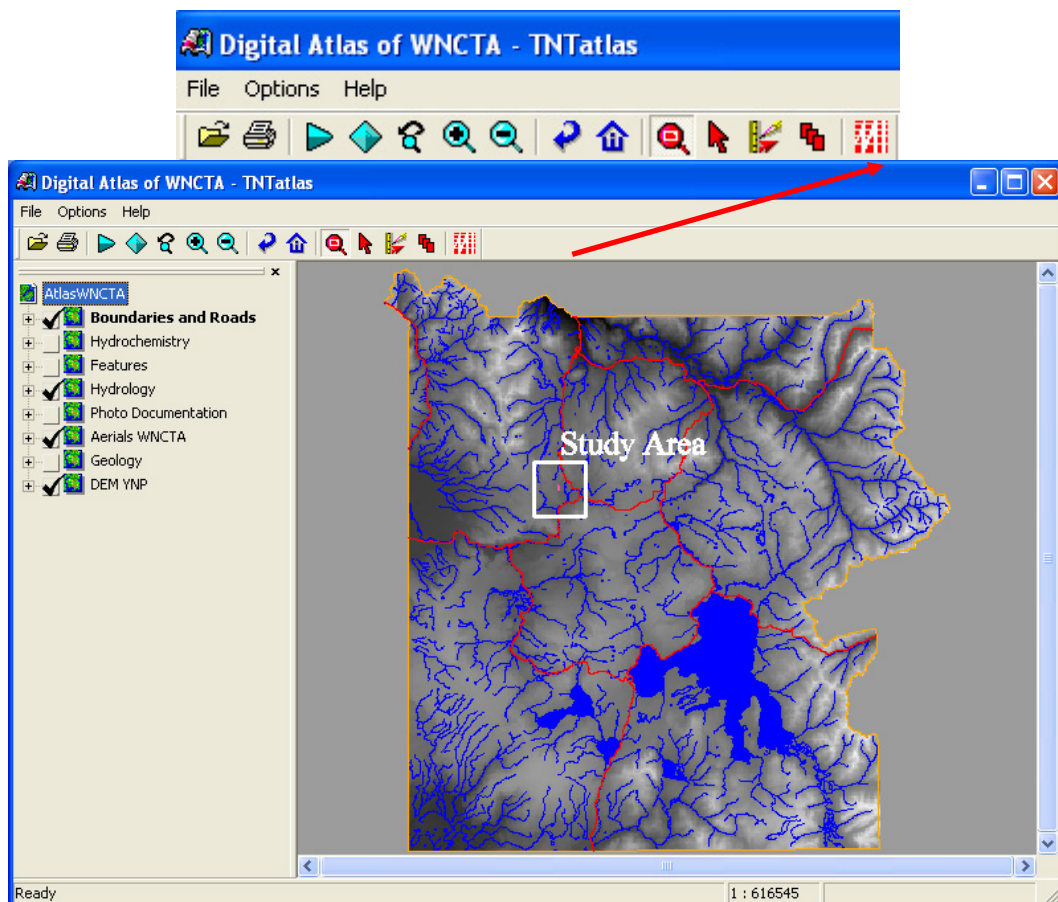




Figure 27: Toolbar and opening screen of the digital atlas

5.1.1.1 Navigation tools


 **Hyper Index Navigator:** On initially opening the Home page, activate this icon, click on the blue marked text of the section titles and the corresponding atlas layout (Study Area), pdf-file (Help File and Master Thesis) or database (Access Database) will open. This tool is also necessary in the section “Study Area”, group “Photo documentation” where photos are linked to the corresponding vector-points or in the group “Geology”, where legends are linked to the geological map.

 **Back to home level:** opens the start page of the atlas.


 **Navigate back:** opens the previous link/level.


5.1.1.2 Viewing tools

The following tools allow changing the view of the different layers. Mouse-Over will pop-up when approaching the mouse cursor over the icons in the toolbar. Additional information is displayed in the status bar at the lower left corner of the window.


 **Full view:** zoom to the full extents; size of the largest layer.

 **Redraw the view:** use after selecting a new layer to refresh the view.

 **Previous view:** restore previous view and zoom.


 **Zoom in:** scale up.


 **Zoom out:** scale down.

 **Zoom Box:** activates zoom box tool; select a section to enlarge and confirm with right mouse button.

5.1.1.3 Working tools

Several tools allow the user to work on the displayed layers. The following tools are provided by the TNTAtlas.

 **Geo Toolbox:** gives different possibilities to measure lengths, areas and to draw sketches. For example, distances between ground control points (in the group “Features”, layout “Ground Control Points”) and other features can be determined.

 **Select:** use this icon to select features and structures of vector objects. If a table is linked to the selected structure, it will open.

Right mouse: click the right mouse button on the corresponding **group** and make a choice (Figure 28):

- activating (displaying) group
- show/hide all layers
- expand/collapse all layers

Right mouse on **layer**:

- data tip
- zoom/view extents (metadata information)

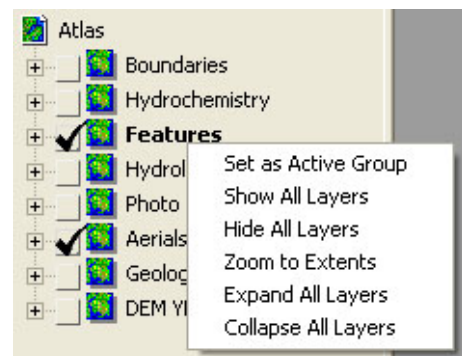


Figure 28: Right mouse on group

5.1.1.4 Groups and Layers

The atlas layouts are subdivided into several thematic groups that are further separated in different layers. The default overview shows only the basic groups and layers. For combining different layers, click on the grey rectangle to the left of each group to display it. The group opens and it is possible to select different layers. Displaying the layer also opens the corresponding legend (Figure 29). If this is not the case, clicking on the plus sign to the left of the layer title opens the legend view.

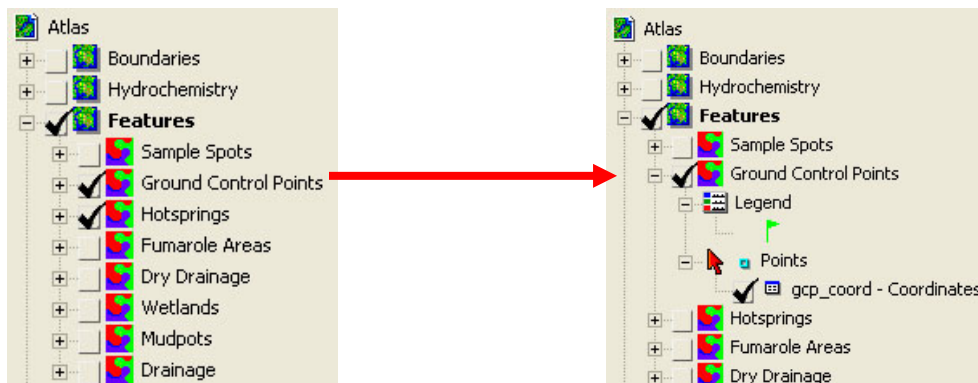
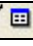





Figure 29: Opening the layer displays the legends

Tables with further information are connected to the vector layers. All available information for each feature is displayed when opening the data-table in the layer manager window by activating the black check  gcp_coord - Coordinates

To get information on a single feature, choose the select icon  and click on the structure. Open the corresponding data-table in the layer manager window, the structure of interest is marked by a red point in the table  WNCTA01. Vice versa, selecting a record in the table marks the corresponding feature in the layer in pink (select the record by clicking on the grey rectangle left of the record and then click on “Select elements” ).

In the menu “Table” users can switch between “Single record view” and “Tabular view”. When a record contains numerous data the “Single record view” is recommended for a better overview. For comparing different data, the “Tabular view” is suitable.

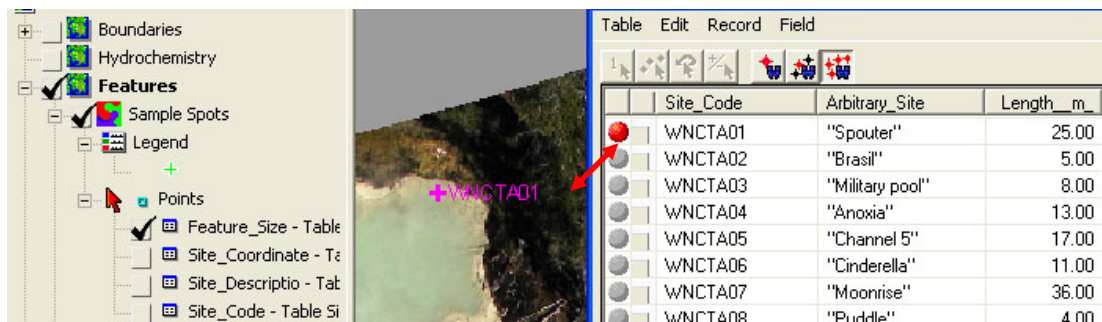


Figure 30: Selection of elements can be done in the map or in the related datatable

5.1.1.5 Groups and Individual Layers of the Atlas

All the layers of the groups were georeferenced based on the settings from the georeference process (Projection: UTM zone 12; Method: Transverse Mercator; Datum: North American 1983; Type: Geodetic; Epoch: 1986; Ellipsoid: GRS 1980).

Detailed information on georeference is displayed by right mouse click on the layer and “View Extents” in the pop-up window.

Groups and *Layers* of the atlas are:

Boundaries and Roads: contains vector layer *Study Area*, the vector layer *Boundary Study Area*, and the vector layer *Boundary YNP* (Spatial Analysis Center, Yellowstone National Park 1995). The vector layer *Major roads YNP* illustrates the course of the Park's major roads (Spatial Analysis Center, Yellowstone National Park 1997).

Hydrochemistry: contains eleven layers, which highlight measurements of *Temperature*, *pH* and *Conductivity* from a survey campaign by the National Park Service (NPS) and from a personal survey campaign. From on-site measurements, the *Iron* speciation (Fe II and Fe III) was determined and is displayed in yellow/orange pie charts. From the determination of the major anions, *Chloride* and *Sulfate* are displayed as characteristic species in thermal waters. *Arsenic* speciation (As III, As V, DMAA, MMAA) was done by two different techniques: a) elution of ion exchangers and determination by AAS and b) HPLC-ICP-MS.

To read more about hydrochemistry, sampling and analysis techniques, browse the data tables in the attached MS Access database (link from Homepage).

Features: the layer of the eighteen *Sample Spots* contains additional data-tables with information on size and characteristics of the features. *Ground Control Points* (gcp) displays all the points, where the coordinates have been determined by differential GPS. *Hotsprings* lights-up all the springs (surging and dormant). *Fumarole Areas* shows all the areas where degassing activity was detected. *Dry Drainage*, *Wetlands*, *Mudpots* and *Drainage* show the distribution of these structures in the West Nymph Creek Thermal Area.

Hydrology: two vector layers show the *Rivers* (National Park Service Water Resources Division 2001) and the *Major lakes* (Spatial Analysis Center, Yellowstone National Park 2000) of the park. Selected standard output layers from the TNT Watersheds¹ modelling process are the two vector layers *Standard flow paths* and *Watersheds polygons and pour points*. Selected standard output raster layers are *Watershed polygons*, *Flow directions*, *Flow accumulations*, *Flat areas & extrema point* and *Adjusted elevation* (extract from the DEM).

Photo Documentation: this layer contains 88 linked jpeg-pictures of the study area. To look at the pictures, activate the Hyper Index Navigator (see Navigation Tools) and click on one of the white camera icons in the layer. In MS Windows, the pictures open automatically in the default picture-viewing program.

Aerials: the raster object *Mosaicked aerials from balloon* is based on the aerial photos taken from the balloon. Ground control points were marked as reference crosses on the

¹ **Watersheds:** in *TNTmips, Process, Raster, Elevation, Watershed*, an extract of the digital elevation model (DEM) was processed; default settings for output file.

ground and their corresponding coordinates from the differential GPS measurements were taken for georeferencing the balloon images (see also GCP in group Features).

After the 50 images were mosaicked¹, the aerial overview was georeferenced² a second time and then resampled³. The original output overview has a raster cell size of 0.019 m and a file size of 4.6 GB. To reduce size and required processing time (CPU) the raster was resampled to a raster cell size of 0.025 m (25 mm) and a file size of 1.8 GB. The raster object layer *Aerial YNP DOQQ Norris junction nws* (Digital Orthophoto Quarter Quad) is provided by the Spatial Analysis Center, Yellowstone National Park 1998. The resolution of the raster cells is 1 m. *Topo YNP Norris Junction 7.5 USGS quads* shows an extract of the Topographic map of the YNP (Spatial Analysis Center, Yellowstone National Park 1998).

Geology: two vector layers include information about the shape of the *Domes* and the *Caldera* in the Park area (by Henry Heasler, National Park Service, written communication). The raster layer *Geology YNP* (Christiansen 2001) was georeferenced and extracted to the extensions of the Yellowstone National Park. The coordinates are not exact because of the rough adaptation. Using the Hyper Index Navigator tool and clicking anywhere in the layer opens the legend (part A and B) of the geological map (imaging-files).

DEM YNP: The raster layer *DEM YNP* (Digital elevation model, provided by the Spatial Analysis Center, Yellowstone National Park 1998) with a ground resolution of 10 m was extracted to the extensions of the Yellowstone National Park. Light colors (grey and white) represent elevations; dark colors (dark grey and black) depressions. The elevation in feet is shown for the active layer by the mouse-over function. Notice that the layer has to be active (black box around) to apply this function. *DEM WNCTA* is an extract of the *DEM YNP* to reduce the required processing time.

5.1.1.6 Legends of the Layers in the Group Hydrochemistry

In all the other groups, the legends of the layers are more or less self-explicit. Because of the large amount of hydrogeochemical data for every sample spot, explanations how this data is displayed are necessary.

¹ **Mosaic process:** *Input:* georeferenced aerials, automatic positioning and in some cases manual positioning by tie points, *Image area:* whole raster and sometimes processing area, *Parameters Mosaicking options* – Piecewise affine, cubic convolution, last raster, *Output* - null value from none to set 255, nothing else changed in the default settings.

² **Georeference process:** Model – piecewise affine, projections see 3.4.2.1.

³ **Resample process:** automatic, Model - piecewise affine, Resample - cubic convolution, Scale - by cell size, Orient – to projection, Extents - entire input, Output extents - default settings, Output Projection – UTM (same as input), Output cell size (m) – 0.025, Null Value - user defined 255

The group **Hydrochemistry** contains eleven different layers. The legends are made up by different numbers of classes with user-defined intervals for each parameter. Legends open by clicking in the small box. Data tables contain standard and additional information. All data originates from tables of the Microsoft Access database.

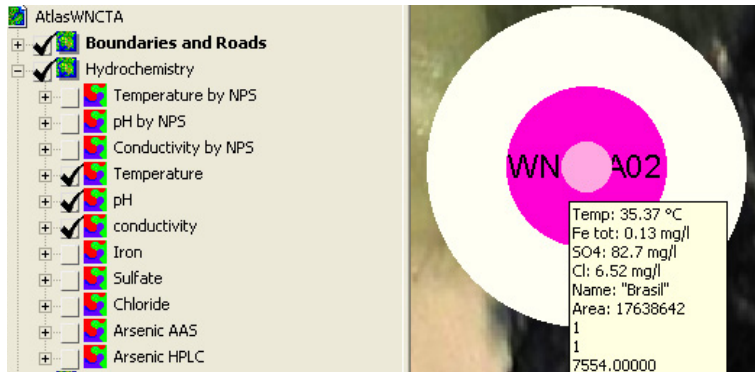


Figure 31: Enlarged labels and mouse-over of one feature

Most of the features are invisible at first sight because of the size of the graphic label. Zooming into the layer will automatically enlarge the labels. Activating the layers *Temperature*, *pH* and *Conductivity* and zooming on a sample spot (in this case it was done for WNCTA02) will show the following information:

Rose circle in the center: Temperature. In this layer the mouse-over function is activated and gives information on exact temperature, total iron, sulfate and chloride concentrations, as well as the arbitrary name of the feature and the elevation in feet. The pink circle represents the pH; this layer displays the site code (id name) of the sample spot. The large white circle represents the specific conductance (Figure 31).

The interpretation of the *Iron speciation* (Fe II and Fe III) is done by yellow and orange pie charts. The size of the pie will not vary while zooming. The pie is labelled and gives exact information on the iron species concentrations. The mouse-over function is activated and data tables exist (Figure 32).

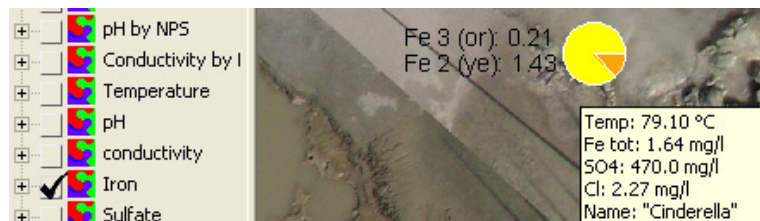


Figure 32: Pie shows the iron speciation

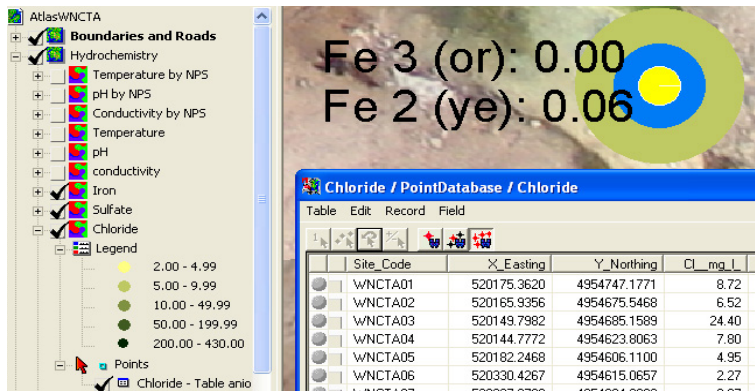


Figure 33: Labels for iron, sulfate and chloride

Iron, Sulfate and Chloride can be displayed together. For iron speciation (yellow circle) see above, sulfate is represented by the midsize circle (here: blue), chloride by the largest, lowermost circle (olive green). Data tables and mouse-over function are active (Figure 33).

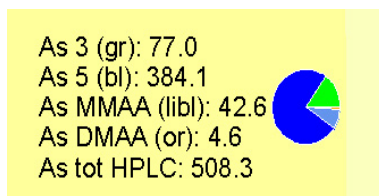


Figure 35: Label for the arsenic speciation by HPLC

The arsenic speciation is displayed in pie charts. An example for the HPLC arsenic speciation is given in Figure 35. The arsenic share (in µg/L) is printed to the left of the chart. The abbreviations of the colors are: green = gr, blue = bl, light blue = libl, orange = or. Arsenic speciation done by AAS is displayed in an identical way: pie charts are smaller and the concentrations are printed on to the right of the

diagram. This way, both layers are displayed together (Figure 34). Additional data is provided in data tables and in the Microsoft Access database.

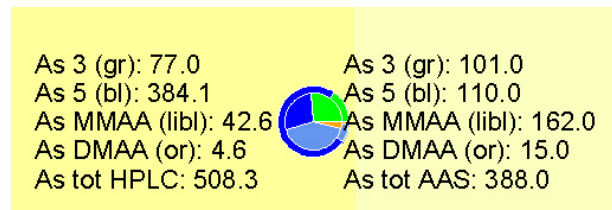


Figure 34: Arsenic speciation by HPLC and AAS

5.2 Analytics

5.2.1 Data Quality Check with Charge Imbalance

In ideal aqueous solutions, the sum of the equivalents of anions and cations must be zero. However, analytical errors and unanalyzed constituents in chemical analyses generally cause electrical imbalances to be calculated for natural waters. The accuracy check of the water analysis was done by calculating the charge imbalance with the hydrogeochemical modeling programs WATEQ4F v3.18 (Ball and Nordstrom 1991) and with PHREEQC 2.8.03 (Parkhurst and Appelo 1999) combined with the database WATEQ4F (V.2.4 with revised data from Nordstrom and Archer 2003).

WATEQ4F and PHREEQC are chemical speciation codes for natural waters that use field measurements of temperature, pH, E_H , dissolved oxygen, alkalinity, and the chemical analysis of a water sample as input and calculate the distribution of aqueous species, ion activities, and mineral saturation indices. The program WATEQ4F uses the following equation:

$$\text{Percent Error} = \frac{100 * (\sum \text{ cations } [\text{ meq/L }] - \sum \text{ anions } [\text{ meq/L }])}{0.5 * (\sum \text{ cations } [\text{ meq/L }] + \sum \text{ anions } [\text{ meq/L }])}$$

Thus, the maximum value of the result of this calculation is ± 200 percent caused by the “0.5” in the denominator. A value of zero for the percent error denotes exact electrical balance, whereas differences of $> 10\%$ suggest errors in the analytical input values. Differences of $< 10\%$ are considered as tolerable. Values $< 5\%$ are considered as accurate. This charge imbalance calculation is twice the charge imbalance normally computed e.g. PHREEQC uses the same equation without the “0.5”. Thus for PHREEQC, differences of $> 5\%$ suggest errors in the analytical input values, differences of $< 5\%$ are considered as tolerable, and values $< 2\%$ are considered as accurate. Since a proportional error in both the cation and anion concentrations will not be detected by PHREEQC, Rossum (1975) proposed using the difference between measured and calculated specific conductance to identify such errors (see 5.2.1.1).

Values below detection limit were replaced by $0.3 * \text{detection limit}$ in all modeling programs. Concentrations of H^+ and OH^- were always included because of the wide range of pH from 2.0 to 7.5 covered by the individual samples. Within the pH range of 5 to 8, neither H^+ nor OH^- will contribute significantly to specific conductance. In acid waters, H^+ is the predominant cation, and slight changes in the pH can already alter the ion balance significantly. Field pH is generally considered the most accurate. However, using the field pH together with the unrevised analytical data in WATEQ4F, errors for the charge imbalance up to 100% for individual samples were detected.

5.2.1.1 Charge Imbalance by PHREEQC

A method to check the data for its accuracy is the comparison of the calculated specific conductance with the measured specific conductance. Unlike WATEQ4F, the measured specific conductance is not an input parameter for the PHREEQC calculations. The considered parameters were pH, temperature, p_e ($16.9 * E_H$), Al, As(III), As(V), B, Br, Ca, Cl, Cu, F, Fe(II), Fe(III), C(IV), K, Li, Mg, Na, N(V), Si, S(-II), S(VI), Sr, and Zn. A prime example of a single parameter that can influence the ion balance significantly is the pH. For samples with a $pH \leq 5$, the laboratory pH is in general 0.9 pH units lower in comparison to the field pH - a maximum lowering of 1.5 pH units is detected for the samples WNCTA07 and WNCTA09. The laboratory pH of samples with a $pH > 5$ drifts in average ± 0.3 pH units from the field pH. The overall variance between field and laboratory pH determination is ± 0.6 pH units.

Laboratory pH values in general (16 out of 18 samples) yielded lower errors for the charge imbalance. For all samples a “best fitting pH”, within the range of the field pH and the laboratory pH, was determined manually (change the pH by steps of 0.1 and rerun the modeling process) to minimize the analytical error. Adaptations of the pH by ± 0.1 units were sufficient to result in analytical errors $< 1\%$. Out of eighteen samples, twelve samples presented errors $< 2\%$, two samples presented errors $< 5\%$ and the remaining three samples presented errors $> 5\%$. The maximum detected error was -12.5% for WNCTA18 (Table 8).

5.2.1.2 Measured vs. Calculated Specific Conductance after Rossum (1975)

The adapted pH values were used together with the species concentrations determined by species modeling with PHREEQC for calculating the specific conductance. These adapted pH values correspond to the “best fitting pH”, a pH in the range of field determination and the laboratory determination, resulting in the lowest analytical error. The applied method by Rossum (1975) to calculate the specific conductance takes care of the contributions of individual species to the total specific conductance. Extrapolated values for equivalent conductance of Al^{3+} , Ba^{2+} , Br^- , Ca^{2+} , Cl^- , CO_3^{2-} , HCO_3^- , F^- , Fe^{2+} , Fe^{3+} , H^+ , OH^- , K^+ , Li^+ , Mg^{2+} , Na^+ , NO_3^- , HSO_4^- , SO_4^{2-} , and Sr^{2+} in the standard state of infinitely dilute solutions at $25^\circ C$ were taken from Rossum (1975), completed by those listed in Coury (1999). The specific conductance is calculated systematically in Excel from the equivalent conductance of the individual anions and cations and in dependence of the species' concentration, determined by species modeling in PHREEQC. Zero valent complexes stay unconsidered.

If the measured specific conductance is higher than the calculated specific conductance, negative charge balance indicates a deficiency of cations, whereas positive charge balance indicates a deficiency of anions (Table 7). If the measured specific conductance is lower than the calculated specific conductance, negative charge balance indicates a surplus of anions, whereas positive charge balance indicates a surplus of cations. The difference between measured and calculated specific conductance as proposed by Rossum (1975) is utilized in WATEQ4F.

Table 7: Statements from accuracy checks of water analyses based on the calculations of the charge balance and a comparison of measured and calculated conductivity.

	Negative charge balance	Positive charge balance
Measured conductivity > calculated conductivity	Deficiency of cations	Deficiency of anions
Measured conductivity < calculated conductivity	Surplus of anions	Surplus of cations

The conductivities from the field measurement and those calculated after Rossum (1975) using the species distributions determined by PHREEQC are listed in the table in Appendix 4. The statement in Appendix 4, whether a surplus/deficit of anions/cations is detected in the solution, is not influenced by the sometimes high range of analysis (values in red > 10%) resulting from the calculated conductivities after Rossum (1975) and the measured conductivities. Only the fact which specific conductance is higher is considered. The statement depends on the percent-error of the calculated charge imbalance.

5.2.1.3 Charge Imbalance by WATEQ4F

A second method to check the accuracy of the analytical data is the specific charge imbalance determined by WATEQ4F. The input parameters used by WATEQ4F to compute the charge imbalance (“speciated CI” in the output file) and the specific conductance (“calculated conductivity” in the output file) differ slightly from the input parameters used by PHREEQC. The measured specific conductance, pH, temperature, E_H , Al, As(tot), As(III), As(V), B, Br, Ca, Cl, Cu, F, Fe(tot), Fe(II), Fe(III), HCO_3^- , H_2S , K, Li, Mg, Na, NO_3^- , SiO_2 , SO_4^{2-} , Sr, and Zn were the considered input parameters. The varying input parameters compared to PHREEQC are: (1) the measured specific conductance instead of no specific conductance, (2) E_H instead of pe, (3) additional to the species concentration: total As and total Fe, (4) alkalinity (HCO_3^-) instead of TIC (entered as C(IV)). While using the laboratory pH values to calculate the charge imbalance, all 18 samples showed a lower error compared to the field pH. Even better results were achieved with the adapted pH values from the PHREEQC modeling (see above 5.2.1.1).

In a first run of WATEQ4F, the adapted pH values were used. Three samples showed errors < 5%, six samples show errors between 5-10%, and seven samples showed a poor charge imbalance with errors > 10%. The maximum analytical error was found to be 25%. The samples that presented the higher analytical errors were not identical to those with the large drift between field and laboratory pH.

A second iteration of WATEQ4F used a revised data set where all raw data were revised again. The data from the ICP-AES and the IC were revised carefully with special interest on the major anions and cations as the major anions (and cations) influence most the specific conductance. From double determinations in different dilutions, the value with the better fit for the analytical error and the lower range of analysis (idem standard deviation) between measured and calculated specific conductance was selected. For seven samples,

the different dilutions did not agree very well with each other. For seven samples Na concentrations were corrected, for two samples SO_4^{2-} , and HCO_3^- for one sample. All changes are documented in the Access database. After a second run of WATEQ4F, nine samples had a charge imbalance $< 2\%$, four samples $< 5\%$, and five samples showed errors $> 5\%$ with a maximum analytical error of $+12.6\%$. (WNCTA01).

Table 8: The percent-error for the charge imbalances from the WATEQ4F and the PHREEQC determination is displayed. Revised data was used. If the analytical error for both calculations is $< \pm 2\%$, the comment is "o.k.". If the charge imbalance is $> \pm 2\%$, the conductivities are checked according to Table 7 and the corresponding comment is entered. If the charge imbalances are from opposite signs (positive and negative) they don't agree. According to Table 7 no statement is possible.

Sample ID	WATEQ4F %- error Charge imbalance	PHREEQC %- error Charge imbalance	Comment
WNCTA01	12.6	-0.7	no agreement
WNCTA02	3.2	-1.7	no agreement
WNCTA03	-1.5	-4.1	deficit of cations
WNCTA04	4.4	1.8	deficit of anions
WNCTA05	-1.0	-0.5	o.k.
WNCTA06	-1.1	-0.6	o.k.
WNCTA07	0.3	0.2	o.k.
WNCTA08	-0.5	-0.3	o.k.
WNCTA09	-0.3	-0.2	o.k.
WNCTA10	1.2	0.6	o.k.
WNCTA11	-0.9	-0.5	o.k.
WNCTA12	-6.3	-5.5	deficit of cations
WNCTA13	3.2	1.3	o.k.
WNCTA14	9.4	-5.0	no agreement
WNCTA15	10.4	-5.5	no agreement
WNCTA16	8.9	-4.3	no agreement
WNCTA17	-1.1	-1.5	deficit of cations
WNCTA18	-3.3	-12.5	deficit of cations

Conductivities determined in the field were in general elevated compared to the calculated ones. Sample WNCTA01 showed an error of $+12.6\%$ for the charge imbalance determined by WATEQ4F. As the pH drifted between 5.6 (field) and 6.2 (laboratory), the pH would not alter significantly the charge balance by H^+ -ions.

5.2.2 Iron Species Check

The concentrations of Fe species were compared as determined by on-site photometry and ICP-AES. Due to different sensitivities of the analytical devices, only Fe concentrations > 0.2 mg/L were considered for the range of analysis. The overall range of analysis for nine Fe measurements is 18.9% . Two samples (WNCTA08 and WNCTA09) present significant discrepancies in their Fe determinations. Both samples are characterized by elevated Fe(III)

concentrations, detected with the photometer; an average R.O.A. of about 75% is the consequence. While disregarding these two samples, the overall R.O.A. is 2.4%. In general, Fe(II) is the predominating iron species (14 out of 18 samples). On-site determinations were taken for all further modeling, because they contain species information on Fe(II)/Fe(III).

5.2.3 Arsenic Species Check

The total As concentrations determined by ICP-AES and HG-AAS, as well as the total As concentrations determined as sum from the species determination by HPLC-ICP-MS and from the elution of the ion exchangers are represented in Table 9. Only five samples from the West Nymph Creek Thermal Area showed arsenic concentrations above detection limit for all the techniques. Therefore, eight additional samples from surrounding areas were considered for statistical comparison of the speciation techniques. These samples have been analyzed together with the samples from West Nymph Creek. Details on the sample locations are given in Planer-Friedrich (2004). The sample code is the following: YNP = Yellowstone National Park, RH = Ragged Hill, NL = Nymph Lake and HL = Hazle Lake. In the tables presented below it will be indicated (*) if these additional samples have been considered.

Table 9: Total arsenic concentrations for selected samples in µg/L, determined by the different detection methods. Only samples with As concentrations > detection limit were considered. For HPLC-ICP-MS and GF-AAS the sum from the four As species was taken. X = ion exchanger, aa = acetic acid conditioned, HCl = HCl conditioned. Missing values are represented by the expression -999. Detection limit is abbreviated by D.L.

Sample ID	As(tot) ICP-AES (µg/L) D.L. 50 µg/L (a)	As(tot) HG-AAS (µg/L) D.L. 0.5 µg/L	As(tot) HPLC-ICP-MS (µg/L) D.L. 0.3µg/L	As(tot) µg/L X aa GF-AAS D.L. 3 µg/L	As(tot) µg/L X HCl GF-AAS D.L. 3 µg/L
WNCTA14	559	532	588	482	454
WNCTA15	1820	1790	1869	686	704
WNCTA16	1280	1460	1767	983	841
WNCTA17	1290	1423	1542	-999	819
WNCTA18	427	437	508	-999	388
*YNPHL01	307	118	156	-999	281
*YNPNL07	1660	1168	1290	-999	-999
*YNPRH04	1420	1851	1812	-999	1875
*YNPRH10	1290	1542	1563	-999	1581
*YNPRH18	352	300	315	-999	296
*YNPRH29	4670	4523	4562	-999	4668
*YNPRH30	4530	4248	4450	-999	3926
*YNPRH31	2460	2305	2633	-999	2573

(a) the actual detection limit of the ICP-AES is 50 µg/L. Because of possible interferences and known inaccuracies, a D.L. of 100 µg/L is considered.

With statistical methods (e.g. correlation) the degree of statistical coherency between two parameters can be determined. All the variables from the analysis are independent, non-paired and non-normal variables. To check the five variables of the total As for their correlation, the SPEARMAN-correlation coefficient was determined with the statistical software SPSS © 13.0 for Windows.

Table 10 presents the correlations for total arsenic determinations. Normally treated as 0.3*detection limit, the values below detection are not considered for the correlation analysis, neither for the range of analysis check (Table 11). Almost all variables show an expected positive correlation on a significance level of 99% (¹). The poor correlation coefficient for the acetic acid conditioned ion-exchangers results from missing values.

Table 10: Two-tailed Spearman correlation coefficients for total As determinations by ICP-AES, HG-AAS, HPLC-ICP-MS, and elution of the ion exchangers (X).

Correlations					
	As(tot) AES	As(tot) HG AAS	As(tot) HPLC	As(tot) X aa	As(tot) X HCl
As(tot) AES	1.000				
As(tot) HG AAS	.924 ¹	1.000			
As(tot) HPLC	.927 ¹	.989 ¹	1.000		
As(tot) X aa	.500	.500	.500	1.000	
As(tot) X HCl	.918 ¹	.958 ¹	.923 ¹	1.000 ¹	1.000

1. Correlation is significant at the 0.01 level (2-tailed).

Considered samples: five WNCTA with total As concentrations > D.L. and additional eight samples from surrounding areas.

5.2.4 Description of the Analysis Results

5.2.4.1 Cl-As-Correlation in Geothermal Fluids

The positive correlation between As and Cl discussed in general in 2.2.5.1 was confirmed for all of the 26 samples (West Nymph Creek and surrounding areas) by bivariate correlation analysis on a significance level of 1%. The correlation analysis was done twice: first for all the samples, including those with As < D.L., and second, for all the samples presenting As concentrations > D.L. (Figure 36). The total As concentrations were taken from the HPLC-ICP-MS determination because these resulted in the highest R². The Cl-As-correlation using the As concentrations from the ICP-AES shows a similar result ($y = 5.9443x - 48.706$; $R^2 = 0.7286$).

The correlation analysis was performed as well with the total As concentrations from HG-AAS and from ion-exchangers, never resulting in a better residuum ($R^2 > 0.79$).

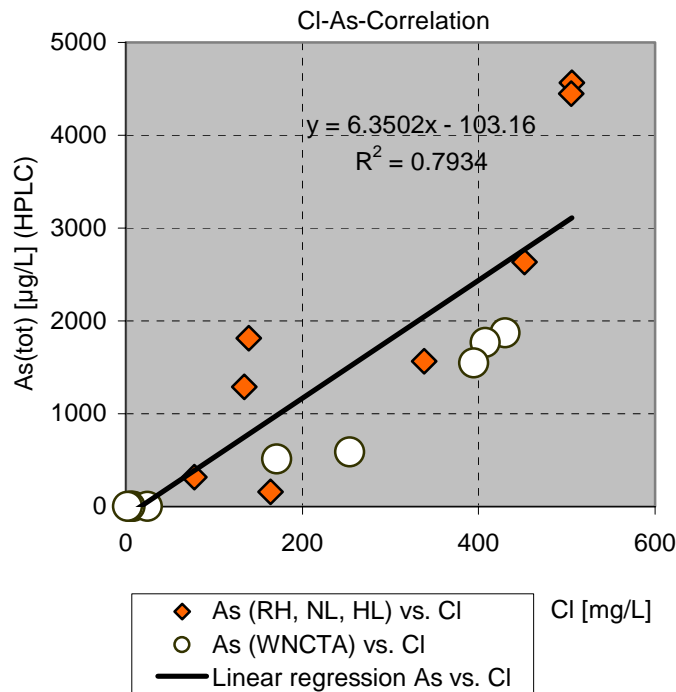


Figure 36: Positive correlation and significant trend of As and Cl concentrations due to similar behavior during steam-water separation. Considered samples: 18 samples with total As concentration > D.L. (10 samples from WNCTA (white dot) and 8 samples from surrounding areas (orange square). RH = Ragged Hill, NL = Nymph Lake, HL = Hazle Lake.

The correlation agrees with the findings from Stauffer and Thompson (1984) who checked 268 thermal springs in Yellowstone National Park for their Cl-As-correlation. Chloride was found to be the principal geochemical correlate of As in all explored high temperature igneous systems. If As behaves conservatively during fluid migration any combination of adiabatic cooling and dilution by Cl and As-free meteoric water results in points lying along the linear line. Points with reduced Cl levels, which lie significantly below the linear line, indicate either losses of solute As accompanying cooling, or mixture with another source water with higher Cl/As ratio. Conversely, when points lie significantly above the linear line, an additional As source is indicated, either by mineral dissolution or mixing with another high-As source water.

5.2.4.2 Comparing HG-AAS to HPLC-ICP-MS

Only five from the eighteen water samples from the West Nymph Creek Thermal Area present significant elevated As concentration. To allow a comparison between the different methods, additional eight samples from Yellowstone were considered. These samples originate from different locations in Yellowstone. Details on the sample locations are given in Planer-Friedrich (2004). In the tables presented below it will be indicated if these

additional samples have been considered. The range of analysis between the different analytical techniques was determined (Table 11).

Table 11: (*) Range of analysis for the total arsenic determination done by ICP-AES, HG-AAS, HPLC-ICP-MS, and elution of the ion exchangers (X) (aa = acetic acid conditioned). Values below detection limit were not considered.

Range of Analysis [%]					
	As(tot) AES (µg/L)	As(tot) HG AAS (µg/L)	As(tot) HPLC (µg/L)	As(tot) X aa (µg/L)	As(tot) X HCl (µg/L)
As(tot) AES (µg/L)	-	3.2 ¹	7.5 ¹	21.9 ¹	20.5 ¹
As(tot) HG AAS (µg/L)	30.6	-	5.7 ¹	23.0 ¹	22.2 ¹
As(tot) HPLC (µg/L)	33.7	5.7	-	28.3 ¹	27.5 ¹
As(tot) X aa (µg/L)	4.0	66.2	66.5	-	4.0 ¹
As(tot) X HCl (µg/L)	45.5	56.2	57.1	29.7	-

1. R.O.A. [%] exclusively determined for As(tot) >100µg/L

(*) only the WNCTA samples were considered

The total As from the HG-AAS compared to the total As from the HPLC-ICP-MS have a range of analysis (R.O.A.) of 5.7% if only the WNCTA samples were considered. If the additional eight samples were considered, the R.O.A. is lowered to 4.6%. One should be aware of, that the determination of the R.O.A. is extremely sensitive toward variances of low concentrations. Two samples for example $x_1 = 1$ and $x_2 = 2$ show a discrepancy of 1, resulting in a R.O.A. of 0.5 (33.3%), whereas $x_3 = 1000$ and $x_4 = 1001$ have also a discrepancy of 1, resulting in a R.O.A. of 1 (0.0%). This characteristic of the R.O.A. is the reason why low concentrations (below detection limit) were not considered in the following comparisons of the analytical methods.

The high ranges of analysis in the first column of Table 11, assuming inaccurate analytics, are mainly due to three As determinations from the ICP-AES, which were barely detected with any other method: 163 µg/L (ICP-AES) vs. 3.7 µg/L (average from all the other methods), 161 µg/L vs. 5.5µg/L, and 141 µg/L vs. 7.3 µg/L. These differences may result from probable matrix interferences during the multi element detection. Disregarding these three values, a R.O.A. of 3.2% with HG-AAS is possible. All ICP-AES samples have been determined in three dilutions (1:2, 1:10, and 1:50) in order to choose the best fitting value within the range of detection. No reason for these discrepancies could be identified.

The accuracy for species separation (As(III) and total As) by hydride generation is strongly pH dependent. With HG-AAS speciation technique, all the dissolved As species (inorganic and organic) may be detected as total As or only the As(III) fraction may be detected. Discussed in detail in 4.2.1, the Figure 22 reveals that at $\text{pH} < 5$ fractions of pentavalent As species (mainly DMA^{V}) are reduced and transformed to arsine, and erroneously detected as As(III). Thus the detected As(III) fraction is expected to be elevated to the disadvantage of the As(V) fraction, determined from the difference of the total As and the As(III)

concentrations. The assumption that the differences between the two methods would increase with decreasing pH was rejected, as the natural pH has no influence on the hydride generation itself. All the samples have been acidified to the same pH prior to analysis. Losses of As(V) due to low pH affect all the samples in the same way. To find out, whether or not the mono- and dimethylated species contribute to the As(III) concentration, species from HG-AAS were compared to species from HPLC-ICP-MS.

Furthermore, the As(V) fraction determined by HG-AAS is expected to exceed the As(V) fraction determined by HPLC-ICP-MS. Reason for this assumption is that all the methylated species (except the losses of DMA^VA) will contribute to the As(V) fraction. Thus, the As(V) concentrations from the HG-AAS are assumed to equal the sum of As(V), DMA^VA, and MMA^VA from the HPLC-ICP-MS. The following trends are expected:

- 1) As(III) from HG-AAS > As(III) from HPLC-ICP-MS
- 2) As(V) from HG-AAS >> As(V) from HPLC-ICP-MS
- 3) As(V) from HG-AAS \approx As(V) + DMA + MMA from HPLC-ICP-MS

1) The expectation was confirmed. The As(III) concentrations from the HG-AAS are elevated on average by 13.6% in comparison to the As(III) concentrations from the HPLC-ICP-MS (Table 12). Reason for this might be that some of the pentavalent methylated As fraction is determined erroneously as As(III). The samples 1 to 13 have at least one value below detection limit and need not be considered in the comparison.

Table 12: As(III) concentrations determined by HG-AAS and HPLC-ICP-MS. For the samples 1 to 13, at least one of the two As(III) determinations was below detection limit. D.L. = detection limit. R.O.A. = range of analysis.

Sample ID	Field pH	As(III) HG-AAS D.L. 1 µg/L	As(III) HPLC-ICP- MS D.L. 0.3µg/L	R.O.A. [%]
WNCTA14	6.4	532	275	31.9
WNCTA15	7.2	1579	973	23.8
WNCTA16	7.1	417	380	4.6
WNCTA17	6.4	234	203	7.1
WNCTA18	5.9	107	77	16.3
YNPHL01*	3.0	74	40	29.5
YNPNL07*	2.5	1079	574	30.5
YNPRH04*	1.8	136	112	10.0
YNPRH10*	3.0	1074	1033	1.9
YNPRH18*	2.2	123	125	0.7
YNPRH29*	2.6	1049	993	2.7
YNPRH30*	2.6	3074	2748	5.6
YNPRH31*	2.7	2721	2132	12.1

(*) eight additional measurements were considered for comparison of analytical methods

As the hydride generation for As(III) determination was performed at a pH of 1 to 2, Figure 22 reveals that the complete DMA^VA fraction and almost 50% of the MMA^VA fraction is reduced to arsine and contribute to a significant overestimation of the As(III) fraction. The choice of such a low pH for As(III) determination may be due to the fact that the methylated As fraction was either underestimated or not considered by USGS.

2) The expected trend was not confirmed. In contrast, the As(V) concentrations from the HG-AAS are lowered on average by 12.3% in comparison to the As(V) concentrations from the HPLC-ICP-MS (Appendix 3). The samples 1 to 13 have at least one value below detection limit and need not be considered in the comparison. The two samples WNCTA14 and YNPRH31 showed As(V) concentration below detection limit while determined by HG-AAS, whereas the HPLC-ICP-MS detects an As(V) concentration of 301 µg/L, respectively 115 µg/L. Nevertheless, the samples were determined twice (at two different dilutions) in both, the HG-AAS and the HPLC-ICP-MS. No agreement was realized. If the samples were disregarded, the average R.O.A. is 19.9%.

The general lowered As(V) by HG-AAS results from the loss of fractions of methylated As(V) species at the pH of 1 - 2 of the hydride generation process. These fractions were thus erroneously detected as As(III). Individual samples show a methylated As fraction (DMAA and MMAA) up to 38% of the total As. In general the methylated As fraction makes up 10.2% of the total As.

3) The assumed correspondence was not observed. Even As(V) from HG-AAS << sum pentavalent As species from HPLC-ICP-MS. If the samples with a response below detection limit are not considered, furthermore the samples WNCTA14 and YNPRH31 are disregarded because of discrepancies of the values, the concentrations of the As(V) by HG-AAS are significantly lower than the overall sum of As(V), DMAA, and MMAA from the HPLC-ICP-MS. The sum of the pentavalent As fraction from the HPLC-ICP-MS is in general 22.5% higher than the As(V) by HG-AAS (Appendix 2).

Reason might be the mentioned volatilization of the methylated species to arsine at a pH about 2, and thus the erroneously determined as As(III).

5.2.4.3 Ion exchangers: Acetic acid vs. Hydrochloric acid Conditioning

A combined set of commercial cation and anion exchangers was used to separate on site As(III), As(V), MMA, and DMA. For details of the field application and the conditioning, refer to 4.3.3 On-site Arsenic Species Separation. The respective arsenic concentrations recovered from the acetic acid conditioned exchangers and from the hydrochloric acid conditioned exchangers are shown in the following figures: As(III) in Figure 37, As(V) in Appendix 5, MMAA in Appendix 6, and DMAA in Appendix 7. Bednar et al (2002, 2004) found better species recoveries while using acetic acid conditioned exchangers, furthermore longtime stability and buffering capacity were improved. In case of a better response of the

acetic acid conditioned ion exchangers, the linear regression line would be located below the line of equal relation ($X=Y$ -line), presenting a gradient < 1 .

For As(III) the response of the acetic acid conditioned exchangers was not improved compared the chloride form (Figure 37).

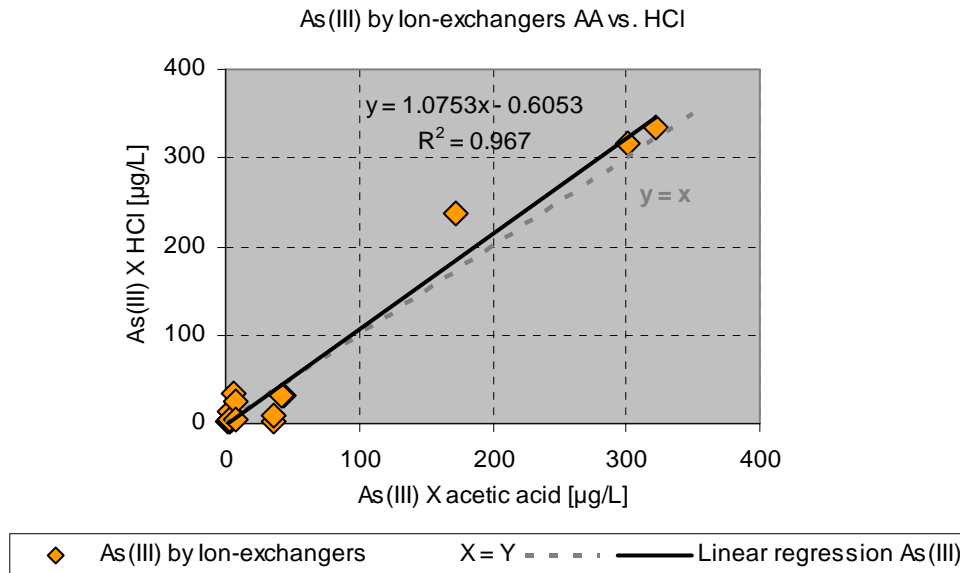


Figure 37: Linear regression analysis of HCl conditioned ion exchangers (Y-axis) and a.a. conditioned ion exchangers (X-axis) for As(III). As the gradient of the regression line is slightly > 1 , the response for the a.a. conditioned exchangers was not improved.

For As(V) one determination from an HCl conditioned exchanger shows a low response and is identified as main reason for the gradient < 1 (Appendix 5). The low concentration does not agree with As(V) determinations by HPLC-ICP-MS, neither HG-AAS. In general, no improvement of the acetic acid form was detected compared to the chloride form. Neglecting this one value, a R^2 of 0.94 for the regression line was determined.

The concentrations of the methylated As species eluted from both types of ion exchangers agree quite well with each other. Unfortunately, only four samples presented both: elevated As concentrations and were determined by acetic acid conditioned exchangers. The regression line for MMAA is shown in Appendix 6. Again only one value is responsible for the gradient < 1 ; neglecting this value, a regression line of about one was determined. The regression line for DMAA, with a gradient of about one, is shown in Appendix 7.

There was no significant difference in species recovery for the acetic acid conditioned ion exchangers compared to the hydrochloric acid conditioned exchangers could be determined. One reason for the correspondence of the concentrations from the different conditioned ion exchangers might be that the method presented by Bednar et al. (2004) was designed for waters with a low pH (< 4) e.g. acid mine drainage. The Yellowstone samples present a

variance in pH ranging from < 2 to > 7 ; however, the samples with elevated arsenic concentrations have a pH varying from 6 to 7 and thus are not affected by low pH.

5.2.4.4 Species determination: Ion exchangers vs. HPLC-ICP-MS

To compare both species determination methods, the species concentrations from the ion exchanger were displayed against those determined by HPLC-ICP-MS. The series from the HCl conditioned ion exchangers were taken because of their completeness of the data series. The series for the acetic acid conditioned exchangers comprise only 16 measurements (instead of 18 for X HCl). Only the samples with relative species concentrations above detection limit were considered. Furthermore, additional 7 samples where ion exchangers were applied were considered for the comparison of the methods. Details on these sample locations are given in Planer-Friedrich (2004).

A linear regression analysis of HPLC-ICP-MS and HCl conditioned ion exchangers was done for all the species. The different responses resulting in different gradients of the regression line might be due to the pH dependent species separation on the ion exchangers. If higher concentrations of the considered species are found on the ion exchanger (better response), the linear regression line would be located above the line of equal relation (X=Y-line), presenting a gradient > 1 .

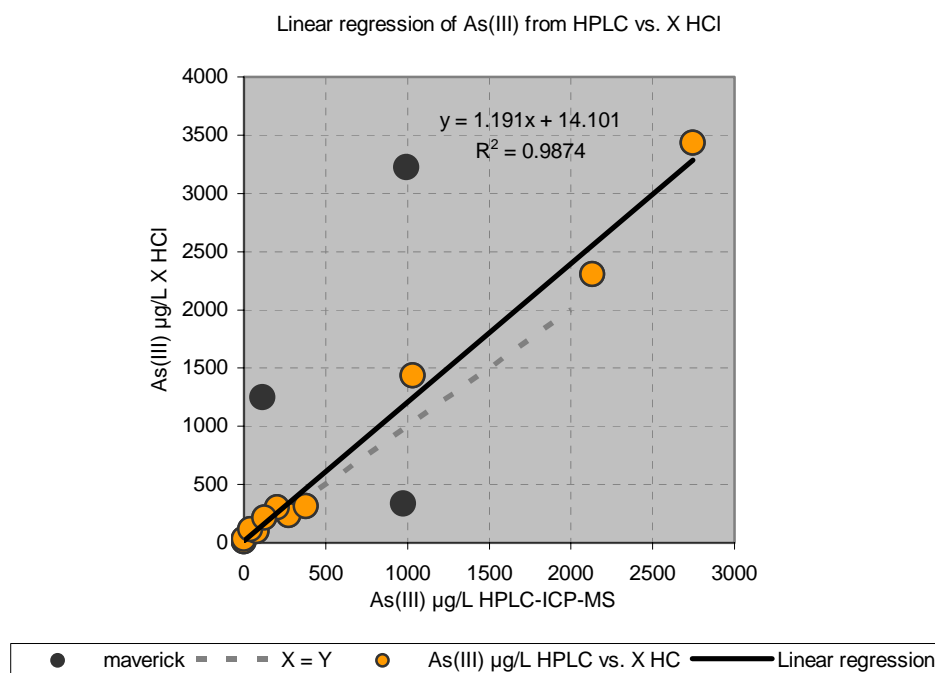


Figure 38: Linear regression analysis of HCl conditioned ion exchangers (Y-axis) and HPLC-ICP-MS measurements (X-axis) for As(III). The gradient of the regression line is slightly > 1 , the response of the ion exchangers might be slightly better.

The linear regression analysis for As(III) concentrations reveals an almost linear regression line. The response of the HPLC-ICP-MS measurement compared to the eluted ion

exchangers is similar (Figure 38). Three outliers were not considered for the regression line, thus resulting in a $R^2 = 0.99$. The outliers would have pretended a better response of the ion exchangers.

The figure in Appendix 8 displays the linear regression line of As(V) from HPLC-ICP-MS and ion exchangers. The extreme low gradient of 0.05 reveals a poor As(V) recovery from the HCl conditioned ion exchangers (idem for a.a. conditioned exchangers).

The comparison of MMAA from the ion exchangers and MMAA determined by HPLC-ICP-MS shows almost no trend (Appendix 9). The quality of the regression line is poor ($R^2 = 0.19$). In general, both methylated As species (MMAA and DMAA) show elevated concentrations while recovered from the ion exchangers. The comparison of the DMAA concentrations reveals a better recovery from the ion exchangers. This observation is confirmed by a gradient > 1 of the regression line (Appendix 10).

The total As concentrations determined by the ion exchangers show a poor agreement with the other total As determinations; however the total As by HPLC-ICP-MS agree well with the total As by ICP-AES and HG-AAS (Table 11). The quantitation of the HPLC-ICP-MS measurements was done with the software program Graphical Analysis® to calculate the area under the chromatographic peaks. When a rather small peak of DMAA succeeds immediately a high peak of As(III) and a rather small peak of MMAA proceeds a high peak of As(V), distortions of the respective peaks should be considered (screenshot of the peaks Appendix 11). High peaks of inorganic As species are likely to hide (suppress) the smaller peaks of methylated As species what may result in the “better response” of the HPLC-ICP-MS determinations toward inorganic As species (Figure 38 and Appendix 8), while methylated As species remain undetected or underestimated.

For those samples where ICP-AES, HG-AAS, and HPLC-ICP-MS detected total As concentrations below detection limit, the elution of the ion exchangers resulted in total As concentrations of about 10 - 20 $\mu\text{g/L}$. These concentrations are likely to result from a single species determination with concentrations slightly above detection limit, added to the concentrations below detection limit, that are produced as $0.3 \cdot \text{detection limit}$. With a detection limit of 3 $\mu\text{g/L}$ for every species these values are explainable. Thus, these values need not be commented. The exception are two samples (WNCTA09 and WNCTA10) that presented total As concentrations of 30 $\mu\text{g/L}$ while determined with the HCl conditioned ion exchangers and about 40 $\mu\text{g/L}$ while determined with the acetic acid conditioned exchangers. With no other technique, these concentrations were detected. The detected species was in both cases As(III) in the run-through of the exchangers.

The conditioning of the exchangers prior to analysis excluded a contamination of the exchangers. Furthermore, the acids designated for conditioning were analyzed themselves and showed no contamination neither. Accidental contaminations in the field or in the laboratory are unlikely because only in the first elution run arsenic concentrations were

registered. The second elution run shows only As concentrations below detection limit (< 3 µg/L). At high concentrations the total As determinations from the ion exchangers are underestimated.

Where do the low As(V) concentrations from the ion exchangers result from?

The As speciation technique by ion exchanger is influenced by pH - below pH 4, part of the As(V) fraction occurs as non-charged species (Figure 17). This non-charged species passes the ion exchanger and is thus erroneously determined in the As(III) fraction. The fact that all the samples with elevated As concentrations presented a pH about 6 to 7 and the fact that As(V) predominates as negative charged species at this pH range demands another explanation. The low As(V) recoveries and the elevated MMAA concentrations may result from a co-elution of both single negative charged species from the anion exchanger (Figure 20). Thus some As(V) is determined erroneously as MMAA.

Furthermore the As(III) recoveries from the ion exchangers are too low. If only the samples with total As > 100 µg/L were considered, average deficits of As(III) of 3% and 27% compared to As(III) from HPLC-ICP-MS and HG-AAS respectively were detected. Individual samples show a deficit of As(III) up to 60%. A maximum deficit of 79% was detected for WNCTA15 when comparing As(III) from the acetic acid conditioned exchanger to the HG-AAS data. No reason for the poor total As recoveries from the exchangers could be identified.

Table 13: Percent [%] distribution of the As species for selected samples. Values highlighted in red show bad agreement compared among each other. To compare the As(V) determination from the HG-AAS to the speciation methods, the sum of the pentavalent species (As(V), DMA^VA and MMA^VA) is given.

	Field pH	HG-AAS		HPLC-ICP-MS					Ion exchanger (HCl)				
		As(III)	As(V)	As(III)	As(V)	MMAA	DMAA	Σ As(V)	As(III)	As(V)	MMAA	DMAA	Σ As(V)
WNCTA14	6.44	100	0	47	51	1	2	53	52	7	34	7	48
WNCTA15	7.17	88	12	52	44	2	2	48	47	11	32	9	53
WNCTA16	7.12	29	71	22	69	9	1	78	38	20	37	5	62
WNCTA17	6.35	16	84	13	86	1	1	87	37	21	37	5	63
WNCTA18	5.92	25	75	15	76	8	1	85	26	28	42	4	74
YNPHL01	3.04	63	37	26	36	1	37	74	42	0	16	42	58
YNPRH10	2.99	70	30	66	26	6	2	34	91	1	4	5	9
YNPRH18	2.15	41	59	40	31	28	2	60	73	8	17	2	27
YNPRH29	2.55	23	77	22	77	0	1	78	69	5	14	12	31
YNPRH30	2.64	72	28	62	33	4	2	38	87	1	8	4	13
YNPRH31	2.73	100	0	81	4	9	6	19	90	1	6	3	10

Table 13 represents the relative distribution of the As species in percent [%] determined by the different methods. The As(III) species determined by ion exchangers are elevated (overestimated) in general for the disadvantage of the As(V) fraction. That might be the reason as well why the sum of the pentavalent As species (As(V), DMA^VA, and MMA^VA) shows disagreement (underestimated for the ion exchangers), especially for those samples with a low pH value. The MMAA fraction for the ion exchangers seems to be overestimated - reason might be that some of the As(V) fraction is eluted from the exchangers by the acetic acid, designated to elute the MMAA fraction in a first run.

In waters with a pH about 6 to 7, the single negatively charged species H₂AsO₄⁻ predominates for the As(V) fraction (see below 5.2.4.5). At pH values < 3 (additional samples) a share of the As(V) fraction is available as non-charged H₃AsO₄ species. Non-charged species pass the exchanger column without being absorbed, idem As(III) fraction, and contribute to an As(III) overestimation.

The limited ion exchange capacity of the cartridges was also considered as a theoretical explanation for the low recoveries from the exchangers. As the exchange capacity is 1.9 meq/mL, the limitation of the exchange capacity is not considered as reason.

5.2.4.5 Modeling As Species

Speciation modeling was done with PHREEQC using the database WATEQ4F. No thermodynamic data could be found for the organic As species MMAA and DMAA. Arsenic species concentrations from the HG-AAS and from the HPLC-ICP-MS determinations were used as input parameters for modeling. The species modeling was done for all samples from the West Nymph Creek Thermal Area, presenting either As(III) or As(V) concentrations above detection limit. As the modeling process did not consider the organic species, the determined organic species were added according to their most probable redox state +5 to inorganic As(V) and referred as sum. The concentration and distribution of the thus-modeled As(III) and As(V) species were referred to the actual concentrations determined by species-selective sampling.

While using the HG-AAS concentration determinations as input (As(III) and As(V)), a predominance of As(V) species, making up to 84%, is registered for seven out of nine samples. This predominance of the As(V) species is confirmed by the measurements. The predominant pentavalent species is H₂AsO₄⁻ making up to 67% of the total dissolved arsenic. The second most abundant pentavalent species is HAsO₄²⁻ with a maximum of 34%. These findings are not in accordance with other reports on geothermal As (Webster and Nordstrom 2003) where As(III) species are predominant. Only for two samples, the trivalent H₃AsO₃ was the predominant As species. The second most abundant trivalent As species is H₂AsO₃⁻ with up to 10%. The species predominance in dependence of the samples' pH is shown in Figure 17 and Figure 18.

The accuracy of the modeling was checked with a second modeling using the As concentrations from the HPLC-ICP-MS with As(V) input as sum of DMAA, MMAA, and As(V). Six out of eleven considered samples present a predominance of trivalent As species, exclusively H_3AsO_3 , making up to 89% of the dissolved As. The predominance of the trivalent species is found for those samples presenting low total As concentrations (about detection limit). Samples with elevated total As concentrations present a predominance of As(V) species. The predominant pentavalent species are H_2AsO_4^- making up to 76% and as second most abundant pentavalent species HAsO_4^{2-} with a maximum of 63% of the total dissolved arsenic (Figure 39). Both methylated species, DMAA and MMAA, determined by HPLC-ICP-MS do not contribute more than 10% to the total dissolved arsenic. Only two samples (WNCTA16 and WNCTA18) have a methylated fraction of about 10%. All other samples present a methylated fraction $< 4\%$.

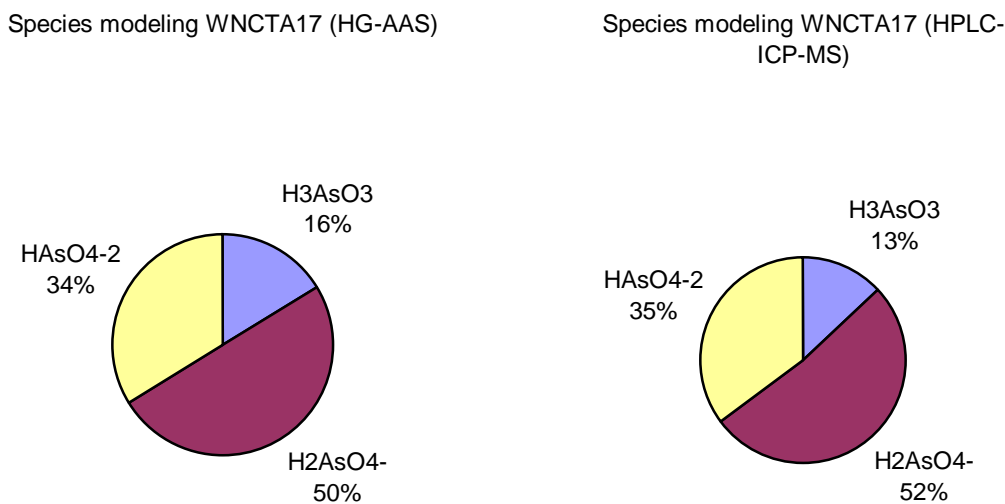


Figure 39: Arsenic species modeling done with HG-AAS input data (left) and HPLC-ICP-MS input data (right) show good agreement for samples with elevated Total As concentrations. The pentavalent species H_2AsO_4^- and HAsO_4^{2-} are predominant. The methylated As fraction of WNCTA17 is about 1.3%.

5.3 Hydrogeology

5.3.1 Clustering the Water Samples

Hierarchical cluster analysis was performed with the statistical software SPSS © 13.0 for Windows. The analysis divided the 18 water samples into two major groups (Appendix 12).

This result was found with the cluster methods of Between-groups linkage, Within-groups linkage, Nearest neighbor, Furthest neighbor, Centroid clustering, Median clustering, and

Ward's method, using the measuring interval Squared Euclidean Distance. All data were transformed to ranges between 0 and 1.

The significance of the classification into two groups is checked with the non-parametric Mann-Whitney U test, used to compare two independent groups of sampled data. Significant differences between the variables of the two subgroups on a significance level of 1% (P-value ≤ 0.01) was found with the Mann-Whitney U test for the following variables: pH, Cl, F, Br, Mg, Na, Al, B, As(III), As(V), DMAA, and MMAA. On a significance level of 5% (P-value ≤ 0.05) the following variables show a significant difference: SO_4^{2-} , DOC, Fe(II), Li, Ba, and SiO_2 . No significant overall difference was found for the specific conductance, temperature, E_H , TIC, NO_3 , Ca, K, Fe(III), Mn, Cu, Zn, and Sr.

The most important physico-chemical parameters (on site parameters) for water classification schemes e.g. temperature, pH, specific conductance, and redox potential were checked in detail. The temperature of the type I waters has a mean of 43°C (range of 66); the type II waters have a mean of 58°C (range of 59). No significant difference for temperature between the two water types was detected. The pH of the two water groups showed a significant difference. Type I waters had a mean pH of 3.7 (range of 4.3) and the type II waters had a mean pH of about 6.6 (range of 1.8) (Figure 40).

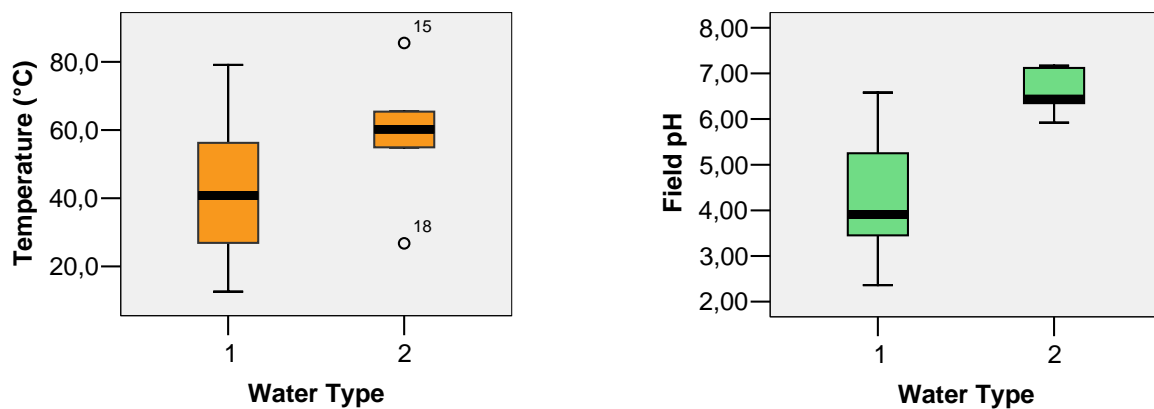


Figure 40: (left) No significant difference for the temperature between the two groups was detected. (right) The type I and the type II waters showed a significant difference for the pH.

The specific conductance and the redox potential are displayed in Appendix 14. Both parameters did not show a significant difference to allow a classification into one of two water types.

The two different groups correspond to the type I and type II waters discussed in section 2.2.5.1. The ternary diagram Cl- SO_4 - HCO_3 in Figure 41 (Giggenbach and Goguel 1989) shows their origin from heated steam (type I) or deep thermal sources (type II). Sulfate (SO_4^{2-}), one of the three classification parameters, shows a significant difference for the two groups on a significance level of 1.9%. If the three “peripheral influenced” samples were

considered as a group for their own (type III), the significance level of sulfate is 0.2%. The mean for sulfate for type I is about 300 mg/L (range of 766) and for type II 73 (range of 58) (Appendix 15).

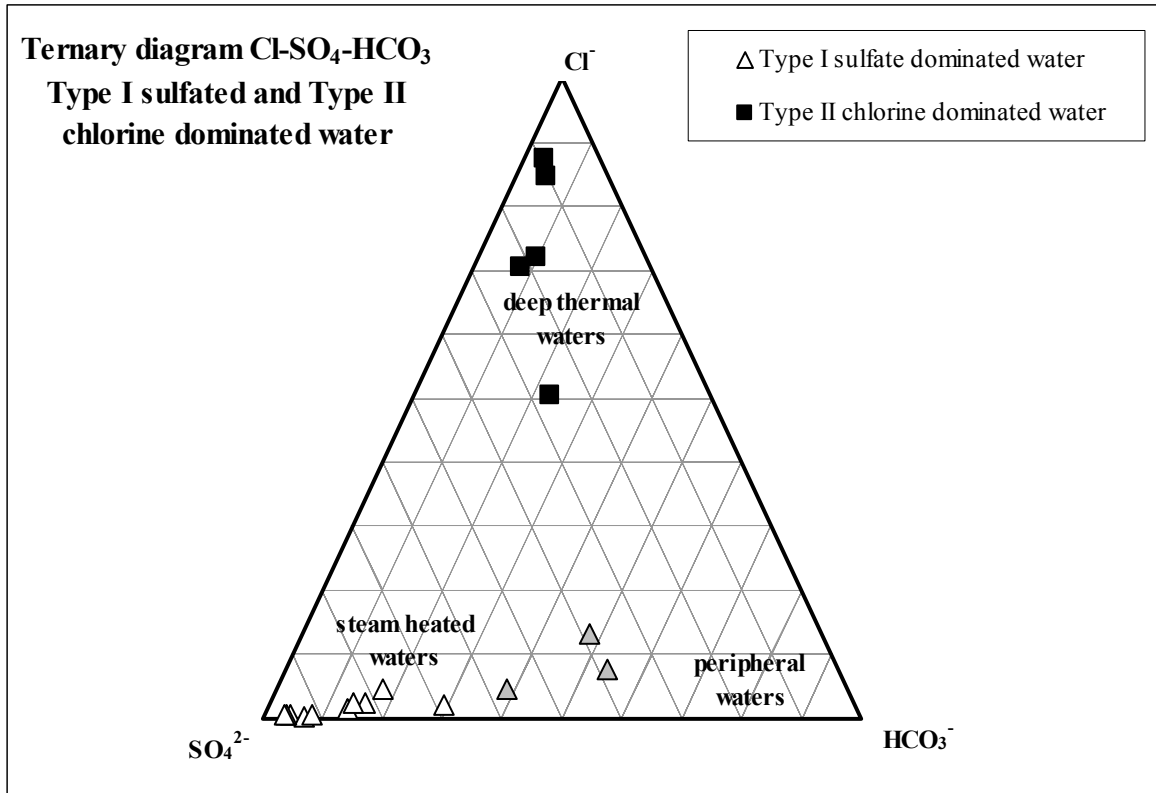


Figure 41: Ternary diagram Cl-SO₄-HCO₃ showing the origin of type I (sulfate dominated) waters from heated steam and type II (chlorine dominated) from deep thermal sources (after the classification scheme of Giggenbach and Goguel 1989). The ternary diagram confirms the classification into two groups defined by the cluster analysis.

The classification from the cluster analysis corresponds to the classification by the ternary diagram. The five samples from the southern part of the study area, closer to the Gibbon River and the Norris Geyser Basin correspond to the type II waters (chlorine and sodium dominated, deep thermal) (Figure 42). The thirteen samples of the central and the northern part of the study area correspond to the type I waters (sulfate dominated, steam heated), characteristic for Norris-Mammoth corridor waters. Peripheral waters influence three samples of the type II waters (highlighted in light grey: WNCTA01, WNCTA02, WNCTA03). The samples from the West Nymph Creek Thermal Area were displayed together with samples from surrounding area in a ternary diagram Cl-SO₄-HCO₃ (Appendix 13). Detailed explanations on the samples from the surrounding areas (Norris Geyser Basin, Nymph Lake, Hazle Lake) were given in Planer-Friedrich (2004).

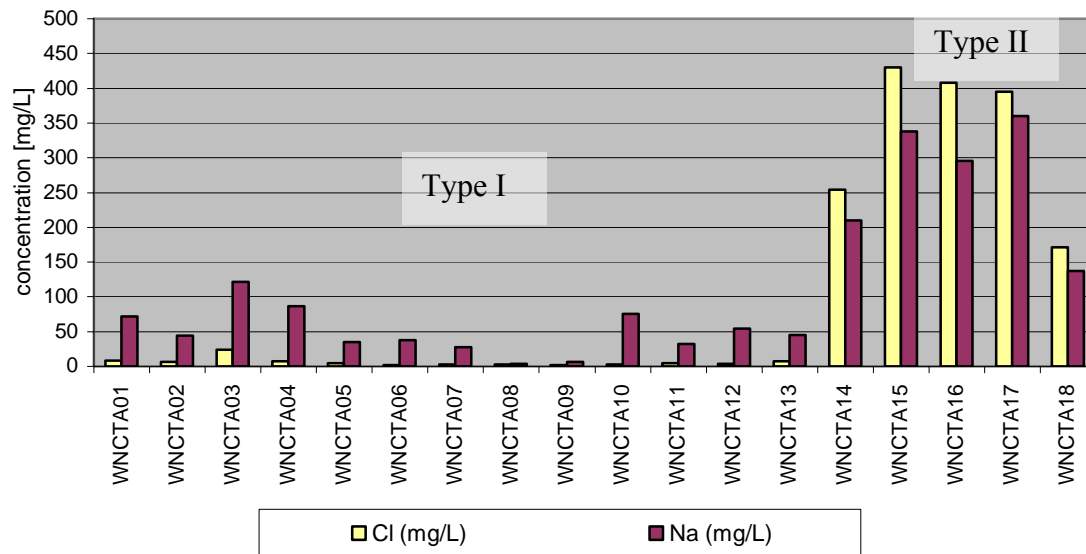


Figure 42: Significant difference for Cl and Na for the classification into two groups. Type I waters (steam heated) have low Cl and Na concentrations. Thus, type II waters (deep thermal) present elevated Cl and Na concentrations.

With the Si-geothermometer, the determination of the formation depth of a considered type of water is possible. In accordance with the Si-facies and the natural geothermal gradient, the formation depth can be determined. If the natural geothermal gradient is unknown or varies strongly (e.g. regions with geothermal activity), the formation depth cannot be determined. However, knowing which Si-modification (e.g. quartz, chalcedony, SiO₂ amorphous) predominates, the formation's temperature can be calculated. Species modeling with PHREEQC gives saturation indices for most of the minerals in solution. As quartz is oversaturated for all the samples, the quartz concentration is used to calculate the formation's temperature of the water.

$$T [^{\circ}C] = \frac{1032}{4.69 - \log SiO_2} - 273.15$$

The so-obtained formation temperature presents a significant difference for the classification into type I and type II waters on a significance level of 1.9% (Mann-Whitney U test). The outlier WNCTA06 for the type I water results from a cinder pool, explained in detail in 5.3.3. The calculated formation temperature may suggest a deep hot spring. The outlier WNCTA18 would rather fit into the type I group. This feature is located at the border of a wetland and is maybe altered by peripheral water. This dilution effect can also be observed for the sodium and chloride concentration (Figure 42).

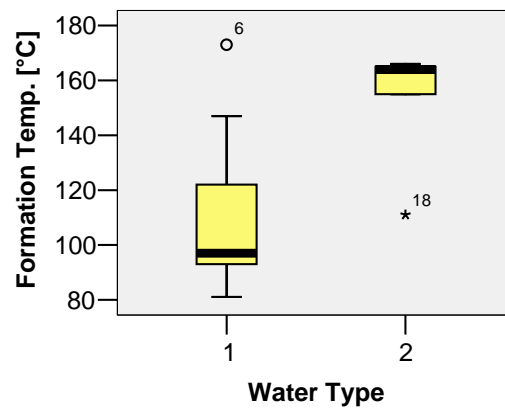


Figure 43: Calculated formation temperature of the water types according to the Si-geothermometer. The differences are significant (P -value = 0.02). The outlier WNCTA06 from type I is explained in detail in 5.3.3. According to the formation temperature, the outlier WNCTA18 would fit into the type I group.

5.3.2 Hydrogeological Model

The study area is located on the Norris-Mammoth corridor, near the intersection of two other major structures (Figure 3), the north wall of the Yellowstone caldera, and the Hebgen Lake fault to the west. One hydrogeologic model for the Norris-Mammoth corridor and the Norris Geyser Basin is proposed by White et al. (1988) and is illustrated in Figure 8 (refer to 2.2.5.1). The Norris-Mammoth corridor probably formed as a down faulted sag in the caldera's rim during the third-cycle Lava Creek tuffs. More than 350 m of ash-flow tuff are protected and preserved in this down dropped fault system. Chemical geothermometers indicate that geothermal waters at the base of the tuff have temperatures of $\sim 270^{\circ}\text{C}$ (White et al. 1988). The slightly adopted model is shown in Figure 44.

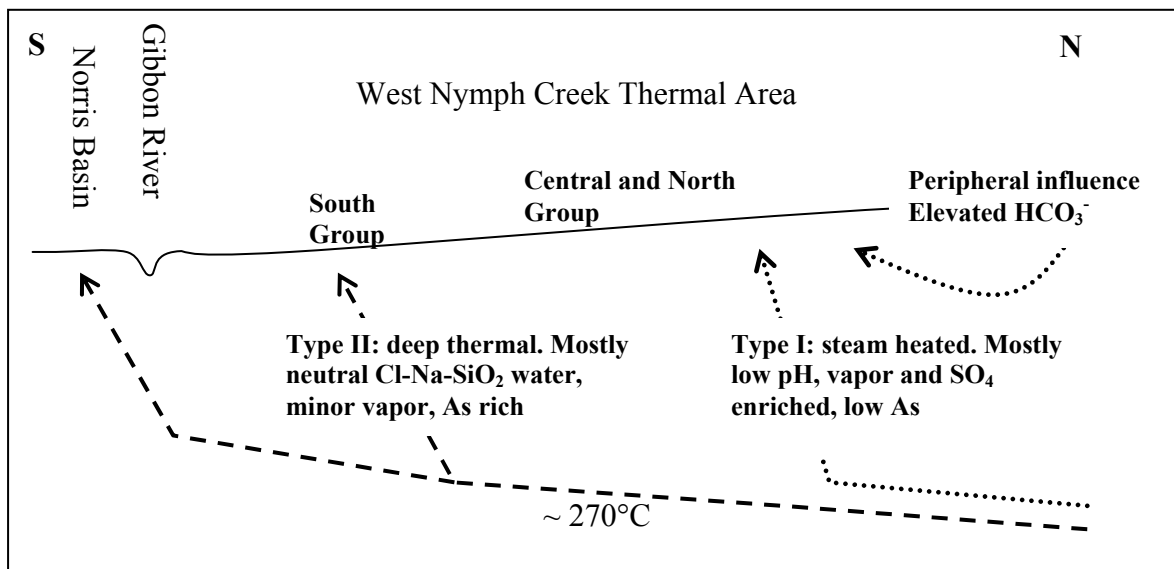


Figure 44: Schematic north-south section across the West Nymph Creek Thermal Area on the Norris-Mammoth corridor to explain the hydrogeologic situation. The existence of two water types was shown with a cluster analysis and verified with a significance test.

5.3.3 Remarkable Thermal Features

“Cinderella” (WNCTA06) is maybe the most interesting thermal feature of the study area. Located at the northwestern border of the study area, this surging hot spring measures about 50 to 30 meters in its extensions and contains milky-white to grey acid SO_4^{2-} -water at about 80°C . A tang of H_2S was characteristic for the site. During the period of the field trip, the border of this feature was covered by floating golden “cinders” almost spherical in shape and ranging from 2 mm to > 5 mm in diameter. A few “cinders” are nearly perfect spheres with hollow centers, but most of them present a broken surface (Figure 45). The thickest walls also contain dispersed small spherical cavities of various diameters, similar to the spherical gas cavities (vesicles) of some volcanic cinders and lava flows of fluid basaltic pahoehoe types.



Figure 45: Golden spherical “cinders” of “Cinderella” surging hot spring (WNCTA06). The size of the “cinders” varied from 2 mm to > 5 mm. Allen and Day (1935) identified similar black “cinders” in the Norris Geyser Basin as elemental sulfur.

Allen and Day (1935) were the first who identified Cinder Pool, a similar feature to “Cinderella”, in the western part of the Norris Geyser Basin. The black “cinders” of Cinder Pool were identified as elemental sulfur colored black by finely dispersed pyrite. The “cinders” with golden reflectance are made up of elemental sulfur. When dried, the “cinders” burn freely with a strong SO_2 odor.

The similarities of Cinder Pool and “Cinderella” in appearance allow to explain the mechanisms of this feature by referring to the investigations done by White and Leigh in (1969 and explained in White et al. (1988). Temperature-depth measurements at Cinder Pool revealed a constant temperature of 88 to 92°C extending to a depth of -19 m. At a depth of about -20 m, the temperature rose abruptly to 118°C and the temperature probe behaved as if suspended in a very viscous medium. Withdrawn from a depth of -21 m (119.5°C) the probe was completely encased in a black pitchlike substance that hardened and was later found to be elemental sulfur colored by dispersed iron sulfide.

The bottom of these “cinder” pools is likely to contain a pot of molten sulfur, overlain by a porous zone of congealed fragments of sulfur. In standard references, the melting point of orthorhombic sulfur is listed as 112.8°C, of monoclinic sulfur 119.0°C, and of elemental sulfur 120°C. At temperatures below melting points, molten sulfur can also be undercooled to a black rubbery substance (sulfur glass). For Cinder Pool in the Norris Geyser Basin, White et al. (1988) suggest a concealed “kettle” of seething, convecting molten sulfur at depths below about -19 m overlain by a ± 0.5 m thick sulfur sediment layer - probably particles similar to the floating “cinders” except with lower porosity and higher density. The sulfur sediment sealing is pierced intermittently by steams of rising gas bubbles that buoyantly carry molten sulfur into the cooler overlaying water-saturated porous zone of the layer. The gas probably exists in part as separate vapor bubbles, but may also be in solution in the molten sulfur. The hollow “cinders” might be interpreted in two ways: first as sulfur precipitated on gas bubbles, and second and more likely to be chilled blobs of molten sulfur containing dissolved gases that expand as long as the undercooled sulfur glass is sufficiently low in viscosity.

The only comparable occurrences of lakes containing molten sulfur pools above an active sub-aqueous fumarole are the Oyunuma Crater Lake of Noboribetsu in Japan, and at the Waiotapu in New Zealand (Lloyd 1959). The most critical requirements for the formation of molten sulfur and “cinders” are: (1) abundant supply of H₂S as basic source of reduced sulfur in geothermal areas; (2) at least 13 m of overlaying water is necessary to provide the pressure required for temperatures of 120°C to exist in a saturated water-steam system; (3) H₂S oxidizing to elemental sulfur as a major product, most simply by surface oxidation of an H₂S-rich convecting pool; and (4) low rate of discharge to avoid flushing and removal of newly formed “cinders”.

All the other thermal features are displayed and characterized in brief in numeric order in the Appendix 16 to Appendix 33.

6 Summary and Recommendations

In general, the combination of a helium balloon with a commercial digital camera turned out to be an appropriate method to realize high-resolution and cost-effective aerial survey.

Encountered problems were the lift capacities of the helium balloon, which diminished every day due to helium diffusion through the latex membrane. Furthermore, hot rising air with a lower density above large thermal features posed a problem. The helium balloon is extremely sensitive toward arising winds. Recommendations for future aerial survey campaigns are the use of lighter camera or a balloon with stronger lift capacity. The best lift capacities (100 m) during the mapping campaign in 2005 were reached with two interconnected helium balloons. A second advantage of the use of a balloon-couple is the safety aspect of the camera equipment. If one balloon bursts, the second balloon secures the camera from severe damage by crashing down. Connecting the two balloons with one single line is not recommended because the lower balloon will turn around the connecting line and twist the tether lines. The use of a light nylon net (e.g. net to protect fruit shrubs against birds) to integrate the two balloons is recommended. Attention should be paid while filling the balloon with helium: deflating helium from the valve might burn a hole in the latex membrane of the balloon. To keep the helium-filled balloon on site for two days or more a net or something similar could be used to fix it at the ground.

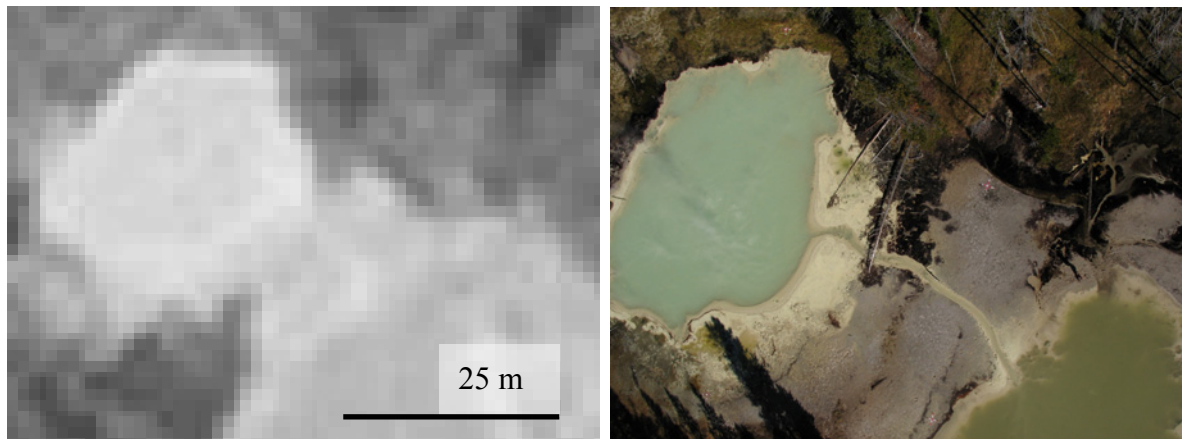


Figure 46: Traditional aerial image (left) with a raster cell size of 1 m in comparison to the high-resolution aerial images (right) with a raster cell size of 0.025 m.

A multi-layer GIS atlas merges the processed aerial pictures, the digitized features, thematic maps, and hydrochemical data. The on-site data from the ground survey, as well as the analytical results are attached to the atlas as databases. For this project, the accuracy of 0.5 m of the Trimble differential GPS was sufficient. Pictures taken from 100 m altitude show sufficient ground control points for georeferencing the pictures. The aerial survey

from the balloon resulted in a high-resolution aerial overview image. The raster cell size of the preexisting aerial images could be reduced from 1 m to a mosaicked cell size of 0.025 m in the digital atlas (Figure 46).

The hydrothermal waters were checked on reported high arsenic concentrations. Unfortunately the As concentrations in the study area were not that high and abundant than expected. From 18 samples, only about 5 samples showed significant elevated As concentrations in the range from 0.5 to 1.8 mg/L. For statistical evaluation of species distribution from the different analytical techniques, more samples with elevated concentrations were required. Therefore, additional 8 samples from different surrounding areas (details in Planer-Friedrich 2004) were taken into consideration. These samples have been analyzed together with the 18 samples from the West Nymph Creek Thermal Area. These samples presented As concentrations in the range from 0.3 to 4.7 mg/L.

Two methods for arsenic species separation were compared: on-site speciation by solid phase extraction (SPE) vs. species separation from preserved sample by high performance liquid chromatography (HPLC). Literature review let us presume that both methods would deliver similar results. However, the results are different. The determined As concentrations from the eluted ion exchangers are significant lower than those determined by HPLC-ICP-MS, ICP-AES, and HG-AAS. At low concentrations, the ion exchangers show a response where no other method shows any response - at elevated concentrations, a general deficit of the total arsenic is detected. One recommendation for future application of the ion exchangers is the use of standard solutions. Unfortunately the accuracy of the response of the ion exchangers could not be checked because the lack of applied standard solutions. The response of acetic acid conditioned exchangers was not significant better than that from the hydrochloric acid conditioned exchangers. A major disadvantage of the ion exchangers is the required time and the many possible errors one can make during conditioning, sampling, storage, (triple) elution, and analytics. Furthermore, the limited ion exchange capacity is a significant disadvantage when As concentrations are high and / or the specific conductance is elevated and charged dissolved ions compete for the exchanger places. To avoid these disadvantages, HPLC-ICP-MS is recommended for arsenic species determination. Attention should be paid for samples with elevated As(III) concentrations because this peak might hide / overlap a smaller DMA peak. Dilution of the sample might affect the DMA (and MMA) concentration to that extent that it drops below detection limit. A way to avoid the overlapping of two peaks would be the use of a longer column in the HPLC increasing the retention time for every species.

To do the As speciation for As(III) and As(V), without considering the methylated species, HG-AAS is recommended for samples with low concentrations of methylated As species. A major problem for this analysis technique is identified in the low pH at which the hydride generation for As(III) was done. Beside As(III), major fractions of DMA^VA and minor fractions of MMA^VA were volatilized as well, and erroneously determined as As(III).

Recommendation at this point should be the careful pH check at which the hydride generation for As(III) is performed.

The hydrogeological model of the Norris-Mammoth corridor (White et al. 1988) was checked for its applicability to the West Nymph Creek Thermal Area. The documented As/Cl correlation for hydrothermal waters from Yellowstone (Stauffer and Thompson 1981) was confirmed for the study area and its surrounding areas. The proposed grouping of the Yellowstone's hydrothermal waters (type I and type II) of the Norris Geyser Basin is applicable to the study area. Cluster analysis and the ternary diagram (Giggenbach and Goguel 1989) revealed two significantly different groups of water. The northern and central part of the study area are characterized by the type I waters; the southern area is characterized by the type II waters.

7 Acknowledgements

I would like to thank Prof. Broder Merkel, my first supervisor, who supported this work by professional suggestions how to present the results in the best way and by proofreading.

I am grateful to Dr. Britta Planer-Friedrich for giving me the opportunity to work out a diploma thesis abroad. She enabled all the important contacts to the National Park Service and the U. S. Geological Survey. Her engagement, experience in the field and the laboratory, as well as proofreading helped me much while working out this thesis.

During the work in the Yellowstone National Park, I relied on the help from the National Park Service. Therefore, I would like to thank Christie Hendrix and Shannon Savage in providing me GIS data, digital maps, and their support with the aerial survey permission. Furthermore, I appreciated the help of Steve Miller, GIS department of the National Park Service, for providing the differential GPS, giving instructions, and postprocessing the GIS data.

My acknowledgements go to the work group of Dr. Darrell Kirk Nordstrom from the U.S. Geological Survey (Boulder / USA) for their assistance in the field and providing the laboratory facilities. Special thanks go to Blaine R. McCleskey for his enduring help in the laboratory, his warm hospitality, and for his recommendations for data processing. Acknowledgement goes to Dr. James W. Ball for help with WATEQ4F.

An interesting and constructive part of my work was realized in the fascinating laboratory environment of the U. S. Geological Survey, Denver Federal Center (Denver / USA). Special thanks go to Dr. John Garbarino who enabled the analytical work on the HPLC-ICP-MS. His engagement, his help in data evaluation and proofreading as third supervisor helped me much.

I really appreciated the contact to all the members of the U. S. Geological Survey Staff in Boulder and Denver, answering my questions and providing more than scientific information.

The aerial mapping project was enabled by the creative work of Michael Sekul and his crew at the workshop of the TU Bergakademie Freiberg (Germany) constructing the custom-made carrier frame for the camera, as well as the handlebars. For laboratory assistance in Freiberg for the TIC/DOC determination, I want to thank Dipl. Chem. Hans-Joachim Peter.

Moreover, my special acknowledgments go to all-rounder Steve Dill from the Western Federal Lands Highway Division (USA) for his enduring help. Without him, the fieldwork wouldn't be done in this short time. Thanks to Juliane Becker from the TU Bergakademie

Freiberg in giving suggestions for the processing of the aerial photographs and for the GIS project.

Every work has to be financed and therefore I would like to thank the DAAD for their financial support.

Sincere thanks to my parents for financing my studies, my family and friends for the permanent encouragement during the difficult periods of my work. Thanks to Joy and my friends for their patience and their help to get some distraction from my work if it was necessary...

8 References

- Ball, J. W., McCleskey, R. B., Nordstrom, D. K., Holloway, J. M., Verplanck P. L. (2002): Water-Chemistry Data for Selected Springs, Geysers, and Streams in Yellowstone National Park, Wyoming, 1999-2000. U.S.G.S., Open-File Report 02-382
- Ball, J.W., Nordstrom, D.K., Jenne, E.A., and Vivit, D.V., (1998a): Chemical analyses of hot springs, pools, geysers, and surface waters from Yellowstone National Park, Wyoming, and vicinity, 1974-1975: U.S. Geological Survey Open-File Report 98-182, 45 p.
- Ball, J.W., Nordstrom, D.K., Cunningham, K.M., Schoonen, M.A.A., Xu, Y. and DeMonge, J. M., (1998): U.S. Geological Survey Open-File Report 98-574.
- Ball, J.W., and Nordstrom, D.K., (1991): User's manual for WATEQ4F, with revised thermodynamic data base and test cases for calculating speciation of major, trace, and redox elements in natural waters: U.S. Geological Survey Open-File Report 91-183, 189 p.
- Ballantyne J.M., Moore J.N. (1988): Arsenic geochemistry in geothermal systems. *Geochimica et Cosmochimica Acta*, Vol 52, p 475-483
- Becker, J. (2004): High resolution aerial and field mapping of thermal features in Ragged Hills, Yellowstone National Park; FOG Freiberg Online Geology, Vol. 11; ISSN 1434-7512. www.geo.tu-freiberg.de/fog/FOG_Vol_11_s.pdf
- Bednar, A.J., Garbarino J.R., Burkhardt M.R., Ranville J.F., Wildeman T.R. (2004): Field and laboratory arsenic speciation methods and their application to natural-water analysis. *Water Research*, Vol. 38, p. 355-364
- Bednar, A.J., Garbarino J.R., Ranville J.F., Wildeman T.R. (2002): Preserving the Distribution of Inorganic Arsenic Species in Groundwater and Acid Mine Drainage Samples. *Environ. Sci. Technol.* Vol. 36, No. 10, p. 2213-2218
- Bentley, R., Chasteen, T. G. (2002): Microbial Methylation of Metalloids: Arsenic, Antimony, and Bismuth. *Microbiology and Molecular Biology Reviews*, June 2002, Vol. 66, No. 2, p. 250-271
- Christiansen R. L. (2001a): Geologic map of the Yellowstone Plateau area in the Quaternary and Pliocene Yellowstone Plateau Volcanic Field of Wyoming, Idaho, and Montana. U.S.G.S. Professional Paper 729-G
- Christiansen R. L. (2001b): The Quaternary and Pliocene Yellowstone Plateau Volcanic Field of Wyoming, Idaho, and Montana. U.S.G.S. Professional Paper 729-G

- Cullen W. R., Reimer, K.J. (1989): Arsenic speciation in the environment. American Chemical Society. Chemical Reviews, Vol. 89, p. 713-764
- Dana P. H. (1997): Global Positioning System (GPS) - Time Dissemination for Real-Time Applications. Real-Time Systems, Vol. 12, p. 9-40
- Dzurisin, D., Wicks, C., Thatcher, W. (1999): Renewed uplift at the Yellowstone Caldera measured by levelling surveys and satellite radar interferometry. Bulletin Volcanology, Vol. 61, p. 349-355
- Ellis, A., Mahon, W. (1964): Natural hydrothermal system and experimental hot-water/rock interactions. Geochimica et Cosmochimica Acta, Vol. 28, p. 1323-1357
- Fritz, W. J. (2003): Roadside geology of the Yellowstone Country. 10th ed., Mountain Press Publishing Company, Missoula
- Garbarino J.R., Bednar A.J., Burkhardt M.R., (2002): Methods of Analysis by the U.S. Geological Survey - Arsenic speciation in Natural-Water Samples using laboratory and field methods. U.S. Geological Survey, Water-Resources Investigations Report 02-4144
- Gihring T.M., Druschel G.K., McCleskey R.B., Hamers R.J., Banfield J.F. (2001): Rapid Arsenite Oxidation by *Thermus aquaticus* and *Thermus thermophilus*: Field and Laboratory investigations. Environmental Science and Technology, Vol. 35, No.19, p. 3857-3862
- Haines, A. L. (1996): Yellowstone place names: mirrors of history. University Press of Colorado, p 11-16
- Hofmann-Wellenhof B., Lichtenegger H. (2001): GPS - Theory and Practice. Springer Wien - NewYork, 5th edition.
- Howard, A. G. (1997): (Boro)Hydride Techniques in Trace Element Speciation. Journal of Analytical Atomic Spectrometry, Vol. 12, p. 267-272
- Kharaka, Y.K., Mariner, R.H., Bullen, T.D., Kennedy, B.M., Sturchio, N.C., (1991): Geochemical investigations of hydraulic connections between the Corwin Springs Known Geothermal Resources Area and adjacent parts of Yellowstone National Park, in Sorey, M.L., ed., Effects of potential geothermal development in the Corwin Springs Known Geothermal Resources Area, Montana, on the thermal features of Yellowstone National Park: U.S. Geological Survey Water Resources Investigations Report 91-4052, p. F1-F38
- Kharaka, Y.K., Thordsen, J. J., White, L. D. (2002): Isotope and chemical Compositions of Meteoric and Thermal Waters and Snow from the Greater Yellowstone National Park Region, U.S. Geological Survey Menlo Park, California 2002, Open-File Report 02-194
- Kumaresan M., Riyazuddin, P. (2001): Overview of speciation chemistry of arsenic. Current Science, Vol. 80, No.7, p. 837-846

- Le X.C., Yalcin S., Ma M. (2000): Speciation of submicrogram per liter levels of arsenic in water: on-site species. American Chemical Society, Environ.Sci.Technol. Vol.34, No.11, p. 2342-2347
- Lewis A.J., Komninou A., Yardley B.W.D., Palmer M.R. (1998): Rare earth element speciation in geothermal fluids from Yellowstone National Park, Wyoming, USA. *Geochimica et Cosmochimica Acta*, Vol. 62, No. 4, p. 657-663
- Lloyd, E. F. (1959): The hot springs and hydrothermal eruptions of Waiotapu. *New Zealand Journal of Geology and Geophysics*, 2, p. 141-176
- McCleskey, R. B., Ball, J. W., Nordstrom, D. K., Holloway, J. M., Taylor, H. E. (2004): Water-Chemistry Data for Selected Springs, Geysers, and Streams in Yellowstone National Park, Wyoming, 2001-2002. U.S.G.S. Open-File Report 2004-1316
- McCleskey, R. B., Nordstrom D.K., Ball, J.W. (2001): Cation-exchange separation of interfering metals from acid mine waters for accurate determination of total arsenic and arsenic (III) by hydride generation - atomic absorption spectrometry. USGS Workshop on Arsenic in the Environment, February 21-22, 2001, Denver, CO. Extended Abstracts. (<http://wwwbrr.cr.usgs.gov/Arsenic/>)
- McCleskey, R. B., Nordstrom, D. K., Maest, A. S. (2004): Preservation of water samples for arsenic(III/V) determinations: an evaluation of the literature and new analytical results. *Applied Geochemistry*, Vol.19 (2004) p. 995-1009
- Mortimer, C. E., Müller, U. (1996): *Chemie - Das Basiswissen der Chemie*. Thieme Stuttgart, 6th edition, 752 pages
- National Park Service Water Resources Division (2001): Yellowstone National Park Small-Scale Base GIS Data. Fort Collins, CO
- Nordstrom, D.K. (2002): Worldwide Occurrences of Arsenic in Ground Water. *Science*, Vol. 296, p. 2143-2145
- Pergantis S.A., Winnik W., Heithmar E.M., Cullen W.R. (1997): Investigations of arsine-generating reactions using deuterium-labeled reagents and mass spectrometry. *Talanta*, Vol. 44, p. 1941-1947
- Pierce K. L., Morgan L. A., Saltus R. W. (2000): Yellowstone plume head: Postulated tectonic relations to the Vancouver slab, continental boundaries, and climate. U.S. Geological Survey, Open-File Report 00-498
- Planer-Friedrich B. (2004): Volatile Arsenic in Aquatic Environments. *Freiberger Forschungshefte Reihe Geowissenschaften C503*, Technische Universität Bergakademie Freiberg, 242
- Planer-Friedrich B., Matschullat J., Merkel B., Roewer G., Volke P. (2002): Development of a robust technique for sampling volatile metal(loid)s in wetlands. *Analytical and Bioanalytical Chemistry*, Vol. 374, No.7-8, p.1191-1198; Springer (ISSN 1618-2642)

- Rossum J. R. (1975): Checking the accuracy of water analysis through the use of conductivity. *Journal American Water Works Association* Vol. 67, p. 204-205.
- Rüde, T.R. (1996): Beiträge zur Geochemie des Arsens. *Karlsruher Geochemische Hefte*, 19, 206.
- Smedley P. L., Kinniburgh D. G. (2002): A review of the source, behaviour and distribution of arsenic in natural waters. *Applied Geochemistry*, Vol. 17, p. 517-568
- Smith, R. B., Siegel, L. J. (2000): *Windows into the Earth – The Geologic story of Yellowstone and Grand Teton National Park*. Oxford University Press, New York
- Stauffer R. E., Thompson J. M. (1984): Arsenic and antimony in geothermal waters of Yellowstone National Park, Wyoming, USA. *Geochimica et Cosmochimica Acta*, Vol. 48, p. 2547-2561
- Webster J. G., Nordstrom D. K. (2002): Geothermal Arsenic : The source transport and fate of arsenic from geothermal systems. *Arsenic in Ground Water*, A. H. Welch, K. G. Stollwerk, eds. Kluwer Academic Publishers, Boston, p.101-125
- White, D. E., Hutchinson, R. A., Keith, T. E. C. (1988): *The Geology and Remarkable Thermal Activity of Norris Geyser Basin, Yellowstone National Park, Wyoming*. U.S.G.S. Professional Paper 1456
- Whittlesey, L.H. (1995): *Wonderful Nomenclature: A history of the place names of Yellowstone National Park, being a description of and guidebook to its most important natural features together with appendices of related elements*. Helena, MT, Montana Historical Society Press, 867 p.
- Wicks, C., Jr., Thatcher, W., Dzurisin, D. (1998): Migration of Fluids beneath Yellowstone Caldera inferred from satellite radar interferometry. *Science* 282, p.458-462
- Xu, Y., Schoonen, M. A. A., Nordstrom, D. K., Cunningham, K. M., and Ball, J. W., (1998): Sulfur geochemistry of hydrothermal waters in Yellowstone National Park: Park: I. The origin of thiosulfate in hot spring waters: *Geochem. Cosmochem. Acta* 62, p. 3729-3743
- Yalcin, S., Le, C.X. (2001): Speciation of arsenic using solid phase extraction cartridges. *J. Environ. Monit.*, Vol.3, p. 81-85

Online references

- Analytical Spectrometry Research Group, University of Kentucky (2005).
<http://asrg.contactincontext.org/>
- Coury L. (1999): Conductance measurements, Part 1: Theory. *Current Separations.com*, 18:3
www.currentseparations.com/issues/18-3/cs18-3c.pdf.
- Garmin (2005): GPS 12. www.garmin.de

- Nordstrom, D.K., McCleskey, R.B. and Ball, J.W., (2001): U.S. Geological Survey Workshop on Arsenic in the Environment, Denver, CO, Feb. 21-22
<http://wwwbrr.cr.usgs.gov/Arsenic/FinalAbsPDF/nordstrom.pdf>
- Trimble (2005): product information, tutorials and customer support for GPS and DGPS.
www.trimble.com
- Merkel, B. (09.2005): Chair of hydrogeology, lectures, exercises.
http://www.geo.tu-freiberg.de/hydro/vorl_portal/Hydrogeo_uebungen_II/sat_positioning.htm
- U.S. Department of the Interior - U.S. Geological Survey (08.2005): GIS.
http://erg.usgs.gov/isb/pubs/gis_poster/index.html
- U.S. Naval Observatory (09.2005): USNO GPS Timing operations.
<http://tycho.usno.navy.mil/gps.html>

9 Appendix

Appendix 1: The accuracy of the dGPS determined ground control points is checked with the help of 24 tape measurements, performed on-site. The absolute difference between the calculated (GeoToolbox in TNTmips) and the measured (tape measurement) lengths is displayed. The mean deviation is 0.41 m (standard deviation 0.3 m). The mean range of analysis in percent is 0.9 %.

measured [m]	calculated [m]	abs diff. [m]	R.O.A. [%]
27.27	27.19	0.08	0.1
23.84	24.33	0.49	1.0
25.15	25.04	0.11	0.2
26.49	27.26	0.77	1.4
36.30	36.89	0.59	0.8
36.25	36.33	0.08	0.1
17.89	18.55	0.66	1.8
14.36	13.46	0.90	3.2
21.10	21.42	0.32	0.8
17.12	16.55	0.57	1.7
27.38	27.43	0.05	0.1
21.85	22.30	0.45	1.0
22.80	23.53	0.73	1.6
18.80	18.30	0.50	1.3
17.50	17.71	0.21	0.6
24.15	24.25	0.10	0.2
26.35	26.42	0.07	0.1
31.96	32.21	0.25	0.4
29.05	29.21	0.16	0.3
25.42	25.92	0.50	1.0
25.90	25.65	0.25	0.5
22.20	22.70	0.50	1.1
37.04	35.90	1.14	1.6
36.94	37.35	0.41	0.6
		Mean: 0.41 S.D.: 0.3	Mean: 0.9

Appendix 2: As(V) concentrations determined by HG-AAS vs. the sum of pentavalent As fraction (As(V), DMAA, and MMAA) by HPLC-ICP-MS. For the samples 1 to 13, at least one of the determinations was below detection limit. Two samples (WNCTA14 and YNPRH31) showed no response for the As(V) determination by HG-AAS. D.L. = detection limit. R.O.A. = range of analysis.

Sample ID	Field pH	As(V) HG-AAS D.L. 0.3µg/L	Sum of As(V), MMAA, DMAA	R.O.A. [%]
WNCTA14	6.4	< 0.5	314	-999
WNCTA15	7.2	211	897	59.4
WNCTA16	7.1	1043	1386	7.5
WNCTA17	6.4	1188	1339	5.3
WNCTA18	5.9	330	431	7.6
YNPHL01*	3.0	44	115	11.9
YNPNL07*	2.5	89	715	75.8
YNPRH04*	1.8	1715	1700	2.7
YNPRH10*	3.0	468	529	7.3
YNPRH18*	2.2	177	190	29.7
YNPRH29*	2.6	3474	3569	0.8
YNPRH30*	2.6	1173	1702	10.7
YNPRH31*	2.7	< 0.5	500	-999

(*) eight additional measurements were considered for comparison of analytical methods

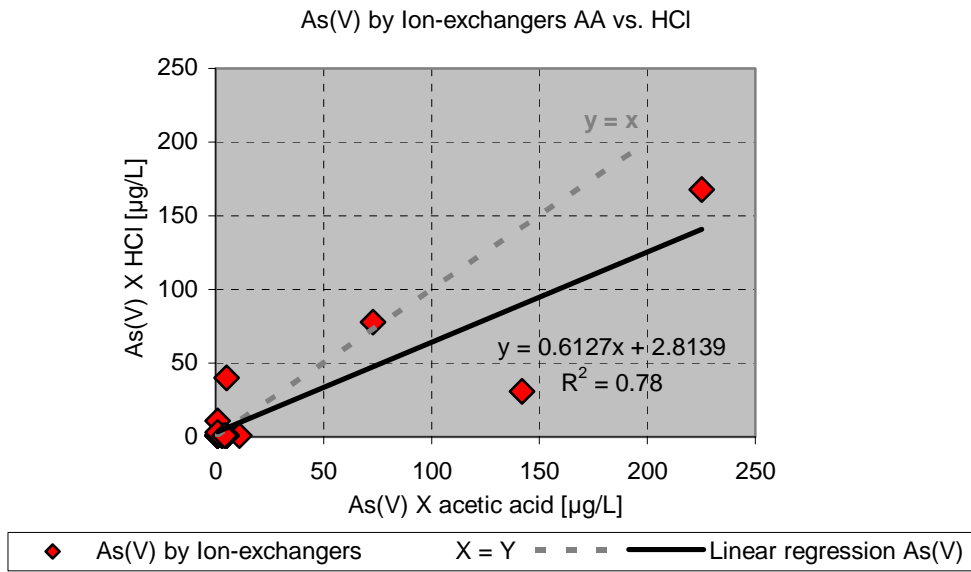
Appendix 3: As(V) concentrations determined by HG-AAS and HPLC-ICP-MS. For the samples 1 to 13, at least one of the two As(V) determinations was below detection limit. Two samples (WNCTA14 and YNPRH31) showed no response for the As(V) determination by HG-AAS; exclusively As(III) was determined. D.L. = detection limit. R.O.A. = range of analysis.

Sample ID	Field pH	As(V) HG-AAS D.L. 0.3µg/L	As(V) HPLC-ICP- MS D.L. 0.3µg/L	R.O.A. [%]
WNCTA14	6.4	< 0.5	301	-999
WNCTA15	7.2	211	830	59.4
WNCTA16	7.1	1043	1211	7.5
WNCTA17	6.4	1188	1320	5.3
WNCTA18	5.9	330	384	7.6
YNPHL01*	3.0	44	56	11.9
YNPNL07*	2.5	89	645	75.8
YNPRH04*	1.8	1715	1626	2.7
YNPRH10*	3.0	468	404	7.3
YNPRH18*	2.2	177	96	29.7
YNPRH29*	2.6	3474	3529	0.8
YNPRH30*	2.6	1173	1455	10.7
YNPRH31*	2.7	< 0.5	115	-999

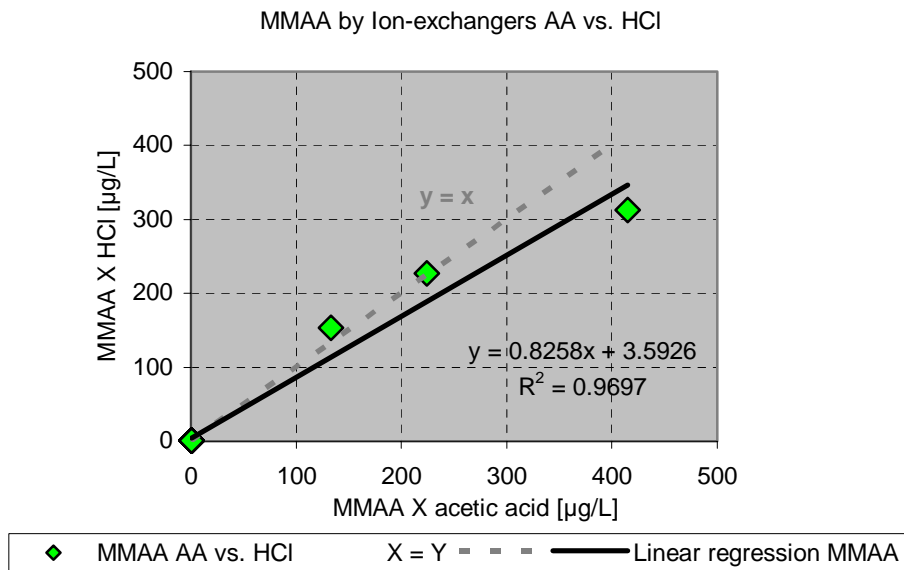
(*) eight additional measurements were considered for comparison of analytical methods

Appendix 4: Comparison of the measured conductivity and the calculated conductivity. The method by Rossum (1975) takes care of the contribution of individual species for the total conductivity in dependence of their equivalence conductance and their respective concentration. Concentrations of 20 selected species were determined with PHREEQC and entered in an Excel-spreadsheet for calculation. The range of analysis (R.O.A.) between the two conductivities is given in percent. The PHREEQC-percent error (charge imbalance) was determined by $100 \cdot (\text{Cat} - |\text{An}|) / (\text{Cat} + |\text{An}|)$. The comment is related to the charge balance by PHREEQC, considering $\pm 2\%$ as significant and is determined after Table 7.

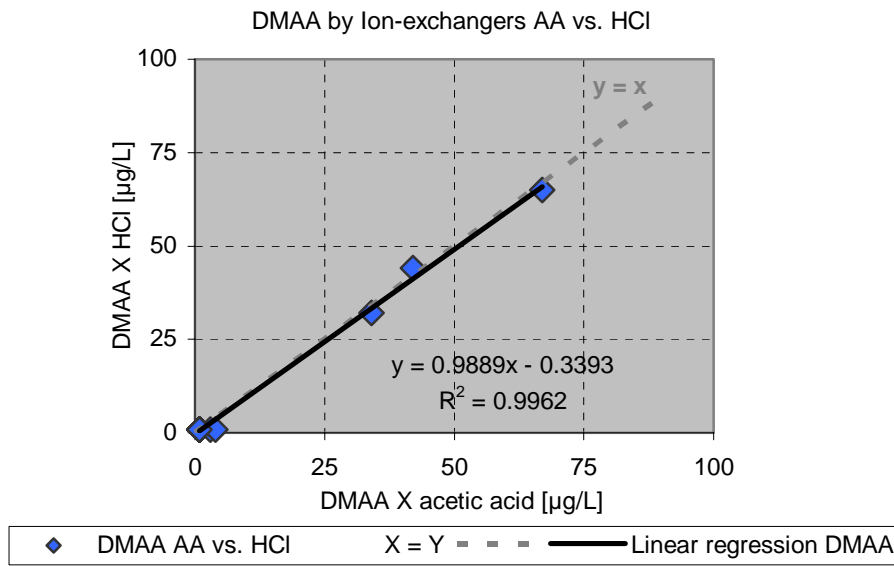
Sample ID	Measured Cond. $\mu\text{S}/\text{cm}$	Calc. Rossum (1975) $\mu\text{S}/\text{cm}$	R.O.A. [%]	PHREEQC %-error	Comment
WNCTA01	369	324	6.5	-0.7	o.k.
WNCTA02	306	211	18.4	-1.7	o.k.
WNCTA03	716	558	12.4	-4.1	deficit of cations
WNCTA04	2250	1777	11.7	1.8	o.k.
WNCTA05	525	543	1.7	-0.5	o.k.
WNCTA06	1335	1578	8.3	-0.6	o.k.
WNCTA07	4320	3835	5.9	0.2	o.k.
WNCTA08	2880	2875	0.1	-0.3	o.k.
WNCTA09	1110	1421	12.3	-0.2	o.k.
WNCTA10	1880	1542	9.9	0.6	o.k.
WNCTA11	525	561	3.3	-0.5	o.k.
WNCTA12	378	267	17.2	-5.5	deficit of cations
WNCTA13	363	268	15.1	1.3	o.k.
WNCTA14	1264	1096	7.1	-5	deficit of cations
WNCTA15	1844	1716	3.6	-5.5	deficit of cations
WNCTA16	1780	1554	6.8	-4.3	deficit of cations
WNCTA17	1875	1720	4.3	-1.5	o.k.
WNCTA18	901	784	6.9	-12.5	deficit of cations



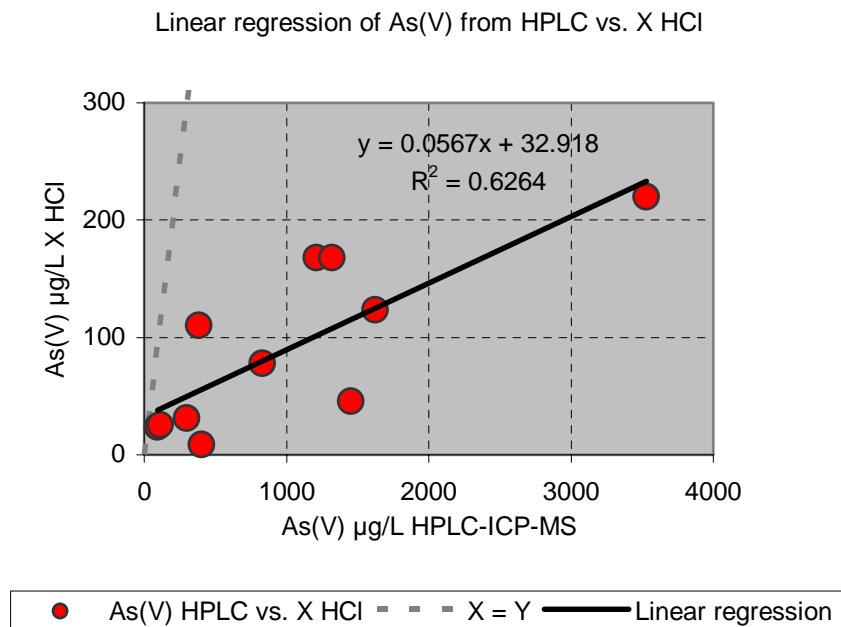
Appendix 5: Linear regression analysis of HCl conditioned ion exchangers (Y-axis) and a.a. conditioned ion exchangers (X-axis) for As(V). Mainly one value is responsible for the gradient < 1 of the regression line. Therefore the response for the a.a. conditioned exchangers can not be said to be improved.



Appendix 6: Linear regression analysis of HCl conditioned ion exchangers (Y-axis) and a.a. conditioned ion exchangers (X-axis) for MMAA. The gradient of the regression line is slightly < 1, the apparent improved response for the a.a. conditioned exchangers is mainly due to one measurement.

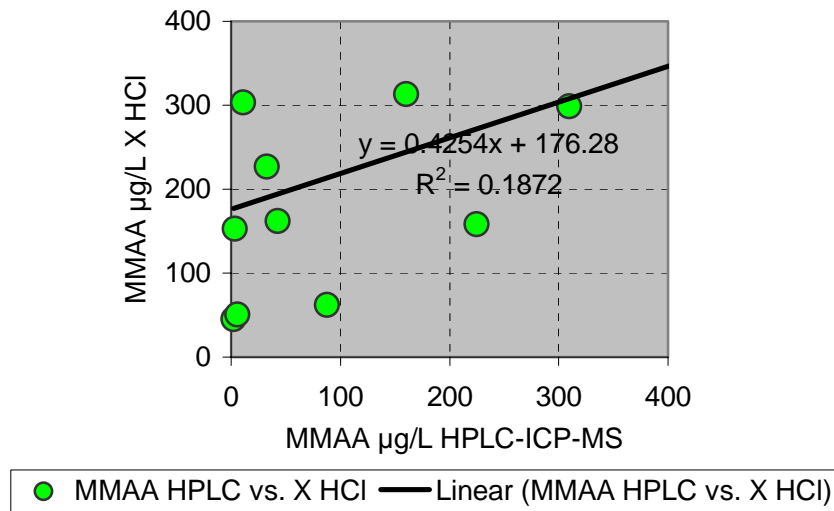


Appendix 7: Linear regression analysis of HCl conditioned ion exchangers (Y-axis) and a.a. conditioned ion exchangers (X-axis) for DMAA. The gradient of the regression line is ~ 1, the response of both types of exchangers is similar.



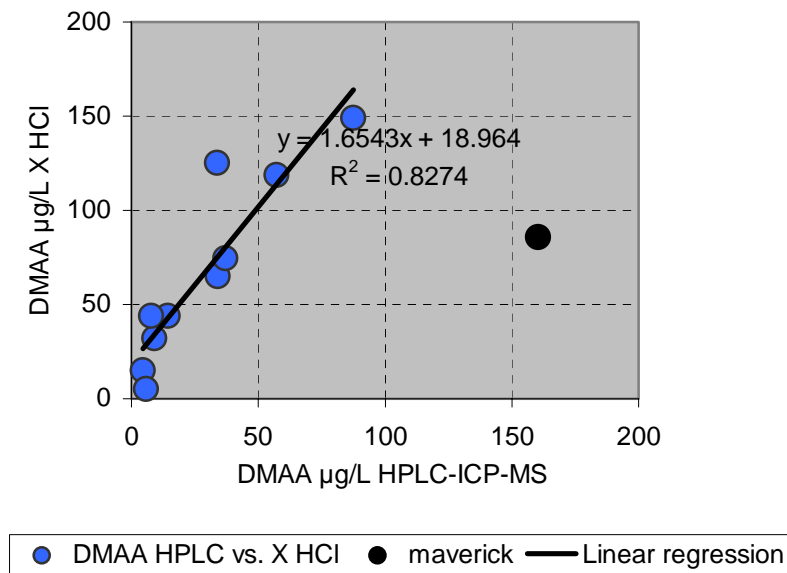
Appendix 8: Linear regression analysis of HCl conditioned ion exchangers (Y-axis) and HPLC-ICP-MS measurements (X-axis) for As(V). The gradient of the regression line is << 1, the response of the HPLC-ICP-MS is significant. Only little As(V) was eluted from the exchangers. Reason might be that some of the As(V) was eluted together with the DMAA in the first elution run with acetic acid.

Linear regression of MMAA from HPLC vs. X HCl

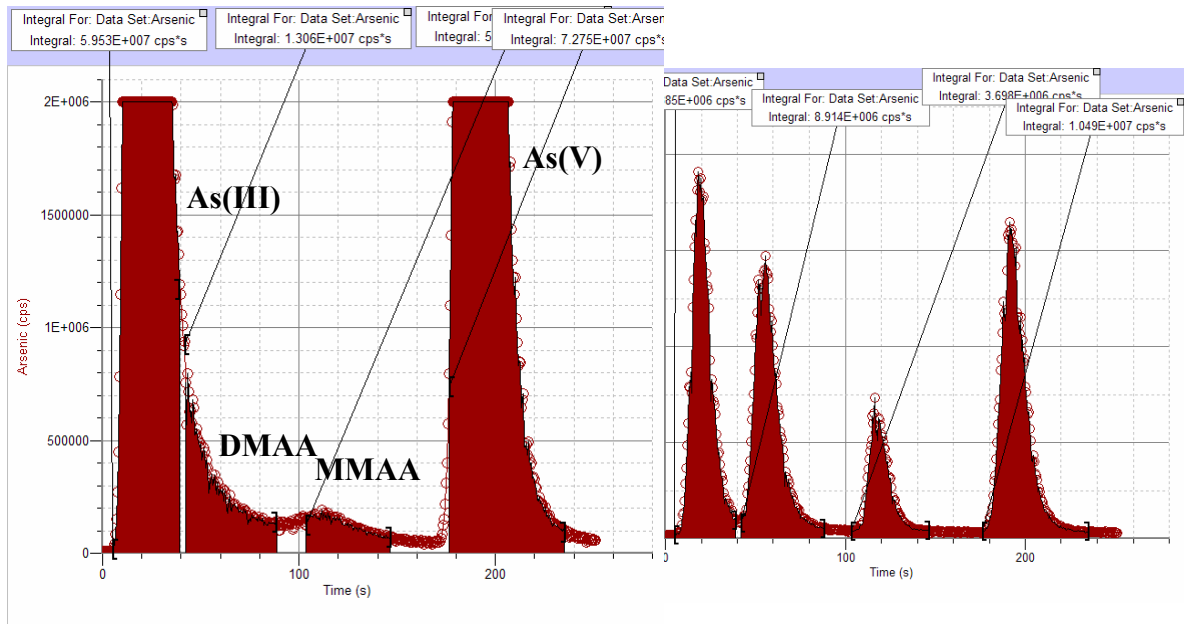


Appendix 9: Linear regression analysis of HCl conditioned ion exchangers (Y-axis) and HPLC-ICP-MS measurements (X-axis) for MMAA. Almost no trend can be identified, the quality of the regression line is poor.

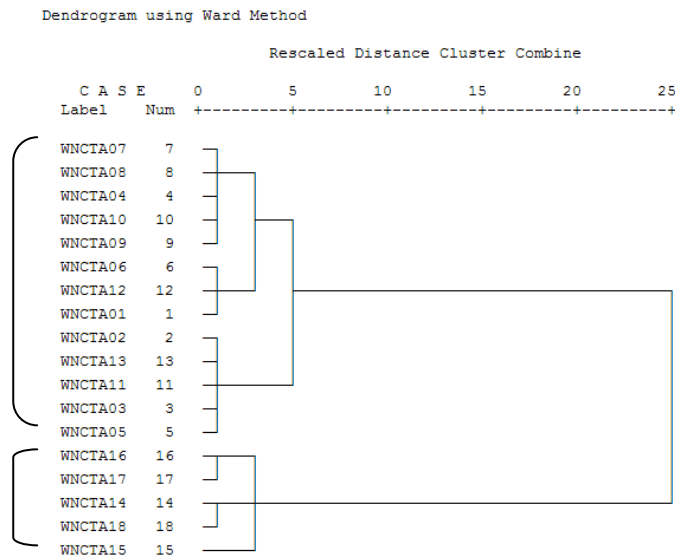
Linear regression of DMAA from HPLC vs. X HCl



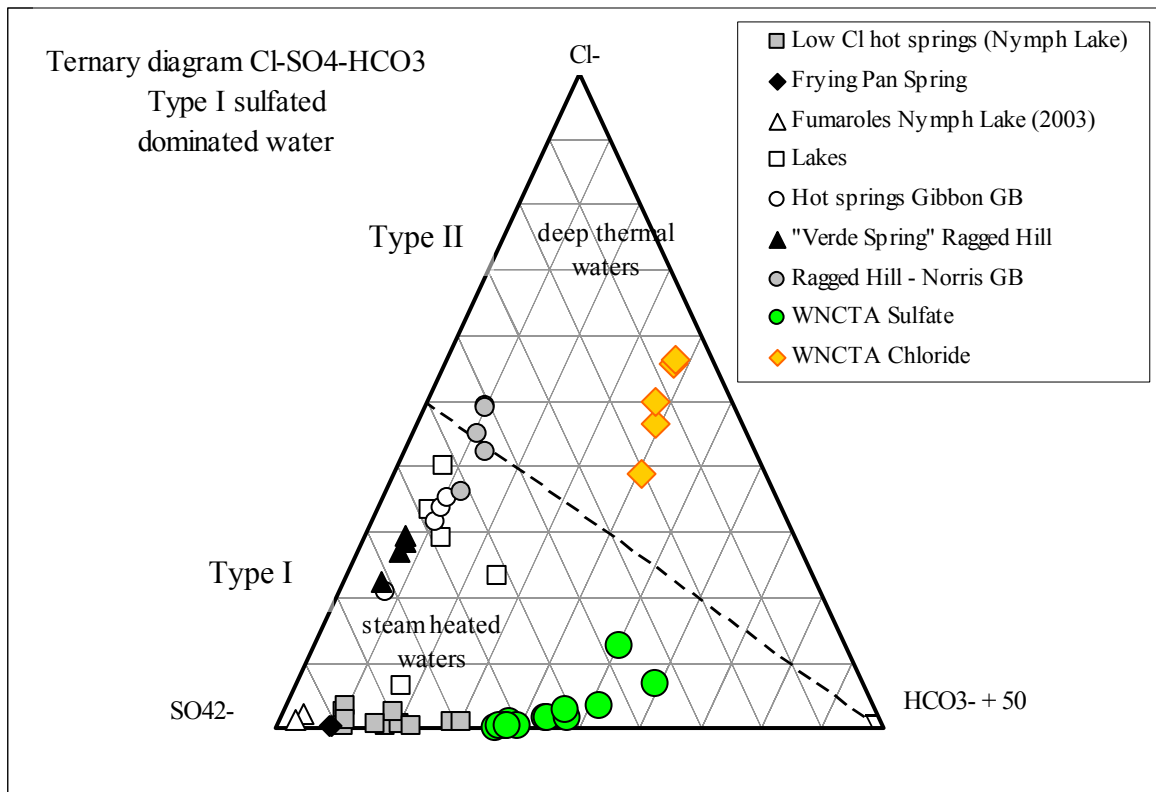
Appendix 10: Linear regression analysis of HCl conditioned ion exchangers (Y-axis) and HPLC-ICP-MS measurements (X-axis) for DMAA. The gradient of the regression line is > 1 , the response of the ion exchangers is stronger compared to HPLC-ICP-MS. Explanation might be the co-elution of As(V) together with DMAA.



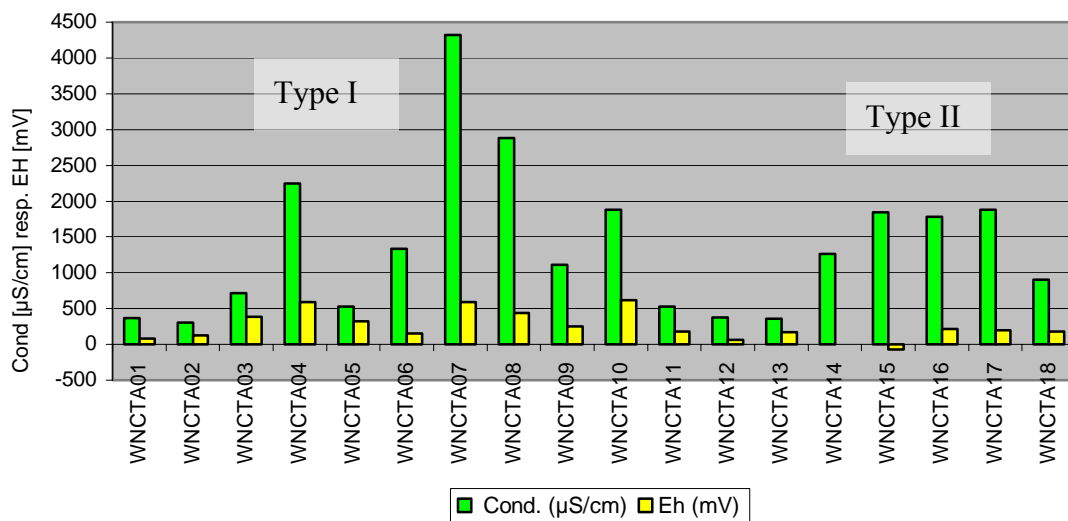
Appendix 11: Determination of the peak area below the curve for the HPLC-ICP-MS measurement. On the left: sample WNCTA15 without dilution, the peaks for As(III) and As(V) are out of range. The As(III) peak hides the DMAA-peak. On the right: peaks of a USGS standard solution showing distinct peaks.



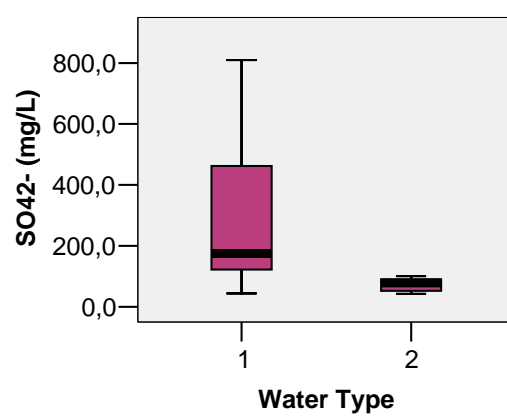
Appendix 12: Dendrogram of the hierarchical cluster analysis using the Ward Method shows two major groups.



Appendix 13: Ternary diagram Cl-SO₄-HCO₃ showing the origin of 7 subgroups of type I steam heated waters (Group 1 to 7) classified by Planer-Friedrich (2004) and the 2 subgroups (WNCTA) from the study area. This diagram places the samples from West Nymph Creek Thermal Area in a larger scale toward other Yellowstone samples. The diagram was modified after the classification scheme of Giggenbach and Goguel (1989), using HCO₃⁻ + 50 instead of HCO₃⁻.



Appendix 14: No significant differences between the two types of water were registered for the conductivity (left box) and the redox potential (right box).



Appendix 15: Significant difference for sulfate between the type I and the type II waters.



Appendix 16: WNCTA01.

Site Code	WNCTA01
Site Name	"Spouter"
Temperature (°C)	61.0
Field pH	5.6
Cond. (µS/cm)	369
Eh (mV)	84
Cl ⁻ (mg/L)	8.7
SO ₄ ²⁻ (mg/L)	44.1
As(T) µg/L (HPLC)	< 2
SiO ₂ (mg/L)	87.9



Appendix 17: WNCTA02. B. Planer-Friedrich sampling.

Site Code	WNCTA02
Site Name	"Brasil"
Temperature (°C)	35.4
Field pH	5.3
Cond. (µS/cm)	306
Eh (mV)	127
Cl ⁻ (mg/L)	6.5
SO ₄ ²⁻ (mg/L)	82.7
As(T) µg/L (HPLC)	< 2
SiO ₂ (mg/L)	70.1



Appendix 18: WNCTA03

Site Code	WNCTA03
Site Name	"Military pool"
Temperature (°C)	17.5
Field pH	6.3
Cond. (µS/cm)	716
Eh (mV)	385
Cl ⁻ (mg/L)	24.4
SO ₄ ²⁻ (mg/L)	71.9
As(T) µg/L (HPLC)	< 2
SiO ₂ (mg/L)	118



Appendix 19: WNCTA04

Site Code	WNCTA04
Site Name	"Anoxia"
Temperature (°C)	12.6
Field pH	2.4
Cond. (µS/cm)	2250
Eh (mV)	591
Cl ⁻ (mg/L)	7.8
SO ₄ ²⁻ (mg/L)	434
As(T) µg/L (HPLC)	< 2
SiO ₂ (mg/L)	119



Appendix 20: WNCTA05

Site Code	WNCTA05
Site Name	"Channel 5"
Temperature (°C)	26.1
Field pH	3.2
Cond. (µS/cm)	525
Eh (mV)	325
Cl ⁻ (mg/L)	5.0
SO ₄ ²⁻ (mg/L)	175
As(T) µg/L (HPLC)	< 2
SiO ₂ (mg/L)	74.7



Appendix 21: WNCTA06

Site Code	WNCTA06
Site Name	"Cinderella"
Temperature (°C)	79.1
Field pH	3.8
Cond. (µS/cm)	1335
Eh (mV)	153
Cl ⁻ (mg/L)	2.3
SO ₄ ²⁻ (mg/L)	470
As(T) µg/L (HPLC)	< 2
SiO ₂ (mg/L)	237



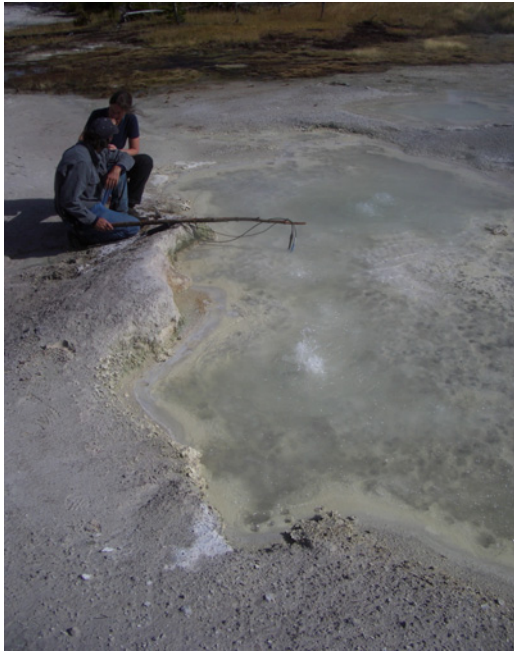
Appendix 22: WNCTA07

Site Code	WNCTA07
Site Name	"Moonrise"
Temperature (°C)	26.9
Field pH	3.5
Cond. (µS/cm)	4320
Eh (mV)	589
Cl ⁻ (mg/L)	2.9
SO ₄ ²⁻ (mg/L)	810
As(T) µg/L (HPLC)	< 2
SiO ₂ (mg/L)	172



Appendix 23: WNCTA08. S. Dill sampling.

Site Code	WNCTA08
Site Name	"Puddle"
Temperature (°C)	50.9
Field pH	2.4
Cond. (µS/cm)	2880
Eh (mV)	438
Cl ⁻ (mg/L)	2.3
SO ₄ ²⁻ (mg/L)	623
As(T) µg/L (HPLC)	< 2
SiO ₂ (mg/L)	79.4



Site Code	WNCTA09
Site Name	"Fizz"
Temperature (°C)	77.1
Field pH	3.9
Cond. (μS/cm)	1110
Eh (mV)	247
Cl ⁻ (mg/L)	1.4
SO ₄ ²⁻ (mg/L)	317
As(T) μg/L (HPLC)	< 2
SiO ₂ (mg/L)	76.2

Appendix 24: WNCTA09. S. Dill, B. Planer-Friedrich sampling.



Site Code	WNCTA10
Site Name	"Chartreuse"
Temperature (°C)	32.6
Field pH	3.5
Cond. (μS/cm)	1880
Eh (mV)	616
Cl ⁻ (mg/L)	3.2
SO ₄ ²⁻ (mg/L)	462
As(T) μg/L (HPLC)	< 2
SiO ₂ (mg/L)	59.8

Appendix 25: WNCTA10



Appendix 26: WNCTA11. B. Planer-Friedrich sampling

Site Code	WNCTA11
Site Name	"Popo"
Temperature (°C)	45.8
Field pH	4.1
Cond. (µS/cm)	525
Eh (mV)	179
Cl ⁻ (mg/L)	4.9
SO ₄ ²⁻ (mg/L)	170
As(T) µg/L (HPLC)	< 2
SiO ₂ (mg/L)	80.3



Appendix 27: WNCTA12

Site Code	WNCTA12
Site Name	"White Eye"
Temperature (°C)	56.3
Field pH	6.6
Cond. (µS/cm)	378
Eh (mV)	65
Cl ⁻ (mg/L)	3.5
SO ₄ ²⁻ (mg/L)	122
As(T) µg/L (HPLC)	< 2
SiO ₂ (mg/L)	141



Appendix 28: WNCTA13

Site Code	WNCTA13
Site Name	"Dillian Spring"
Temperature (°C)	40.8
Field pH	4.9
Cond. (µS/cm)	363
Eh (mV)	168
Cl ⁻ (mg/L)	7.4
SO ₄ ²⁻ (mg/L)	130
As(T) µg/L (HPLC)	< 2
SiO ₂ (mg/L)	74.2



Appendix 29: WNCTA14. S. Dill sampling

Site Code	WNCTA14
Site Name	"Rotondo"
Temperature (°C)	65.4
Field pH	6.4
Cond. (µS/cm)	1264
Eh (mV)	2
Cl ⁻ (mg/L)	254
SO ₄ ²⁻ (mg/L)	78
As(T) µg/L (HPLC)	588
SiO ₂ (mg/L)	190



Appendix 30: WNCTA15

Site Code	WNCTA15
Site Name	"Boiler"
Temperature (°C)	85.5
Field pH	7.2
Cond. (µS/cm)	1844
Eh (mV)	-74
Cl ⁻ (mg/L)	430
SO ₄ ²⁻ (mg/L)	52.3
As(T) µg/L (HPLC)	1869
SiO ₂ (mg/L)	213



Appendix 31: WNCTA16

Site Code	WNCTA16
Site Name	"Fountain of Youth"
Temperature (°C)	55.0
Field pH	7.1
Cond. (µS/cm)	1780
Eh (mV)	216
Cl ⁻ (mg/L)	408
SO ₄ ²⁻ (mg/L)	42.6
As(T) µg/L (HPLC)	1767
SiO ₂ (mg/L)	216



Appendix 32: WNCTA17

Site Code	WNCTA17
Site Name	"Little Prismatic"
Temperature (°C)	60.3
Field pH	6.4
Cond. (µS/cm)	1875
Eh (mV)	199
Cl ⁻ (mg/L)	395
SO ₄ ²⁻ (mg/L)	101
As(T) µg/L (HPLC)	1542
SiO ₂ (mg/L)	219



Appendix 33: WNCTA18

Site Code	WNCTA18
Site Name	"The Swamp"
Temperature (°C)	26.8
Field pH	5.9
Cond. (µS/cm)	901
Eh (mV)	183
Cl ⁻ (mg/L)	171
SO ₄ ²⁻ (mg/L)	90
As(T) µg/L (HPLC)	508
SiO ₂ (mg/L)	101